RAIN RATE ESTIMATION OF NORTHWEST EUROPE AND KENYA FROM SEVIRI SENSOR RETRIEVALS: COMPARISON ŌF PRECIPITATION PROPERTIES VISIBLE AND NEAR INFRARED AND HYDRO-ESTIMATOR ALGORITHMS

MARGARET .W .KIMANI

February, 2011

SUPERVISORS:
Dr, B.H.P., Maathuis
Dr, Ir. C. M. M., Mannaerts

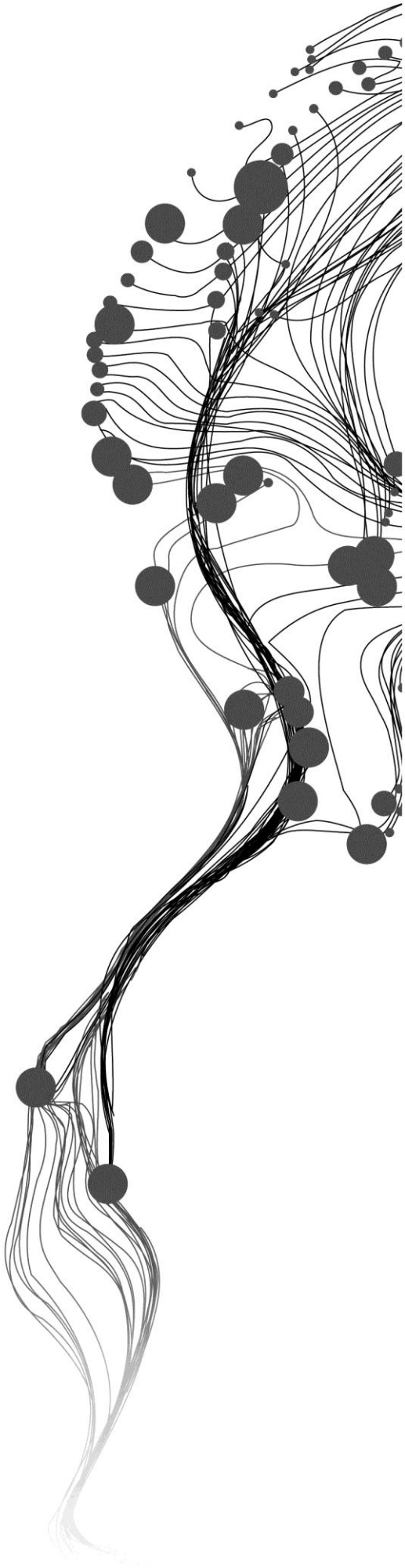

RAIN RATE ESTIMATION OF NORTHWEST EUROPE AND KENYA FROM SEVIRI SENSOR RETRIEVALS: COMPARISON OF PRECIPITATION PROPERTIES-VISIBLE /NEAR INFRARED AND HYDRO-ESTIMATOR ALGORITHMS

MARGARET.W.KIMANI

Enschede, The Netherlands, February, 2011

Thesis submitted to the Faculty of Geo-Information Science and Earth Observation of the University of Twente in partial fulfilment of the requirements for the degree of Master of Science in Geo-information Science and Earth Observation.
Specialization: Water Resource and Environmental Management

SUPERVISORS:
Dr, B.H.P., Maathuis
Dr, Ir. C. M. M., Mannaerts

THESIS ASSESSMENT BOARD:
Prof. Dr, W., Verhoef (Chair)
Dr, R., Roebeling (External Examiner, Research and Development division Weather Services Dept. Royal Netherlands Meteorological Institute)

ABSTRACT

Continuous rainfall estimates at high temporal and spatial resolution is of great importance in Numerical Weather Prediction (NWP) and hydrological model inputs amongst other applications. Geostationary satellites data are of great importance in these applications due to their high temporal (every 15 min) and spatial (1-4km at nadir) resolution. Precipitation Properties Visible/Near Infrared algorithm (PP-VNIR) was compared with Hydro-Estimator (H-E) by use of Spinning Enhanced Visible and Infrared Imager (SEVIRI) of Meteosat Second Generation (MSG) rainfall retrieval over NW Europe and Kenya regions. They were compared with rain gauge measurements for detection of precipitating clouds and rain rate retrieval. Two days were selected in each region in the month of July for NW Europe and the month of April for Kenya which were almost free of night rainfall. Algorithms daytime total rainfall (from 0730 UTC to 1530 UTC) within 5x5 kernel areas were compared to rain gauge day accumulated measurements. Maps scatter and line plot were used to describe the relationship and a linear regression of best fit line determined the significance of the relationship. Categorical statistics of a 2x2 contingency table were used for detection test while continuous statistics of Bias, Root Mean Square Error (RMSE) and correlation coefficients were used for retrieval test. Results showed very high POD and high FAR attributed to point rain gauge measurements failure to characterize the rainfall variability but high spatial resolution of satellite neared that of rainfall variability. They had significant detection and retrieval over NW Europe but retrieval correlation was low over Kenya due to poor rain gauge distribution, topography and evaporation below the cloud effects. The algorithms had significant relationship in retrieval over NW Europe (0.42) and over Kenya (0.91) hence, H-E can fill the PP-VNIR night time gap. Increasing satellite foot print improved the rain gauge measurements validation of the satellite estimates but over Kenya validation using areas of dense rain gauges only can improve the accuracy. Recalibrating the rain /no rain in terms of Z and brightness temperature reduces the over estimation of the H-E non- convective rain rate and is therefore recommended before application. Analyses of more events are recommended for this study.

KEY WORDS: MSG-SEVIRI, Precipitation Properties-Visible /Near Infrared, Hydro-Estimator, detection and retrieval, rain rate, rain gauge measurements, comparison.

ACKNOWLEDGEMENTS

I would like to thank the Netherlands Fellowship Programme (NFP) for awarding me the scholarship to pursue M.Sc. course. Iam grateful to my employer the Ministry of Environment and Natural Resource through the Kenya Meteorological Department headed by the director Dr Mukabana, for allowing me to come to study. Secondly, i want to appreciate Dr. Roebeling and Erwin Wolters of KNMI for their willingness support and provision of Cloud Physical Properties (CPP) look up tables considering their tight schedule. Special thanks to my first supervisor Dr Ben Maathuis for his guidance throughout the study. He was particularly very patient with me and this gave me more confident to move on and I would love to work with him in future. I want to acknowledge my second supervisor Dr Chris Mannaerts for his support and encouragement. Special appreciation goes to Mr. Bas Retsios of Geo-information-Processing for the software operation assistance.

.

DEDICATION

This work is dedicated to my husband Mr. Paul Mwangi, our son James Wanyoike Mwangi together with our dear parents, sisters and brothers for their prayers and moral support.

TABLE OF CONTENTS

LIST OF FIGURES

LIST OF TABLES

LIST OF ABBREVIATIONS

AE	Automatic Estimator
AMSR-E	Advanced Microwave Scanning Radiometer-Earth Observing System
AVHRR	Advanced Very High Resolution Radiometer
AMSU-B	Advanced Microwave Sounding Unit-B
CCN	Cloud Condensation Nuclei
COT	Cloud Optical Thickness
CSI	Critical Success Index
CST	Convective Stratiform Technique
CPH	Cloud thermal dynamic Phase
CPP	Cloud Physical Properties
CWP	Condensed Cloud water Path
DAK	Doubling Adding KNMI
DAR	Dry Adiabatic Rate
DMSP	Defence Meteorological Satellite Program
EUMETSAT	European Organization for the Exploitation of Meteorological Satellites
FAR	False Alarm Ratio
FOV	Field Of View
FRR	False Rejection Ratio
GARP	Global Atmosphere Research Programme
GOES	Geostationary Operational Environmental Satellite
GPI	GOES Rainfall Index
GSOD	Global Surface Summary of the Day
H-E	Hydro-Estimator
H0	Null hypothesis
H1	Alternative Hypothesis
HRIT	High Rate Image Transmission
ITCZ	Inter Tropical Convergence Zone
IR	Infrared
KNMI	Royal Netherlands Meteorological Institute
LEO	Low Orbital Satellite
LWC	Liquid Water Content
LUT	Look Up Tables
MAM	March, April and May
MPE	Multi-sensor Rainfall Estimate
MW	Microwave
MSG	Meteosat Second Generation
NCDC	National Climatic Data Centre
NCEP	National Centre for Environmental Predictions
NIR	Near Infrared
NOAA	National Oceanic and Atmospheric Administration
NWP	Numerical Weather Predictions
OND	October, November and December
Pr	Probability
PERSIANN	Precipitation Estimation from Remotely Sensed Information using Artificial Neural Networks
PP-VNIR	Precipitation Properties Visible/Near Infrared algorithm
POD	Probability Of Detection

PW	Precipitable Water
POR	Probability of Rejection
PR	Precipitation Radar
r_e	Droplet effective radius
RH	Relative Humidity
RGB	Red Green and Blue
RMSE	Root Mean Square Error
SAR	Saturated Adiabatic Rate
SEVIRI	Spinning Enhanced Visible and Infrared Imager
SSM/I	Special Sensor Microwave /Imager
TMI	Microwave Imager
TMPA	TRMM Multi satellite Rainfall Analysis
TRMM	Tropical Rainfall Monitoring Mission
VIS	Visible
WCRP	World Climate Research Programme

1. INTRODUCTION

1.1. Background

This section highlights the rainfall formation processes, cloud types and rainfall physics.

Rainfall Formation

A sequence of four processes must occur to produce rainfall. These are; air cooling to the dew point temperature, condensation of water vapour, droplet growth and importation of water vapour (Dingman, 1994). Air containing water vapour must be cooled to its dew point through radiation, conduction or adiabatic processes. Condensation process requires cloud condensation nuclei (CCN) on which condensation occur to form clouds droplets. CCN could be aerosols, dust, volcanic materials, smoke, forest fires or sea salts. Cloud droplets have a diameter ranging from 0.001 to 0.2 mm. For rainfall to fall from clouds to earth, some of the droplets must grow so that their fall velocity exceeds the rate of uplift such that they survive evaporation as they fall (Ahrens, 2007). Cloud droplets grow to a size of raindrops which is 0.4 to 4 mm diameter or larger. The cloud droplets continue growing by condensation of water vapour. They can also grow when they collide with each other as fall and coalescence. This probability increases fast with droplet size, so that in clouds with re > ~14μm coalescence of cloud droplets into raindrops leads to fast formation of rainfall. . Several million cloud droplets are required to make one raindrop (Gray, 1973). Satellite measurements can detect "r_e" which is the cloud drop effective radius ($r_e = \langle r^3 \rangle / \langle r^2 \rangle$, where r is the radius of the cloud droplets in the measurement volume. The probability of collision and coalescence of drops with $r_e < 12$ μm is very small, to the extent that raindrops cannot form by this mechanism within the lifetime of clouds (Rosenfield & Gutman, 1994).

Rainfall Processes

Rainfall occurs when moist air raises, cools and condenses to form cloud droplets. Clouds form by condensation of water vapour that rise from the surface or is driven by wind to the atmosphere by evaporation, sublimation and transpiration processes as shown in figure 1. The rate at which air cools or warms depends on the moisture status of the air. If the air is dry, the rate of temperature change is 1˚C/100 meters and is called the dry adiabatic rate (DAR). If the air is saturated, the rate of temperature change is 0.6˚C/100 meters and is called the saturated adiabatic rate (SAR). Unlike the DAR which is constant, SAR varies with moisture content in the air. The difference in the two rates is due to the liberation of latent heat released during condensation that reduces the rate of cooling. Processes that are involved in driving the water vapour to the atmosphere for condensation to occur are: convective, stratiform and orographic (Ahrens, 2007).

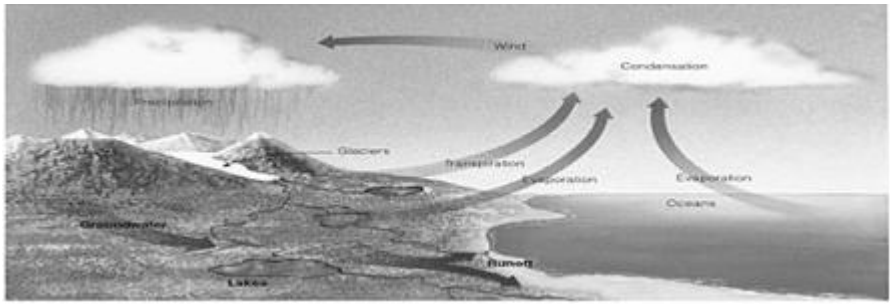

Figure 1: Hydrological cycle: Source: (Ahrens, 2007).

Convective systems

Convection occurs when the Earth's surface within a moist atmosphere, becomes heated more than its surroundings, leading to significant upward motion. This convection occurs from convective clouds, e.g., cumulonimbus (Figure 2). It falls as showers with rapidly changing intensity over a certain area for a relatively short time, due to its limited horizontal extent. This type is common in the tropics due to the intense heating by the sun (Ahrens, 2007) when the Inter Tropical Convergence Zone (ITCZ) is over the region. The rainfall seasons in Kenya in the months of March to May and October to December are dominated by these convective systems.

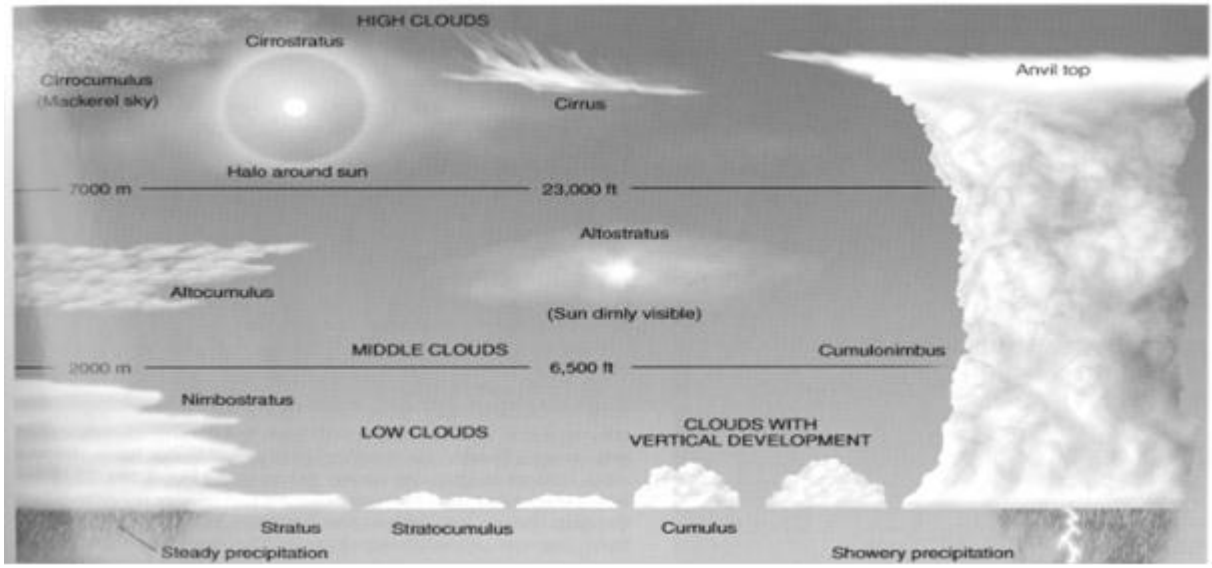

Figure 2: Cloud type's base height. Source: (Ahrens, 2007).

Figure 2 show a generalized illustration of basic cloud types based on height of the cloud base above the surface and vertical development. The three different types of clouds are shown. Low clouds are at the bottom from surface to 2000 m but Cumulonimbus cloud (right) with anvil at the top extends to the high clouds. Middle clouds are at the middle up to 7000 m and high clouds are at the topmost e.g. cirrus clouds.

Stratiform Systems

Stratiform rainfall is caused by frontal systems surrounding the extra tropical cyclones or lows, which form when warm and often tropical air meets cooler polar air. Nimbostratus (Figure 2) is an example of stratiform cloud. When masses of air with different density (moisture and temperature characteristics) meet, the interface between the two is called a front. The warmer air is forced to rise and if conditions are conducive becomes saturated, causing rainfall. In turn, rainfall can enhance the temperature and moisture

contrast along a frontal boundary. Depending on which air mass overrides each other we have different frontal systems e.g. cold front and warm fronts (Brutsaert, 2005). This is the weather systems found in temperate regions e.g. mid latitude areas where NW Europe is located.

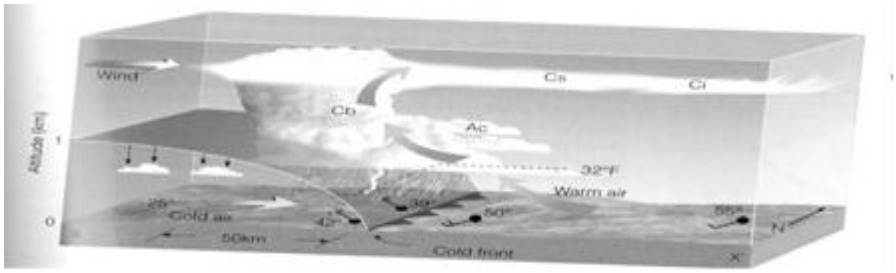

Figure 3: A picture of the extra tropical cyclone. Source: (Ahrens, 2007).

Figure 3 show the tropical cyclone which results from cold polar air mass meeting warm tropical air mass. The warm air mass overrides the cold air mass resulting into development of clouds

Orographic systems

Orographic or relief rainfall (figure 4) occurs when masses of air pushed by wind are forced up the side of elevated land formations, such as large mountains. The raised air cools and condenses to form cloud droplets that grow and fall as rain (Ahrens, 2007). Many hydrologic and ecologic studies recognize the importance of characterizing the temporal and spatial variability of rainfall ,(Goodrich, Faures, Wooolhiser, Lane, & Sorooshian, 1995), (Bindlish & Barros, 2000) especially on mountainous regions due to complex topography and orographic effect leading to more rainfall on the wind ward side, and less on the leeward side and more at higher elevation (Barros & Lettenmaier, 1993),(Barros & Lettenmaier, 1994) than lower elevation. This higher elevation is not captured by the gauges located at lower elevations (Huade & John, 2005).

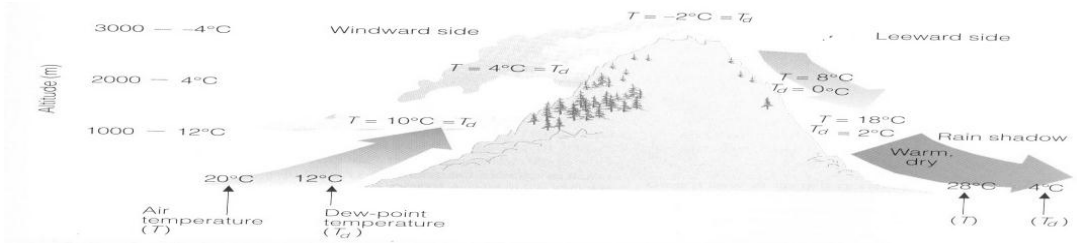

Figure 4: Relief rainfall formation on the wind ward side of a mountain. Source: (Ahrens, 2007).

1.2. Problem Statement

Continuous rainfall estimates at high temporal and spatial resolution is of great importance in climate variability monitoring, Numerical Weather Predictions (NWP), and in hydrological model inputs amongst other applications. Rain gauges network are sparse and available data are insufficient to characterize spatial distribution of the highly variable rainfall (Smith, Seo, Baeck, & Hudlow, 1996). Radar offers spatial coverage at high spatial and temporal resolution but there are difficulties both in obtaining accurate measures of reflectivity and in converting these reflectivity measurements into an accurate representation of the rainfall field at ground level. The former is the result of various phenomena including anomalous propagation, beam block and beam overshoot, and is especially problematic in regions of high

topographic relief where the range of useful radar data can be severely limited (Young et al., 1999). The Spinning Enhanced Visible and Infrared Imager (SEVIRI) of Meteosat Second Generation (MSG) satellite stationed at geostationary location has a good temporal resolution of 15 minutes and spatial resolution of up to 3 km at nadir view. This is quite good for most of these applications. The Precipitation Properties-Visible/Near Infrared (PP-VNIR) algorithm was applied in Northern Europe to detect and estimate rainfall intensities for application in climatological research (Roebeling & Holleman, 2009) by use of SEVIRI data which were retrieved using Cloud Physical Properties (CPP) algorithm (Roebeling, Feijt, & Stammes, 2006). There is a need to verify its validity in a larger area over Europe and over the tropics where convective systems are more dominantly different from extra-tropics where frontal system prevails. One limitation of PP-VNIR is that it can only be used during day time and most of the applications require continuity of rainfall estimates. Hydro-Estimator (H-E) (Scofield & Kuligowski, 2003) which is based on infrared cloud top temperature is being used to estimate rainfall in America every 15minutes and experimentally for the rest of the world by use of geostationary data. The two have similar spatial and temporal resolution and their comparative rainfall estimates is hoped to yield positive results to fill the night rainfall estimates gap by PP-VNIR.

1.3. Main Objective

The main objective of this study is to estimate rain rate over part of NW Europe and over Kenya regions during day time by comparing the two algorithms; PP-VNIR and H-E and validate their results with rain gauge measurements data of the respective regions for a number of events.

1.3.1. Specific objectives

The specific objectives of the study are:

1. To estimate rain rate over NW Europe and over Kenya windows using PP-VNIR algorithm and validate the results by use of rain gauge measurements for each of the regions.
2. To estimate rain rate over NW Europe and over Kenya windows using H-E algorithm and validate the results by use of rain gauge measurements for each of the regions.
3. To compare the PP-VNIR and H-E rain rate estimates and test the significance of that relationship by use of linear regression best line.

1.3.2. Research Questions

1. Can the PP-VNIR algorithm be applied in NW Europe and over Kenya to estimate rainfall intensities? And what would be the accuracy in relation to rain gauge measurements of the corresponding regions?

- Can the precipitating clouds be differentiated from non-precipitating clouds e.g. cirrus in the two regions using PP-VNIR algorithm and with what accuracy compared to the rain gauge measurements of the corresponding region?
- Can the rain rate be quantified from precipitating clouds in the two regions using PP-VNIR algorithm and with what accuracy compared to the rain gauge measurements of each region?

2. Can the H-E algorithm be applied in NW Europe and over Kenya to estimate rainfall intensities? And what would be the accuracy in relation to the rain gauge measurements of the corresponding regions?

- Can the precipitating clouds be differentiated from non-precipitating clouds e.g. cirrus in the two regions using H-E algorithm and with what accuracy compared to the rain gauge measurements of the corresponding region?
- Can the rain rate be quantified from precipitating clouds in the two regions using H-E algorithm? And what would be the accuracy compared to the rain gauge measurements of the corresponding region?

3. Is there any significant relationship between the PP-VNIR and H-E day time rain rate estimates over the two regions?

1.4. Hypothesis

- The null hypothesis (H0: $\rho = 0$) is that there is no significant correlation between the observed and estimated rain rate by PP-VNIR algorithm at 95 %(alpha=0.05) confident level. The alternative hypothesis (H1: $\rho \neq 0$) is that there is significant correlation between the rain rate estimates by PP-VNIR algorithm at 95 %(alpha=0.05) confident level with the observed measurements.
- The null hypothesis (H0: $\rho = 0$) is that there is no significant correlation between the observed and estimated rain rate by H-E algorithm at 95 %(alpha=0.05) confident level. The alternative hypothesis (H1:$\rho \neq 0$) is that there is significant correlation between the rain rate estimates by H-E algorithm at 95 %(alpha=0.05) confident level with the observed measurements.
- The null hypothesis (H0: $\rho = 0$) is that there is no significant relationship between the PP-VNIR and H-E algorithms in rain rate retrieval during day time at 95% confident level (alpha=0.05). The alternative hypothesis H1: There is a significant relationship between PP-VNIR and H-E rain rate at 95 %(alpha=0.05) confident level (alpha=0.05).

1.5. Outline of the Thesis

The thesis consists of 6 chapters.
Chapter 1 is the introduction containing problem statement, objectives, research question, and hypothesis and outline description. Chapter 2 provides a literature review on various methodologies for rain rate estimates. Chapter 3 describes the data set used for the study in terms of acquisition, source and pre-processing. Chapter 4 describes the methodology of PP-VNIR and H-E as applied for the study. Chapter 5 provides the results of analysis and the discussion. Chapter 6 presents conclusions and recommendations drawn from the study and finally the list of references and appendixes are provided.

2. LITERATURE REVIEW

2.1. Methods of Rain rate Estimates

The primary sources of rainfall information are Insitu (e.g. rain gauges measurements) and remote sensing (satellites based). Several studies on these sources have been done as discussed in this section.

2.1.1. Insitu Measurements

This section discusses rain gauge and ground based radar rainfall measurements methods

Rain gauge Measurements

Historically rain gauges have been used for rain rate estimates. The standard way of measuring rainfall or snowfall is the standard rain gauge (Figure 5), which can be found in 100 mm (4 inches) plastic and 200 mm (8 inches) metal varieties. The inner cylinder is filled by 25 mm (1 inch) of rain, with the overflow flowing into the outer cylinder. After the inner cylinder is filled the amount inside it is emptied, then filled with the remaining rainfall in the outer cylinder until all the fluid in the outer cylinder is finished, adding to the overall total until the outer cylinder is empty. During winter the funnel and inner cylinder are removed to allow snow and freezing rain to collect inside the outer cylinder. Once the snowfall/ice is finished accumulating, it is brought inside to melt. The global distribution of gauges is quite variable, from relatively dense networks in the developed countries to sparsely distributed gauges in developing regions (Ahrens, 2007).

Figure 5: An example of the rain gauges used to measure rainfall. Standard rain gauge (left) and tipping bucket rain gauge (right). Source: (Ahrens, 2007).

Over the oceans, gauges are almost non-existent (Prigent, 2010). Rain gauges network are sparse and available data are insufficient to characterize spatial distribution of the highly variable rainfall. This is especially true for mountain areas, where the complexity of the rainfall distribution is combined with the measurement difficulties (Oki, Musiake, & Koike, 1991), (Sturman & Wanner, 2001) (Sotillo, Ramis, Romero, Alonso, & Homar, 2003). Applications in models like in Ecological analysis, Numerical Weather Predictions and hydrological fields require high spatial resolution rainfall distribution as input and this high spatial resolution cannot be achieved through rain gauges estimates.

Weather Radar Estimates

Radar (Radio Detection And Ranging) is used by Meteorological services to gather information about areal representation of rainfall. The radar unit consists of a transmitter and a receiver. The transmitter sends

small microwave pulses. When these pulses come across a target (rain drops or ice crystals) some energy is reflected back to the receiver and is recorded as image or echo. Radar can provide rainfall estimates for time intervals as small as 5 min and spatial resolution as small as 1 km², with an effective range of approximately 200 km. Estimates of the reflectivity factor Z obtained from the radar equation (1-1) are termed equivalent reflectivity and are used to estimate rain rate from reflectivity (Maidment, 1993).

$$R = aZ^b \quad (1\text{-}1)$$

Where, parameters a and b are both functions of the rain type and the heights of the 0ºC isotherm and R is the rain rate in mm and Z is the radar reflectivity.

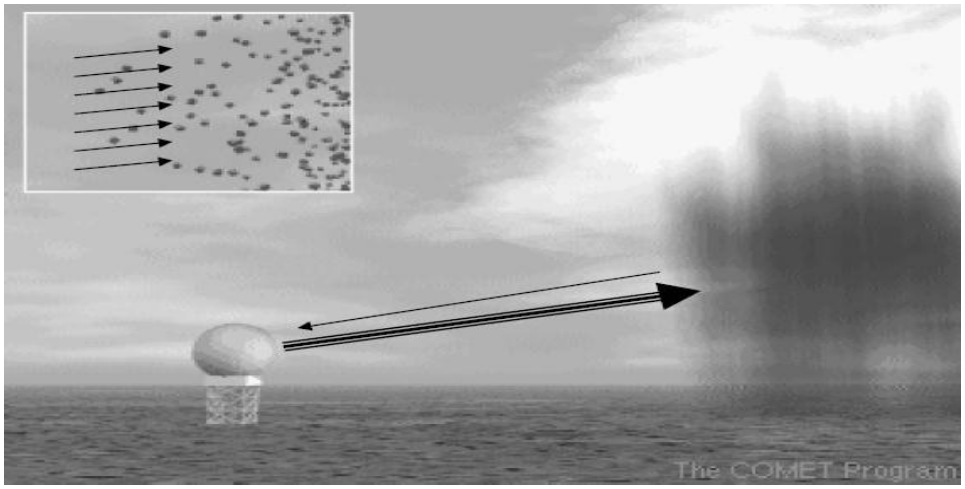

Figure 6: Weather radar. Source: (COMET, 2000)

Radar rainfall estimates compared with rain gauge measurements provide higher spatial and temporal resolutions (AghaKouchak, Habib, & Bardossy, 2010). They have been used together with rain gauges mostly in developed countries like Europe and America yet many places like over oceans still remain without these estimates. Transformation of the radar-measured reflectivity's into rainfall rates presents difficulty in the accuracy of the reflectivity values which can be affected by influence from fixed targets (e.g., ground clutter, beam block) and calibration problem. Radar beam increases in elevation with distance from the radar leading to errors associated with uncertainties in the shape of the reflectivity profile between the beam height and the surface. This results in undetected rainfall or underestimation (Kitchen & Jackson, 1993).

2.1.2. Satellite-based Rainfall Estimation Methods

The uneven distribution of rain gauges and weather radars and the relative lack of rainfall measurements over the oceans have significantly limited the use of global as well local data. Rainfall is one of the most variable quantities in space and time. Rainfall measurements from space are based on the interpretation of the solar radiation that is scattered or emitted from clouds, rainfall and underlying surface, and is monitored by the satellite instruments at the various spectral regions. The interaction of the radiation with the cloud and rainfall particles strongly depends on their composition and size distribution, as described by the Mie theory (Brutsaert, 2005). Therefore, variability in the cloud macro-physical properties and rain intensity would result in substantial changes in the satellite measured radiation that comes from the rain

cloud and hence rainfall. (Levizzani, Amorati, & Meneguzzo, 2002) described several satellite based rainfall estimates methods in their research on Multiple-Sensor Rainfall Measurements, Integration, Calibration and Flood Forecasting (Levizzani, et al., 2002).

Visible and Infrared Methods

Several studies have been done on usage of visible (VIS) (0.4-0.7 μm) and infrared (IR) (10.5- 12.5μm) channel of the solar spectrum. Barrette & Martin (1981) classified rainfall estimation methods into cloud-indexing, spectral life history, and cloud model-based. Each of the categories stresses a particular aspect of the sensing of cloud physics properties using satellite imagery. PP-VNIR algorithm is another algorithm that is based on VIS and IR data retrieval by use of CPP algorithm(Roebeling, et al., 2006) to detect and retrieve the rain rate(Roebeling & Holleman, 2009). It is limited to daytime estimates. The Auto-Estimator (A-E) technique by Vicente et al. (1998) make use of IR 11 μm Geostationary Operational Environmental Satellite (GOES)data and radar data from the US network for applications to flash flood forecasting, numerical modelling, and operational hydrology. The rainfall retrieval is performed through a statistical analysis between surface radar-derived instantaneous rainfall estimates and satellite-derived IR cloud top temperatures collocated in space and time. A power law regression is computed between IR cloud top temperature and radar-derived rainfall estimates at the ground. Rainfall estimates are then adjusted for different moisture regimes using Precipitable water and relative humidity fields from the National Centre for Environmental Predictions (NCEP) Eta Model. However, the A-E frequently assigned high rain rates to cold (but not raining) cirrus clouds and the high dependence on radar for detection of precipitating clouds led to a new algorithm, the H-E(Scofield & Kuligowski, 2003). This is a single-channel (11-μm) rain rate algorithm which is now compared with PP-VNIR algorithm by use of SEVIRI data retrieval in this study. The primary drawback of the VIS/IR techniques is that the observations relate to the characteristics of the cloud profile, rather than the precipitation reaching the surface. Thus, these techniques estimates precipitation at the cloud base, which may still (partly) evaporate between the cloud base and the surface.

Cloud indexing methods

Cloud indexing techniques assign a rain rate level to each cloud type identified in the satellite Imagery. Arkin (1979) provided the simplest and mostly used method named GOES Rainfall Index (GPI) during the Global Atmosphere Research Programme (GARP). The method screens the fraction of the area colder than 235K in the IR with a fixed rain rate. Arkin & Meisner (1987) assigns these areas a constant rain rate of 3 mm/hr. appropriate for tropical rainfall over $2.5^0 \times 2.5^0$. World Climate Research Programme (WCRP) uses the method for 5 days to one month (Huffman et al., 1997) to estimate global rainfall. Todd et al (1999) applied this approach using geostationary satellite data. They associated raining clouds to occurrence of IR brightness' temperatures below a threshold defined for a given location. IR rain /no rain threshold temperatures, was derived from calibration against collateral rain gauge observations. The limiting factor to this approach is cirrus clouds which are cold but non-precipitating, resulting in lower optimum IR thresholds.

Bi-spectral methods

These are the method based on relationship between cold (IR) and bright (VIS) clouds and high probability of rainfall, which are the characteristics of cumulonimbus clouds. Cold, dull (thin Cirrus) or bright but warm are associated with lower probability of rainfall. An Example of this methods is Quasi-operational real-time (nowcasting) rainfall estimating scheme in Canada (RAINSAT) (Bellon, Lovejoy, & Austin, 1980) that screen out cold non-reflective clouds or highly reflective with warm tops. The approach reduces the false alarms of pure IR techniques. This algorithm is based on a supervised classification of trained by radar to recognize rainfall from VIS brightness and IR cloud top temperature from GOES satellites. The GOES data calibrated with radar data to provide real time analysis of rain rate. It was

applied and optimized in the UK by Cheng et al (1993) who found a high correlation with the validation data when VIS and IR was used than when IR was used alone for orographically induced rainfall.

Life- history Methods

The life history technique is based on the premise that the time behavior of clouds on the satellite images and the corresponding radar echoes approximate the simple model, in which both clouds and radar echoes grow to a maximum size and then decay. The life history technique is embodied in the relationship between satellite cloud area and volumetric rainfall reaching the surface (Griffith et al., 1978) as shown in equation 2-1.

$$R_v = \left[I_j < A_e/A_m > jA_{mj} \Delta t \sum_{i=1}^{N} a_i b_i\right] 10^3 \quad (2\text{-}1)$$

where R_v. is the satellite-inferred rain volume for a given cloud on
one image, in m^3, I is rainfall rate in mm/hr, A_e is inferred echo area, in km^2, A_m is the maximum cloud area during the cloud's life cycle, t is the time interval between successive satellite images in hours, i is the index of temperature range j is the denoted term that is a function of life cycle, a is a fraction of cloud covered by a specific temperature range, b is an empirical weighting coefficient for a specific temperature range, N is the number of temperature ranges, and 10^3 is a factor for converting the units from square kilometers to cubic meters.

Cloud model-based

Cloud model techniques introduces cloud physics into the retrieval process for a quantitative improvement based on an overall better understanding of the physical properties of the rain formation processes. Adler and Negri, (1984) developed a one dimensional cloud model which relates cloud top temperature to rain rate and the rain area; the Convective Stratiform Technique (CST). The technique was used to delineate convective as well as stratiform precipitating clouds by use of cloud properties derived from optical satellite data. To achieve this a slope parameter was calculated for each temperature minimum (T_{min}) (Levizzani, et al., 2002). The parameter is defined as:

$$S = \bar{T}_{1-6} - T_{min} \quad (2\text{-}2)$$

Where S is the slope parameter(K)

$\bar{T}_{1-6}$ is the average temperature of the six closest pixels. If the T_{min} is located at (i,j),

$$\bar{T}_{1-6} = \left(T_{i-2,j} + T_{i-1,j} + T_{i+1,j} + T_{i+2,j} + T_{i,j+1} + T_{i,j-1}\right)/6 \quad (2\text{-}3)$$

		j+1,i		
J,i-2	j,i-1	i,j	j,i+1	J,i+2
		j-1,i		

Where i and j refer to the position of the pixel for which Adler and Negri (1988) established an empirical formula to discriminate thin cirrus in the temperaturature/slope plane by use of radar and visible imagery data. They defined a discrimination line such that if the Tmin and its slope fall to the left of the discrimination line, the Tmin location is classified as thin cirrus (non-raining) and a larger slope implies a more clearly defined minimum, that is a thunderstorm.

Passive and Active Microwave Methods

VIS and IR approach relate cloud top temperature to rain rate but at passive microwave (MW) frequencies are the main source of attenuation of the upwelling radiation hence they are physically more direct than those based on VIS/IR radiation. The emission of radiation from atmospheric particles increases the signal received by the satellite sensor, while at the same time the scattering due to hydrometeors reduces the radiation. Type and size of the detected hydrometeors depend upon the frequency of the upwelling radiation. Above 60 GHz ice scattering dominates and the radiometers can only sense ice while rain is not detected. Below about 22 GHz absorption is the primary mechanism affecting the transfer of MW radiation and ice above the rain layer is virtually transparent. Between 19.3 and 85.5 GHz, the common passive MW imagers' frequency range, radiation interacts with the main types on hydrometeors, water particles or droplets (liquid or frozen). Scattering and emission happen at the same time with radiation undergoing multiple transformations within the cloud column in the sensor's Field Of View (FOV). An ocean water body has a low emissivity of about 0.4 which is relatively constant while land surfaces have higher variable emissivity. For many techniques the difference between land and ocean emissivity is such that separate algorithms need to be used one for each surface. For land surfaces, techniques based on emission are not suitable due to high surface emissions effectively masking the rainfall attenuation. Land surfaces have to rely upon the scattering processes and this confine them to medium /high frequencies. Inclusion of the 85.5 GHz on the Special Sensor Microwave /Imager (SSM/I) instruments significantly increased the potential for mapping rainfall over land(Levizzani, et al., 2002). The biggest disadvantage is the poor spatial and temporal resolution, the first due to diffraction (bending of waves around small obstacles and the spreading out of waves past small openings), which limits the ground resolution for a given satellite MW antenna, and the latter to the fact that MW sensors are consequently only mounted on polar orbiters (Kidd, Kniveton, & Barrett, 1998).

An example of active microwave is Precipitation Radar (PR), operating at 13.8 GHz on board the Tropical Rainfall Monitoring Mission (TRMM). It combines the radar, the TRMM Microwave Imager (TMI) and VIS/IR instruments. The radar add information not only on the intensity and spatial/temporal distribution of rain but also on rain type, storm structure, melting layer and latent heat release at different heights. Unlike the passive microwave channels which have difficulties in rainfall measurements over land PR does not have that problem. However the instrument has same shortcomings as ground-based weather radars, of calibration in terms of absolute rain rate values. The rainfall estimates are calculated from the Z profiles by using a power law.

Blending Microwave Visible and Infrared Techniques

Combining several sensors to improve accuracy and coverage has been done by many authors. The Precipitation Estimation from Remotely Sensed Information Using Artificial Neural Networks (PERSIANN) (Sorooshian et al., 2000) provide global rainfall estimates at hourly basis in a 0.25^0x0.25^0 spatial scale It uses geostationary satellite IR data to which is constantly adjusted to estimates of Low Orbital Satellite (LEO) sensors. TRMM Multi satellite Rainfall Analysis (TMPA) combines rainfall estimates from various satellite systems together with rain gauge measurements. It is available both after and in real time, based on calibration by the TRMM Combined Instrument and TRMM Microwave Imager rainfall products, respectively. Only the after-real-time product incorporates gauge data at the present. The dataset covers the latitude band 50°N–S for the period from 1998 to the delayed present. Its coverage depends on input from passive Microwave data collected by a variety of LEO satellites that include the TMI on TRMM, SSM/I on Defence Meteorological Satellite Program (DMSP) satellites, Advanced Microwave Scanning Radiometer-Earth Observing System (AMSR-E) on Aqua, and the Advanced Microwave Sounding Unit-B (AMSU-B) on the National Oceanic and Atmospheric Administration (NOAA) satellite series. They all have physical interaction with the rainfall. Even when

they are put all together significant gaps in the current 3-hourly coverage by the passive microwave estimates is still there (figure 7).

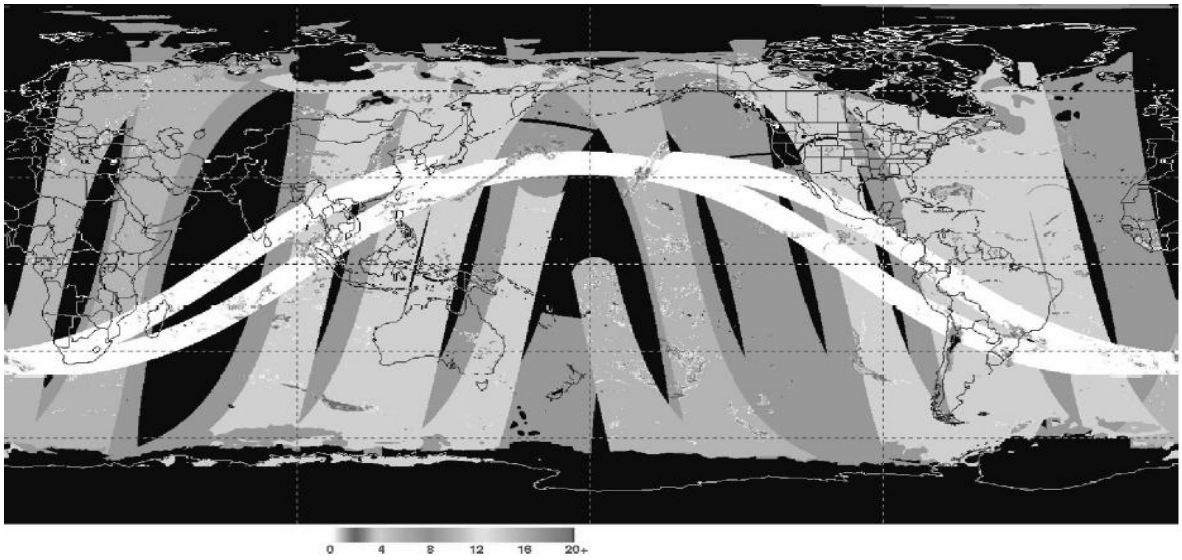

Figure 7: Combined Microwave rainfall estimate for the 3-h period centred at 0000 UTC 25 may 2004 in mm/hr source: (Huffman et al., 2007)..

The Blacked –out areas (Figure 7) denote that lack of reliable estimates, while the zero values in the remaining areas are colour –coded to depict the coverage by the various sensors. The order of precedence for display and corresponding zero colour are TMI (white), SSM/I (light-grey), and AMSR-E (medium grey), and AMSU-B (dark grey).(In the TMPA the TMI, SSM/I, AMSR-E are averaged where overlaps occur) source.

2.2. Cloud Properties from solar and Thermal channels

Multispectral data have long since been available both from polar orbiting and geostationary satellite sensors and used for retrieving cloud properties. The cloud properties have been used for rain clouds identifications and quantification of rainfall intensities (Levizzani, et al., 2002).

2.2.1. Multispectral identification of rain clouds

Cloud radiative properties at VIS, NIR and IR wavelengths have been studied and documented by many authors Kleespies (1995); Liou (1992); Saunders& Kriebel (1988) and Slingo& Schrecker (1982). Their findings were summarized as follows:

•In the thermal IR the radiative properties are sensitive to the size distribution of the hydrometeors

•An increase in the particle size increases the transmissivity, decreases the reflectivity and increases the emissivity of the cloud layer.

•The emissivity of ice clouds is less than that of water clouds. In the NIR the emissivity of a cloud layer is lower than in the thermal IR window: there is a large contribution of reflected radiation at the cloud top.

•Clouds with small hydrometeors scatter and reflect much of the 3.9 μm radiance.

•An increase in cloud particle size or the presence of large drops or ice crystals near the cloud top reduces the 3.9 μm reflectance from the cloud.

•Clouds containing more ice reflect less solar radiation in the 3.7 - 3.9 μm range as ice strongly absorbs at these wavelengths and ice crystals are generally larger than cloud droplets at cloud top.
•NIR reflectance mostly refers to cloud particles effective radius (re).
•VIS reflectance is primarily due to cloud optical depth (Levizzani, et al., 2002)
Rosenfeld and Gutman (1994) used Advanced Very High Resolution Radiometer (AVHRR) channel 1 (0.65μm), 3 (3.7 μm), 4 (10.8 μm), and 5 (12.0 μm) to develop a quantities methodology for the retrieval of cloud top properties that are relevant to rainfall potential of clouds. The principle behind this approach is that larger water droplets and ice particles reflect very little solar radiation in 3.7-3.9 μm region. They found the most crucial parameter to be the effective radius of cloud particles defined as:

$$r_e = \frac{\int_0^\infty r^3 n(r) dr}{\int_0^\infty r^2 n(r) dr} \quad (2\text{-}4)$$

Where, n(r) is the number of the particles of radius r. They showed that optically thick clouds with retrieved re >14μm correspond to well defined areas with radar echoes that indicate the existence of rainfall size particles. Cloud liquid water content (LWC) is also widely used to cloud microphysics
(Slingo & Schrecker, 1982) defined as:

$$LWC = \frac{4\pi\rho_\omega}{3} \int_0^\infty n(r) r^3 \, dr \quad (2\text{-}5)$$

Where, ρ_ω is the density of water. The cloud optical thickness they defined also as:

$$\tau = \int_{z_1}^{z_2} k dz \quad (2\text{-}6)$$

Where z1 and z2 are the height of the cloud base and cloud top, respectively. The Liquid Water Path (LWP) is then given as:

$$LWP = \int_{z_1}^{z_2} LWC(z) dz \quad (2\text{-}7)$$

LWP is proportional to LWC and inversely proportional to r_e in the visible. and r_e are derived from satellite with assumption of vertical homogeneity in the cloud column (Hu & Stamnes, 1993).

3. STUDY AREAS AND DATA SETS

The PP-VNIR and H-E algorithms are both based on geostationary satellites data. The PP-VNIR algorithm based on SEVIRI retrieval has an acceptable accuracy (Bias) of about 0.1 mm h^{-1} and a precision (standard error) of about 0.8 mm h^{-1} in Northern Europe (Roebeling & Holleman, 2009). This is a good accuracy but the algorithm is limited to daylight hence night estimates are not possible. H-E uses IR data for detection and retrieval of rain rate. It has advantage over PP-VNIR algorithm since it eliminates cirrus effects and it can be used day and night (Scofield & Kuligowski, 2003). SEVIRI of MSG data retrieval was used for both algorithms in detection and retrieval of rain rate and the results validated by rain gauge measurements. PP-VNIR and H-E have similar spatial and temporal resolution, hence they were both comparable.

.

3.1. **Study areas**

Northwest Europe window selected is within 47^0 N to 56^0 N (latitude) and 1^0 E to 8^0 E (longitudes). It experiences temperate climate according to Koppen's Climate classification based on annual and monthly averages of temperature and rainfall of latitude range 45° N to 60° N (Europe). Climate in this zone is affected by tropical air-masses (same temperature and moisture characteristics) moving pole ward and polar air mass moving equator ward. Any of the two air masses may dominate the region. These climates have warm, dry summers and cool, wet winters. Seasonal changes between summer and winter are very large. Daily temperatures also change often. Abundant rainfall falls throughout the year. It is increased in the summer season by invading tropical air masses (frontal systems). Cold winters are caused by polar and arctic masses moving south and the region receives most of the rains in summer. The Kenyan window selected is within 5^0 S to 5^0 N latitude and 33^0 E to 42^0 E longitudes. By Koppen's classification this region lies within 10° S to 25 ° N range which is classified as a Tropical Moist Climates. Rainfall is heavy in all months. The total annual rainfall is often more than 250 cm. (100 in.). There are seasonal differences in monthly rainfall but temperatures of 27°C (80°F) mostly stay the same. Humidity is between 77% and 88%. High surface heat and humidity cause cumulus clouds to form early in the afternoons almost every day (FAO, 1997). Convective rainfall systems dominate in this region when the ITCZ passes over the region in March to May and October to December. These are the months of seasonal rainfall over Kenya.

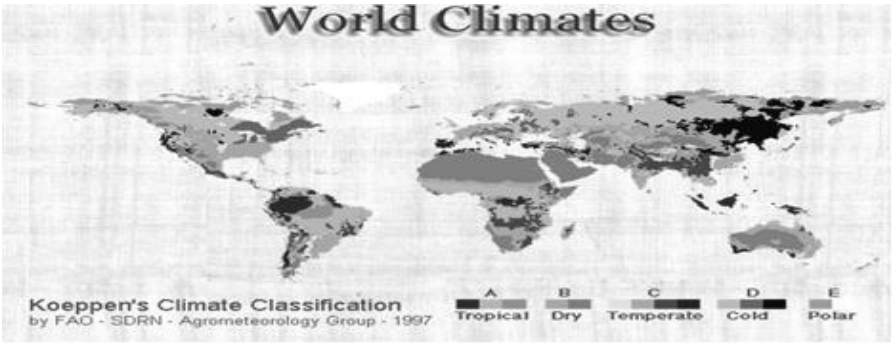

Figure 8: Study areas climatic locations according to Koppen's climate classifications. Source: (FAO, 1997).

3.2. Data Sets

Several data sets in this study are described in this section. The first selection criterion for the months of April and July was a choice of the months when each region receives most rainfall. Mid-latitudes where NW Europe is located receives most of the rains in summer, hence the choice of July while Kenya receives most of the rains when ITCZ lies over the region during the rainfall season of March, April and May (MAM) and October, November and December (OND). The long rainfall is in MAM season hence the choice of April. Second criterion was choice of the days with almost no rainfall at night. This is because the PP-VNIR algorithm is limited to daylight with night estimates being practically impossible. In this study the H-E is hoped to bridge the night time gap of the PP-VNIR algorithm hence their comparison. The algorithms have similar temporal and spatial resolutions since both uses geostationary data sets. To achieve this selection, use was made of European Organization for the Exploitation of Meteorological Satellites' (EUMETSAT) Multi-sensor Precipitation Estimate (MPE)(Heinemann & Kerenyi, 2003). The MPE is an instantaneous rain rate product which is derived from the IR-data of the geostationary EUMETSAT satellites by continuous re-calibration of the algorithm with rain rate data from SSM /I on board DMSP Satellites. The advantages of the high temporal and comparably high spatial resolution of a geostationary IR sensor with the higher accuracy in rain rate retrieval of microwave sensors on polar orbiting satellites are utilized. The assumption made is that cold clouds are more likely to produce rainfall than warmer clouds, in the same synoptic system. Two days from each region were chosen based on those criteria. These were 3rd and 12th July for NW Europe and 2nd and 3rd April for Kenya region in year 2010.

3.2.1. Importing Meteosat-9 image data

Cloud top brightness temperature (10.8 μm) was retrieved from SEVIRI of MSG satellite through the ITC GEONETCast tool box (Figure 9) in High Rate Image Transmission (HRIT) format (Level 1.5). Time series of 10.8 μm brightness temperatures after every 15 minutes from 0730 UTC to 1530 UTC in each region for the respective days were retrieved.

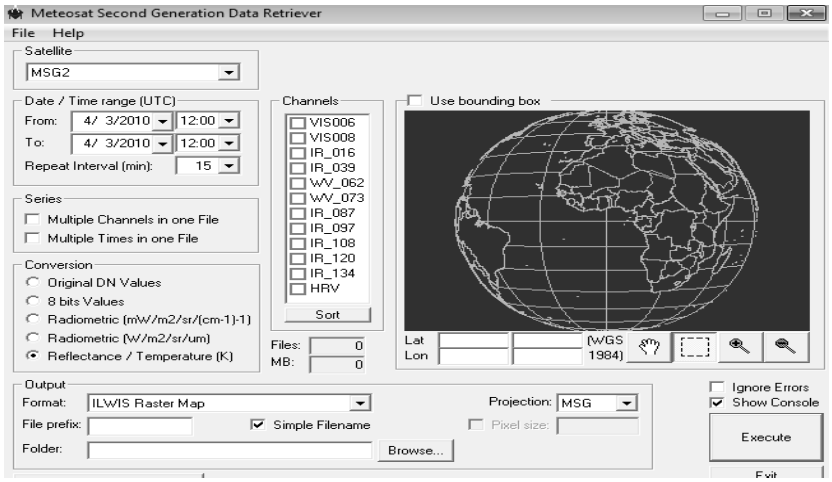

Figure 9: MSG data retriever window, showing the SEVIRI of MSG channels. Source: Courtesy of ITC.

3.2.2. Ground Measurements observation data

The in-situ rain gauge data used in the validation are the accumulated 24-hour rainfall amount in mm. Since the days chosen were free of night rainfalls, the 24hr accumulation represented day time rainfall. The data is available 1-2 days after the date-time of the observations used in the daily summaries from the National Climatic Data Centre (NCDC) in Asheville, NC. These are Global Surface Summary of the Day (GSOD) data and are also available online. By use of GEONETCast tool box rainfall measurements for the selected year were imported. From the yearly record, day records of corresponding months were selected (figure 10) for each station. In NW Europe 29 stations were considered and 31 stations over Kenya. These were all the stations that gave reports on rainfall for the eventful days.. More information on rain gauge stations measurements can be found in appendixes 16 to 19 and maps of the two regions showing the overall rain gauge distribution in appendix 15.

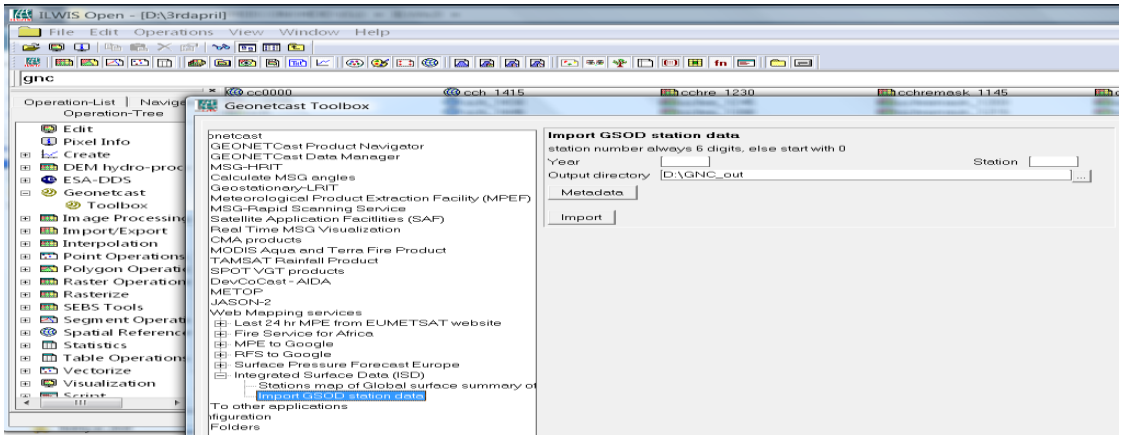

Figure 10: GSOD from website are retrieved easily by use of ITC GEONETCast tool box. Source: Courtesy of ITC

3.2.3. Model data retrieval

The National Centre for Environmental Predictions(NCEP) 6 hour model data forecast applied in Eta model of H-E was retrieved from their website (NCAR, 2010). Details on how to get to the data can be found in the appendix 1. The pgb.ft00.yyyymm data was selected according to the year, month and day. For this study the year 2010, month of July for NW Europe window was selected and the month of April same year for Kenya window both for the respective days. Next selection of the variables and pressure levels as PW (Precipitable water) and RH (relative humidity) was done. The hours selected were 00, 06, 12 and 18 UTC for each variable of the respective days. The pressure level for the Relative humidity (RH) was 500 hpa and non-pressure level for Precipitable Water (PW). The data was in gridded format and was downloaded in a global scale. RH data was in $2.5^0 \times 2.5^0$ spatial resolution and 6 hours temporal resolution. The PW spatial resolution was $1.875^0 \times 1.875^0$ and temporal resolution of 6 hours. Details on data pre-processing can be found in appendix1 and 2.

3.2.4. Cloud Physical properties algorithm fields' data

The CPP algorithm of the Royal Netherlands Meteorological Institute (KNMI) developed by Roebeling et al (2006) retrieve Cloud thermal dynamic Phase (CPH), Cloud Optical Thickness (COT), particle sizes, cloud column height (cch) and Condensed Cloud water Path (CWP) from the SEVIRI on board the MSG by comparing SEVIRI reflectance at 0.6 μm and 1.6 μm to simulated reflectance by Doubling Adding KNMI (DAK) radiative transfer model of water and ice clouds for given optical thicknesses and particle

sizes The PP-VNIR algorithm retrieves rainfall occurrence and intensity from CPP based on Wentz and Spencer (1998) findings, that CWP together with the cloud depth can be used to retrieve rain rate. The principle behind the SEVIRI PP-VNIR retrieval is that, reflectance of clouds at a non-absorbing wavelength in the visible region (0.6μm or 0.8 μm) is strongly related to optical thickness and has little dependence on 1.6 μm or particle size, whereas the reflectance of clouds at an absorbing wavelength in the NIR (1.6 or 3.8 μm) is primarily related to particle size from SEVIRI reflectance at 0.6μm in the visible and 1.6 μm in the NIR of ice and water cloud. The CPP Look Up Tables (LUTs) containing these fields were provided by KNMI on request for the two regions in Hierarchical Data Format, version5. More information on pre-processing can be found in appendix 8. Figure 11 is an example of a LUT extracted by iterative comparison of observed SEVIRI reflectance and the simulated cloud top reflectance by DAK model (Roebeling, et al., 2006) for the viewing geometry: $\theta_0 = 60^0, \theta = 20^0, \varphi = 90^0$ where θ_0 is the solar zenith angle, θ is the satellite zenith angle and φ is the relative azimuth angle. The retrieval of the COT and r_e are done iteratively. First the COT (μm) values corresponding to given reflectance at 0.6μm are extracted. Visually a line is drawn to connect the two values. Secondly re (μm) values corresponding to each COT (earlier extracted) value is also extracted. This is done as many times to get a combination of COT and r_e for different viewing angles and the PP-VNIR algorithm uses these values to derive CWP (gm^{-2}) (Stephens, Paltridge, & Platt 1978) and rain rate.(mm/hr) (Wentz & Spencer, 1998).

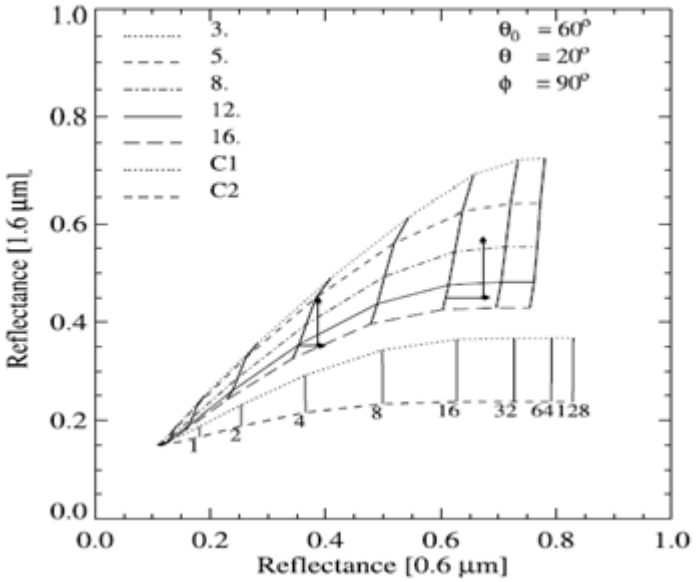

Figure 11: Look up tables of simulated ice and water cloud reflectance by DAK reflectance at 1.6 μm versus 0.6 μm. Source: (Roebeling, et al., 2006).

The 0.6 μm and 1.6 μm (Figure11) are for cloud with optical thickness values between 0 and 128 (solid vertical lines) and with effective radii between 3 and 24 μm (up to 16 μm is shown) for water clouds and C1 and C2 imperfect hexagonal specific columns indicated for ice clouds (dashed and dotted more or less horizontal lines). The results are presented for viewing geometry. The arrows indicate the impact of 11% and 25% difference in 0.6 μm and 1.6 μm reflectance, respectively. The arrows illustrates how a 25% increases in 1.6 μm reflectance results in a decrease of cloud optical thickness values, whereas the horizontal arrows indicate that a 11% increase in 0.6 μm reflectance results in an increase of COT values. Source (Roebeling, et al., 2006).

3.2.5. Retrieval of cloud water path

Assuming a vertically homogeneous cloud, CWP was computed from COT and particle size. It was computed from the retrieved COT at 0.6 μm wavelength (denoted as t_{vis}) and droplet effective radius (r_e) of NIR 1.6 μm (Stephens, et al., 1978). They found r_e (3-1) to be the adequate parameter to represent the radiative properties of a distribution of water particles.

$$r_e = \frac{\int_0^\infty r^3 n(r) dr}{\int_0^\infty r^2 n(r) dr} \quad (3\text{-}1)$$

Where n(r) is the particle size distribution and r is the particle radius. This definition is used to retrieve the effective radius for water clouds between 1 and 24 μm. For ice clouds we assume a homogeneous distribution of C1 and C2 type imperfect hexagonal ice crystals. To derive condensed cloud water path from ice and water phase cloud equation 3-2 is applied.

$$CWP = \frac{2}{3} \tau_{vis} r_e \rho l \quad (3\text{-}2)$$

Where, τ_{vis} is COT (μm), r_e is droplet effective radius (μm) and ρl is the liquid water density. For ice clouds it was assumed a homogeneous distribution of 30 μm (C1) and 40 μm (C2) ice crystals (Roebeling, et al., 2006).

4. METHODOLOGY

4.1. The Precipitation Properties-Visible / NIR algorithm detection and retrieval of rain rate

CPP algorithm as described in Roebeling et al, (2009) was used to retrieve CWP, CPH, COT, cch and particle size from which the PP-VNIR algorithm derived the occurrence and retrieval of rain rate estimates.

4.1.1. Detection of precipitating clouds

Detection of precipitating clouds was done using cloud properties of CWP, CPH, and r_e of the water and ice clouds retrieved by CPP algorithm. Clouds with CWP values larger than a threshold value (160 gm^{-2}) were considered potentially precipitating. CPH was used to separate ice from water clouds. All ice clouds with CWP larger than 160 gm^{-2} were considered to be precipitating and all water clouds with CWP larger than160 gm^{-2} and r_e greater than a threshold value (15 μm) were considered precipitating.

4.1.2. Retrieval of the Height of the Rain Column

The height of the rain column H was determined from the difference between the warmest Cloud Top Temperature (CTT_{max}) over an area of 100 x100 SEVIRI pixels, which is assumed to represent a thin water cloud with a rain column height (dH), and the CTT_{pix} of the observed pixel. Assuming that the vertical decrease in temperature obeys a wet adiabatic lapse rate of 6.5 K km^{-1}, H was estimated by use of equation 4-1.

$$H = \frac{(CTT_{max} - CTT_{pix})}{6.5} + dH \qquad (4\text{-}1)$$

Where CTT_{max} is the maximum cloud top temperature, CTT_{pix} the cloud top temperature of a given pixel, 6.5 is the wet adiabatic lapse rate in Kelvin /km, and dH is the minimum height of the rain column in km. dH = 0.6 km (Roebeling & Holleman, 2009).

4.1.3. Retrieval of the Rain Rates by PP-VNIR Algorithm

The PP-VNIR algorithm is based on columnar liquid water path and the height of the rain column (Wentz & Spencer, 1998) as shown in equation 4-2.

$$R = \frac{\left(\frac{LWP-180}{180}\right)^2}{H} \qquad (4\text{-}2)$$

Where, LWP is the liquid water path in g m^{-2}. R is the rain rate in mm h^{-1} and H is the height of the rain column in km. This equation is only for water cloud and to make the equation more general for both ice

and water CWP is used instead of LWP (Roebeling & Holleman, 2009). The rain rate is retrieved on precipitating clouds ice or water as described in 4.1.2. Unlike the detection of precipitating clouds where ice and water clouds were treated separately, retrieval of rain rate (4-3) is irrespective of the phase since it contains water in solid and liquid form.

$$R = \frac{c}{H}\left[\frac{CWP - CWP_0}{CWP_0}\right]^{\alpha} \quad (4\text{-}3)$$

Where CWP_0 =120 and is the CWP offset value in g m^{-2}, above which R is calculated, α =1.6 and is a dimensionless constant and c=1 and is a constant in mm h^{-1} km (Roebeling & Holleman, 2009).

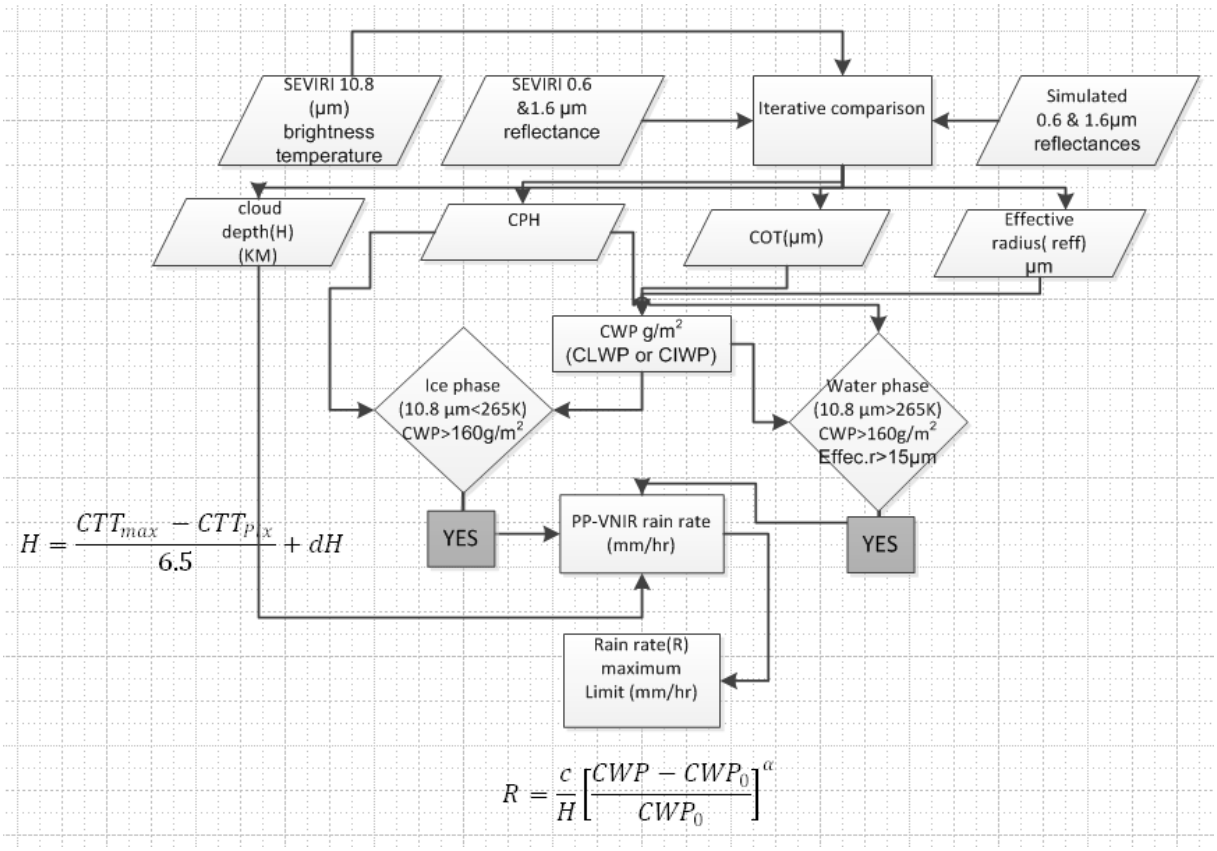

Figure 12: PP-VNIR algorithm methodological flow chart

4.2. Hydro-Estimator Algorithm description

The H-E description according to Scofield and Kuligowski (2003) derive rain rate from convective and non-convective clouds separately by use of GOES brightness temperature (10.7μm). For regions of the world where GOES satellite does not cover other geostationary satellites (METEOSAT over Europe, Africa and western Asia and MTSAT over eastern Asia) data are applied (Vicente, Scofield, & Menzel, 1998). In this study SEVIRI IR 10.8 μm was used. Figure 15 shows H-E algorithm flowchart.

4.2.1. Convective Rain Rate Estimates

The rainfall equation derived from the relationship between rainfall rate from weather radar and GOES Infrared brightness temperature (10.7 μm) for Automatic Estimator (AE) by Vicente et al, (1998) was used in H-E to estimates convective rain rate (4-4). In this study SEVIRI 10.8 μm was used.

$$R = 1.1183 \times 10^{11} exp\left(-0.036382 T_b^{1.2}\right) \quad (4\text{-}4)$$

Where, R is the rain rate in mm/hr. and T_b is 10.8 μm brightness temperatures in Kelvin. The constants 1.1183×10^{11} and 0.036382 correspond to theoretical equivalence of 0.5mm/hr. at 240°K

4.2.2. Convective Rain Rate Adjusted For Precipitable Water

The rain rate of equation 4-13 was corrected at 240°K to correspond to 0.5mm/hr. and a rain rate at 210°K that is related to the Eta model value of PW (Figure 13 a) was also adjusted. The brightness temperature was adjusted according to the available PW (Figure 14 a) before rainfall computation. A maximum rain rate was set (PW (inches) × 40mm/hr.) that was empirically based. Rain rate curve coefficients for the coldest pixel higher than this theoretical maximum was recomputed based on a rain rate of 0.5 mm/hr. at 240°K and the theoretical maximum value at the lowest pixel temperature in the vicinity. This means, pixel value larger than the maximum was assigned the maximum theoretical value. For the stratiform rain rate this maximum value was reduced to 20 % (Figure 13 c). Figure 13b show the relationship of rain rate and brightness temperature at the cloud top (10.8 μm) at different PW depth. Rain rate was then, adjusted in accordance to relative humidity values (Figure 14 c). PW and RH were downloaded from NOAA climatological forecast website (NCAR, 2010) from their Ftp site. The curves (Figure 13 a; 14a and 14c) were converted into polynomial curves which were used as input for rain rate retrieval to have spatial variations (Appendix20) (Scofield & Kuligowski, 2003).

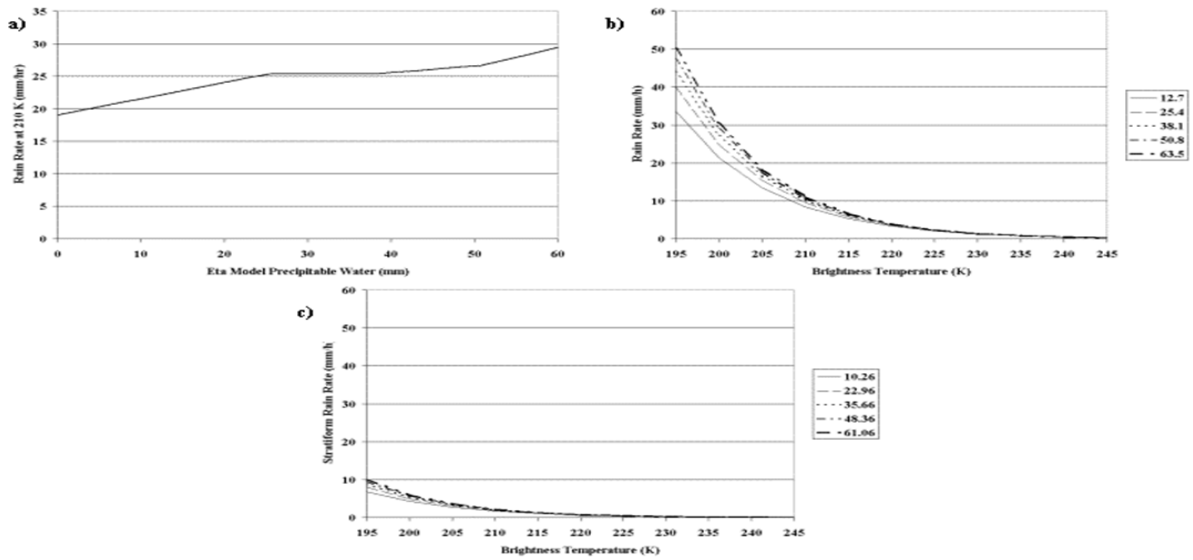

Figure 13: Adjustment functions used in the Hydro-Estimator: (a) rainfall rate at 210K (mm/hr.) as a function of Eta model PW (mm) for convective and non-convective rain rate :Source (Scofield & Kuligowski, 2003)

4.2.3. Convective Rain Rate Adjusted For Relative Humidity

Adjustment for RH (Figure 14 c) was done by subtracting convective rain rate corresponding to available RH. This is assumed to be the amount to be "evaporated" from the rain rate before reaching the surface. These adjustments have helped in handling of stratiform events with embedded convection and in winter time rainfall which is associated with low PW values(Scofield & Kuligowski, 2003).

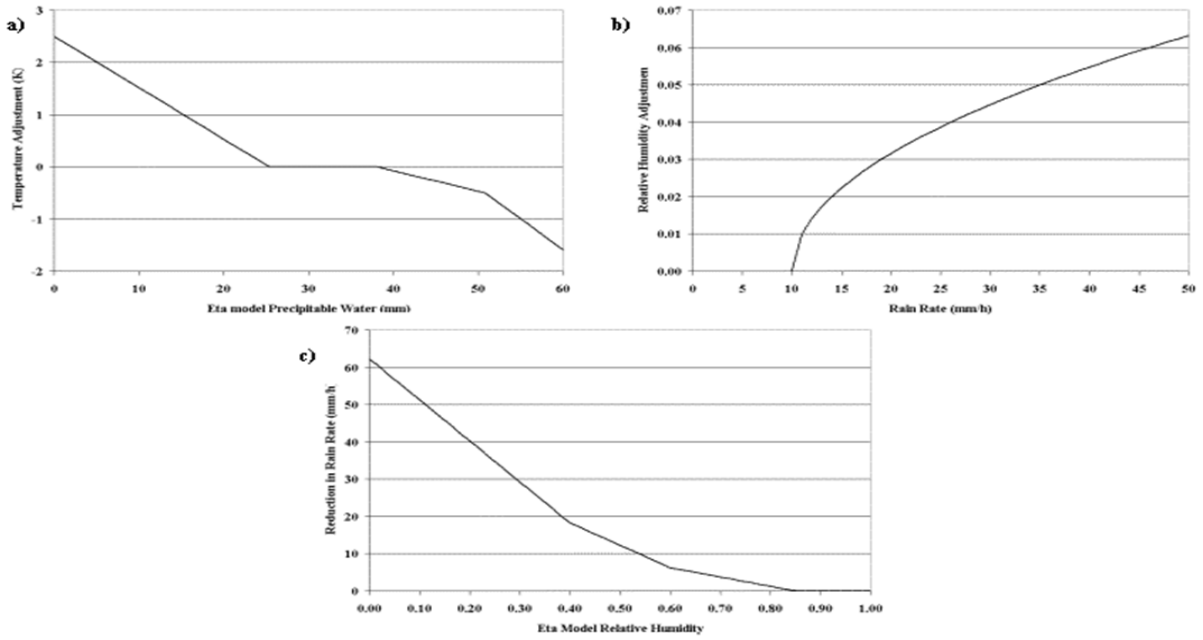

Figure 14: HE adjustment functions: (a) brightness temperature adjustment (K) as a function of Eta model PW (mm); (b) Eta RH as a function of HE rainfall rate (mm/hr.); and (c) Rain reduction in HE rainfall rate (mm/hr.) corresponding to the Eta relative humidity. Source (Scofield & Kuligowski, 2003).

4.2.4. Non Convective Rain rate Estimate

The non-convective rain rate was computed by use of adjusted brightness temperature at 10.8 μm and 20% of the maximum rain rate derived from PW on theoretical basis. This rainfall rate is not allowed to exceed 20% of the corresponding convective rain rate. Just like the convective type, adjustment for relative humidity follows by subtracting the rain rate corresponding to the available RH. Even after limiting the non-convective rain rate to 20% (4-5) of the convective rain rate, over estimation was still there.

$$R_{n=250-T_b} \times \frac{R_{max}}{5} \qquad (4\text{-}5)$$

Where, T_b is the adjusted brightness temperature in Kelvin and R_{max} is theoretical maximum of convective rain rate (mm/hr).

4.2.5. Non convective rain rate adjusted for over estimation

In this study a reduction of this effect was done in two steps taking each eventful day at a time. First the maximum possible rain rate was determined by considering the minimum adjusted brightness temperature and using it to determine the maximum rain rate possible. Each 3x3 kernel area rain rate was divided by this maximum value, such that the kernel corresponding to the maximum rain rate becomes 20% of the corresponding convective rain rate. Secondly, interactively the maximum possible adjusted brightness temperature for each event was determined by making sure there were no outlier maximum rain rates from the main cloud system. In NW Europe on 3rd July which was largely of water cloud 243K was determined and on 12th which was largely of ice cloud 240K was determined. Over Kenya the brightness temperature was almost uniform and 247K was determined. It was evident from this findings that the lower the cloud temperature the lower the maximum adjusted brightness temperature.

4.2.6. Precipitating Clouds determination

This involves finding the minimum temperature (T_{min}) of a 101x101 kernel centred on the pixel of interest. This is the original global pixel size for the H-E (Scofield & Kuligowski, 2003), but in this study a regional scale was determined since the areas of study (e.g. NW Europe) are very small and taking a big kernel would result into few pixels that would not be able to characterize the cloud systems. Since convective systems have many minima, a 3×3 kernel which is the highest spatial resolution was chosen. This was found suitable to characterize local systems which are averaged out by large systems yet cause unpredicted rainfall. This was done by computing the mean (μ) and standard deviation (σ) of the selected radius (3×3 pixel box) of $T_{10.8}$. The presence or absence of rainfall and the relative fraction of convective and non-convective (stratiform) rainfall for the pixel of interest was determined depending on how its temperature compared to its surroundings. A negative Z (equation 4-6) implies the pixel is warmer than the surrounding and rain rate is set to zero, assuming that such pixels are cirrus or otherwise convectively inactive cloud. For positive values of Z (which are constrained to be 1.5 or less), the "core" fraction is related to Z and the "non-core" fraction to (1.5-Z), such that the final rain rate RR can was computed from the "core" rate R_c and the "non- core" rate R_n (Scofield & Kuligowski, 2003).

$$Z = \frac{\mu - T_{10.8}}{\sigma} \tag{4-6}$$

Where, Z is the normalization parameter, μ is the mean value of $T_{10.8}$ of the specified radius and σ is standard deviation of $T_{10.8}$ brightness temperatures in Kelvin

4.2.7. Total Rain Rate by Hydro-Estimator

The total H-E rain rate (4-7), convective and non-convective is summed together.

$$RR = \frac{R_c \times Z^2 + R_n (1.5 - Z)^2}{Z^2 + (1.5 - Z)^2} \tag{4-7}$$

Where, RR is the total rain rate of the H-E in mm/hr. R_c is the convective rain rate in mm/hr. and R_n to non-convective or stratiform rainfall, all in mm/hr. and Z is a standardization quantity (Scofield & Kuligowski, 2003).

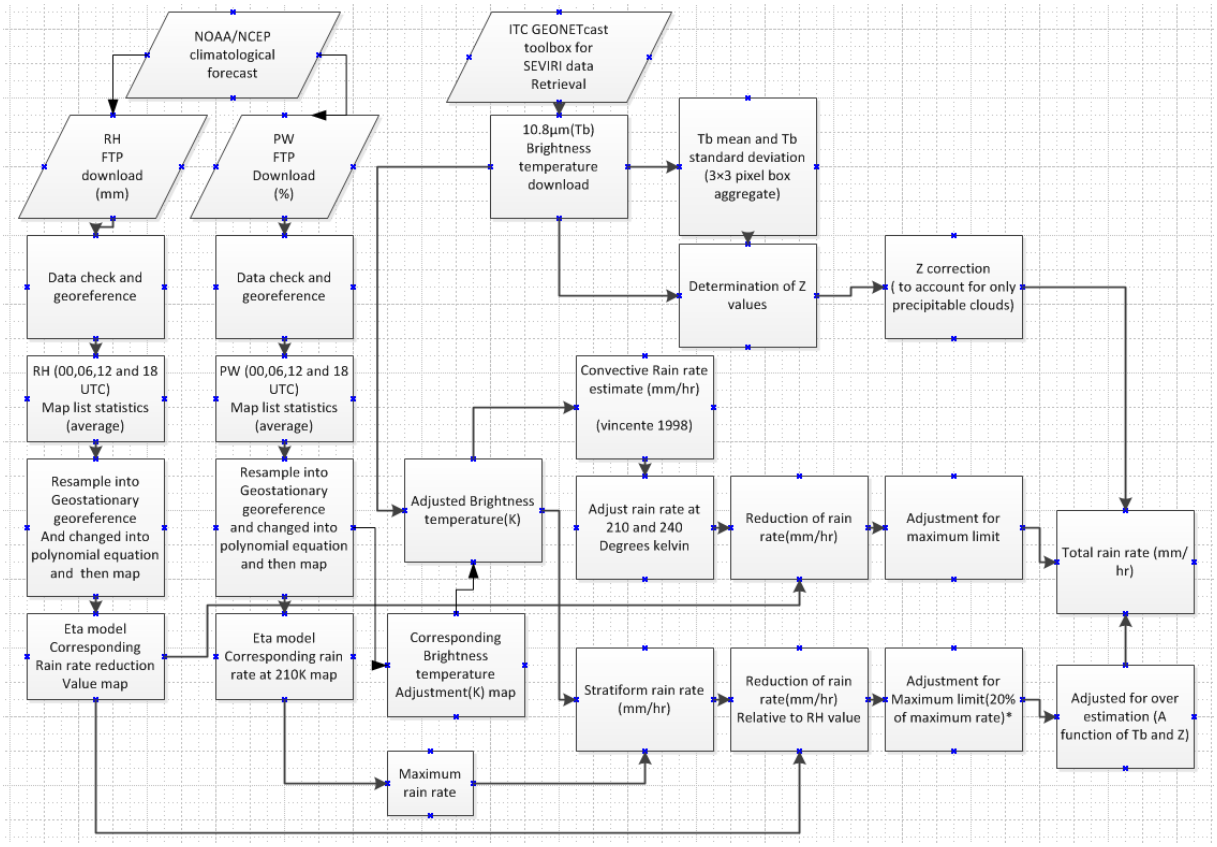

Figure 15: H-E algorithm methodological flow chart

4.3. Skill of detection of PP-VNIR and H-E rain rate in relation to rain gauge measurements

Validation was done by comparing accumulated daily rain gauge data from 29 stations over NW Europe and 31 stations over Kenya to PP-VNIR and H-E day total retrieved rain rate during day time separately. To reduce the uncertainties of different spatial variations of the algorithms and the point measurements of rain gauges, the satellite foot prints was increased to 5x5 kernel area of the day total rainfall estimates of each algorithm. The average value of each kernel was then compared with the corresponding rain gauge measurements. This was done to reduce the uncertainties of different spatial resolution of the satellite and the rain gauges.

4.3.1. Categorical verification statistics of PP-VNIR and H-E rain rate estimates

The skill of the detection of precipitating clouds from SEVIRI retrieval, of PP-VNIR and H-E algorithms relative to the rain gauge observations, were presented in 2 × 2 contingency tables from which various scores (4-8 to 4-13) to verify the quality of the categorical estimates were determined. The statistical indices (conditional distribution) used are: the Probability Of Detection (POD), the False Alarm Ratio (FAR), the Critical Success Index (CSI), the Probability of Rejection (POR), False Rejection Ratio (FRR) and Bias. These were applied to each algorithm separately. Table 1 shows the contingency table. For a rain/no-rain contingency table, R stands for correct no rain estimates, F stands for incorrect rain estimates (i.e., the algorithm gave rain estimates but the observation had no rain), M stands for incorrect no rain estimates (i.e., no rain estimate by the algorithm, but observed had rain estimate), and H stands for correct

rain estimates (i.e., the algorithm gave rain estimates and the observation had rain observed occurrence of rain). Bias indicates the tendency to underestimate (Bias<1) or to overestimate (Bias>1) (Marzban, 1998).

Table 1: Contingency table of the algorithms and the observed probability

Algorithm Estimated rainfall (mm/day)	Observed rainfall (Rain gauge) mm/day)		
	Rain	No rain	Total
Rain	Hits(H)	False alarms(F)	H+F
No rain	Miss(M)	Correct non-events(R)	M+R
Total	H+M	F+R	H+M+F+R

$$CSI = \frac{H}{H+M+F} \quad (4\text{-}8)$$

$$POR = \frac{R}{R+F} \quad (4\text{-}9)$$

$$FRR = \frac{M}{M+R} \quad (4\text{-}10)$$

$$POD = \frac{H}{H+M} \quad (4\text{-}11)$$

$$FAR = \frac{F}{F+H} \quad (4\text{-}12)$$

$$BIAS = \frac{F+H}{M+H} \quad (4\text{-}13)$$

Where H is the correct hits, M is the missed rainfall events; F is the false rainfall alarms and R the correct rejection of rainfall.

4.3.2. Continuous verification statistics of PP-VNIR and H-E rain rate estimates

Continuous verification statistics measure the accuracy of a continuous variable such as rain amount or intensity. PP-VNIR and H-E day total rain rate estimate were compared to rain gauge measurements for each respective day. Statistical analysis was done to determine the accuracy of each algorithm with respect to rain gauge measurements and to each other. The Pearson's coefficient of correlation (4-14) was used and the tests for significance was done using student's t- test (4-15) (Corder & Foreman, 2009). The correlation coefficient r measures the degree of linear association between the values. Root Mean Square Error (RMSE) (4-16). RMSE puts greater influence on large errors than smaller errors despite the direction of deviation. Bias (4-17) measures the average difference between the compared values.

$$r = \frac{\sum_{i=1}^{N}(x_i-\bar{x})(y_i-\bar{y})}{\sqrt{\sum_{i=1}^{N}(x_i-\bar{x})^2(y_i-\bar{y})^2}} \quad (4\text{-}14)$$

$$t = r\sqrt{\frac{n-2}{1-r^2}} \quad (4\text{-}15)$$

Where n is the number of data points and r is correlation coefficient. The relationship is then modelled by the regression best fit line (4-15)

$$RMSE = \sqrt{\frac{1}{N}\sum_{i=N}^{N}(x_i - y_i)^2} \quad (4\text{-}16)$$

$$BIAS = \frac{\frac{1}{N}\sum_{i=1}^{N} x_i}{\frac{1}{N}\sum_{i=1}^{N} y_i} \quad (4\text{-}17)$$

Where x is the observed rainfall measurements (mm/day) and y is the algorithm (PP-VNIR or H-E) rainfall estimates (mm/day) where $\bar{x}$and $\bar{y}$ stands for the corresponding mean values and n is the number of observations/measurements. The same x and y relationship was used to represent PP-VNIR and H-E respectively when comparing their rain rate estimates. Correlation was tested by student's t distribution with n-2 degrees of freedom under the null hypothesis ($H_0: \rho = 0$) that at 95% confidence level, the correlation is not different from zero and alternative hypothesis ($H_1: \rho \neq 0$) that it will be different from zero (Corder & Foreman, 2009). Table showing the tabulated t-test critical values are in appendix 14. The results of measured t-test from this distribution were compared with the tabulated t-test two sided critical values at 95% confidence level. The critical values table columns show the different degree of freedom in % and the rows show the degree of freedom. In this study we had 33 data points (n) from 0730 UTC to 1530 UTC. This is 33 less -2 degrees of freedom which is equal to 31. The tabulated value is 2.0441. The Pr (T<- 2.0441) is = 1-0.975=0.025 for one sided T distribution and so Pr (-2.0441<T<2.0441) =1-2(0.025) =0.95 for 2 sided distribution. If the t-test computed is equal to or greater than the two limits the null hypothesis is rejected and the alternative hypothesis is accepted and vice versa (Corder & Foreman, 2009). The degree of freedom depends on the data point being compared, e.g. in comparison with the rain gauge measurements NW Europe had 29 (n=29-2 degree of freedom) stations while Kenya had 33(n=33-2). The t-test was computed (4-15) and compared with the tabulated values at 95% confident level .Scatter plots and time series lines were also used to check whether there was any association between the algorithms rainfall estimates, after which a linear regression (4-18) best line was fit to check significance of the relationship.

$$Y = a + bX \quad (4\text{-}18)$$

Where X is the independent variable and Y is the dependent variable. The slope of the line is b, and a, is the intercept. In matrix notation this becomes:

$$Y = XB + E \quad (4\text{-}19)$$

Where, Y is an n by 1 vector of y values, X is an n by p matrix of x values, B is an n by 1 vector of regression coefficients, and E is an n by 1 vector of the regression errors.
With this notation the least squares estimator of the regression coefficients is given (4-20) (Silvio & Bryan, 2006).

$$B = (X'X)^{-1}X'Y \quad (4\text{-}20)$$

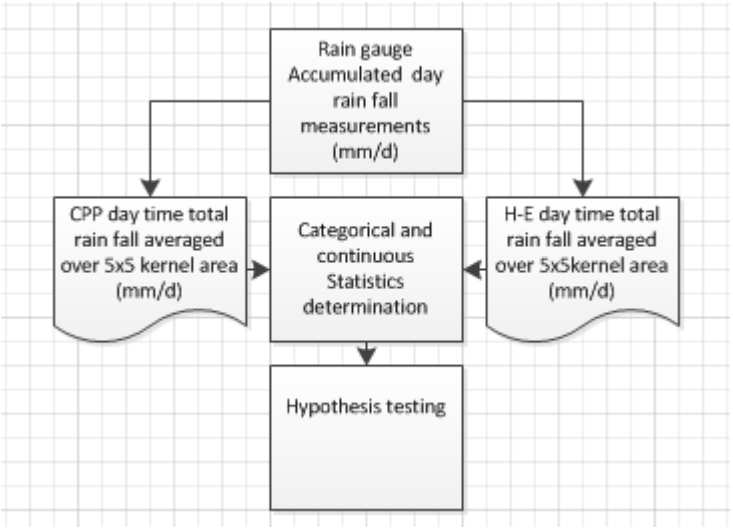

Figure 16: Validation flow chart

5. RESULTS AND DISCUSSION

The results of the two algorithms over NW Europe and over Kenya regions are presented in this section in map form showing each algorithm day time total rain rate and the cloud properties average values for each eventful day. False colour map composites of SEVIRI at 1315 UTC: of R (NIR16), G (VIS008) and B (VIS006) and R (VIS006), G (IR39) and B (IR108) were used to visualize the clouds. 1315 UTC was chosen to represent the convective activity hour. For easier understanding of the false colour composite map, a typical convective system showing stages of development is also shown. Red, Green and Blue (RGB) colour of VIS 006 μm, IR39 μm and IR 10.8μm. The algorithms day total rainfalls were compared with GSOD rain gauge measurements for detection and retrieval of rain rate accuracy. Finally the two algorithms rain rate temporal variations were compared for significant relation. Categorical statistics from contingency tables were used in determining the skill of detection of each algorithm and continuous statistical analysis of correlation; Bias and RMSE were used to determine the accuracy of rainfall estimates. Scatter and line plot were used to describe the relationships of each comparison and a linear regression of best fit line was determined from which the regression statistics results of relationship significance were given.

To test the detection capability the accumulated rain gauge measurements, for each station in each region were compared to the algorithm day total rainfall for each eventful day. Since the days were free of night rainfall the accumulated rain gauge total represented the day time measurements. To account for the uncertainties of spatial variation of satellite and rain gauge point measurements, the algorithms spatial resolution was increased to a 5x5 kernel from which the average values were compared with the rain gauge measurements

5.1. Northwest Europe region results

In this section the results of the two algorithms in detection and estimation of rain rate for North West Europe window are given.. The results of the day total rainfall rate for the H-E (Figure 17 and 19) and PP-VNIR (Figure 18 and 20) algorithms and their intermediate maps are shown. The dates of the events were 20100703 and 20100712 from 0730 UTC to 1530 UTC in 15 minutes time step.

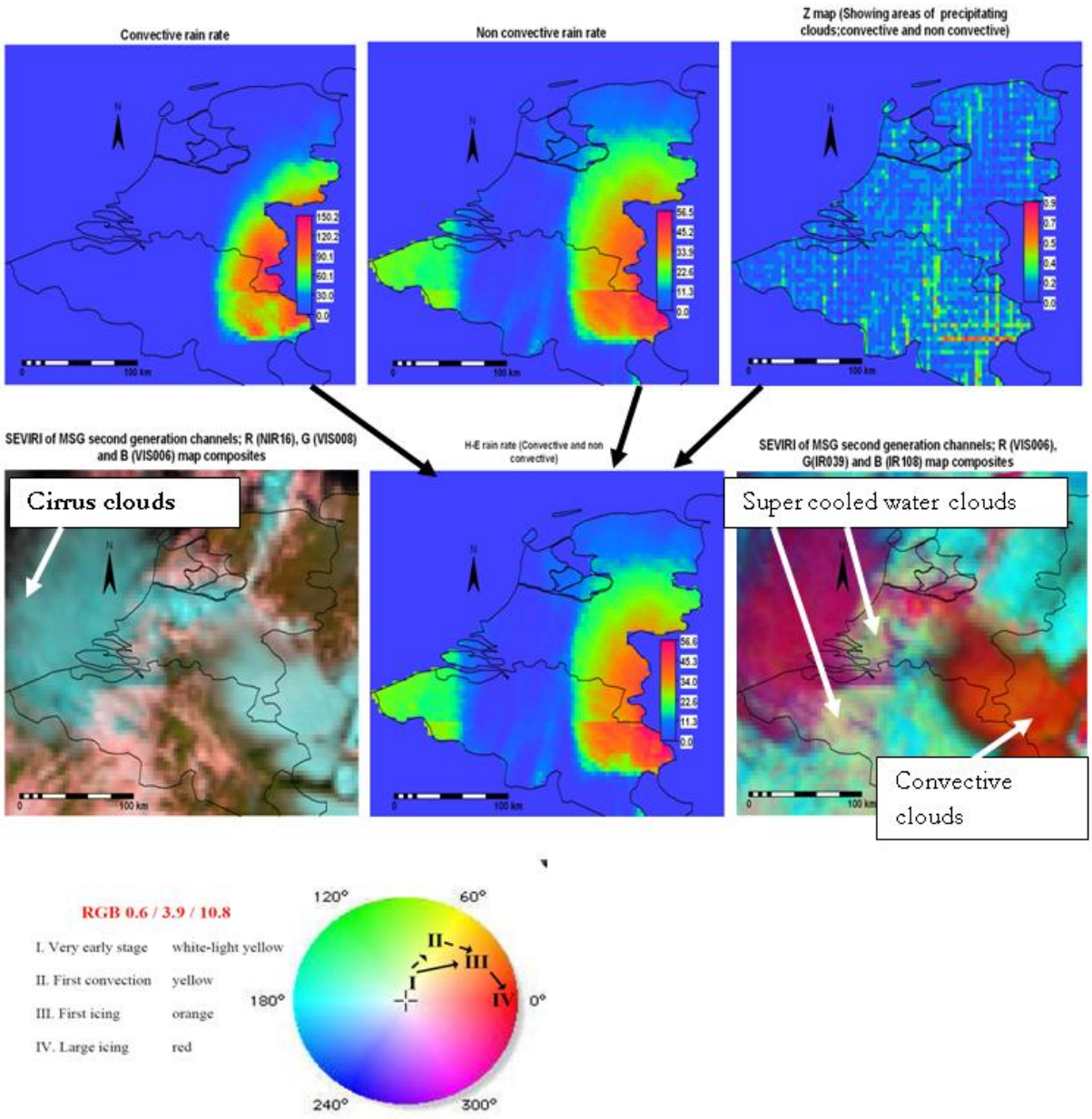

Figure 17: H-E day total rainfall, input maps and 1315 UTC false colour composite maps all in geostationary MSG projection over part of NW Europe on 3rd July 2010

From figure 17, it is apparent that the higher the Z values the higher the convective activity and the lower the values the higher the non-convective activity. The convective activities are to the east and the non-convective includes the central and SW side of the region. The Z map high values (south east) correspond to the convective activities while the central western side of Z map corresponds to non-convective type. From the false colour composites map, the central western region comprises of super cooled water clouds and the H-E underestimates non-convective rain rate over this area. Figure 18 shows the COT and CWP path average values have a direct relationship and CWP is directly related to PP-VNIR rain rate hence COT have a positive influence on the rain rate. Ice phase relates positively with cloud height which means the higher the cloud the colder it becomes hence more of ice phase than water phase. From phase maps it is shown that the day was dominated by water cloud to the north and south and ice cloud to the east and west. It has agreement with false colour composite maps of ice to the west and east. The day total PP-

VNIR rain rate was concentrated to the central region where ice and water cloud coexisted. It is seen that the two algorithms in delineating precipitating clouds had spatial variation.

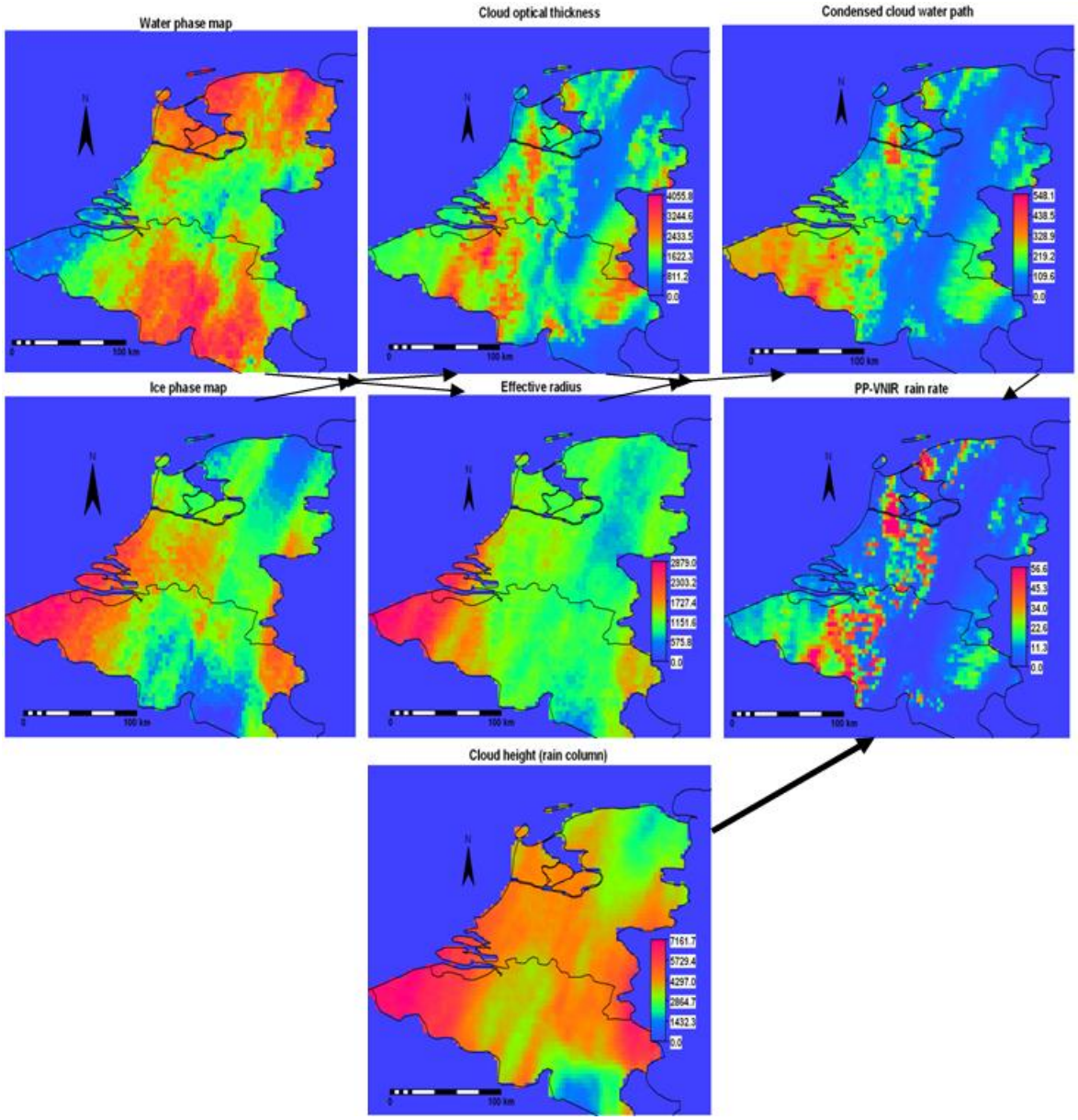

Figure 18: PP-VNIR day time total rain rate and cloud properties day average values over part of NW Europe on 3rd July 2010 all in geostationary MSG projection.

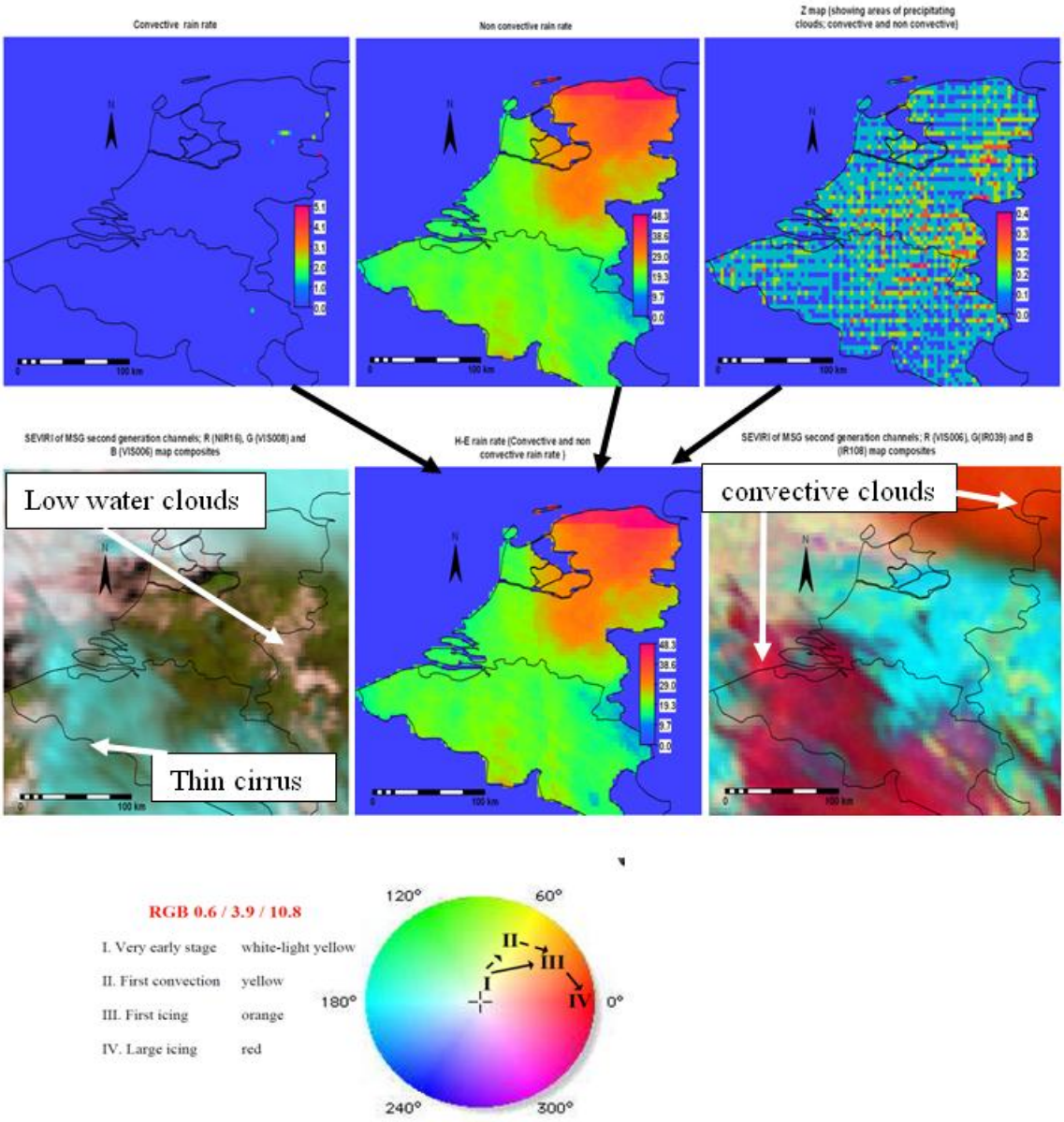

Figure 19: H-E day total rainfall, input maps and 1315 UTC false colour composite maps all in geostationary MSG projection over part of NW Europe on 12th July 2010.

From Figure 19 the false colour composite maps indicate convection activities to the north east and cirrus clouds together with developing convective clouds to the southern part The H-E considered north east to be dominated by non-convective rainfall. Figure 20 of the PP-VNIR and day total rain rate of a day dominated by ice cloud to the south and of water to the north. The rain rate was concentrated to the northeast where water clouds were dominant and scattered to the south where ice clouds were more. The cloud height was mainly highest to the southern part which was associated with ice clouds. The H-E and PP-VNIR had agreement in delineating precipitating clouds to the north which was mixed ice and water cloud.

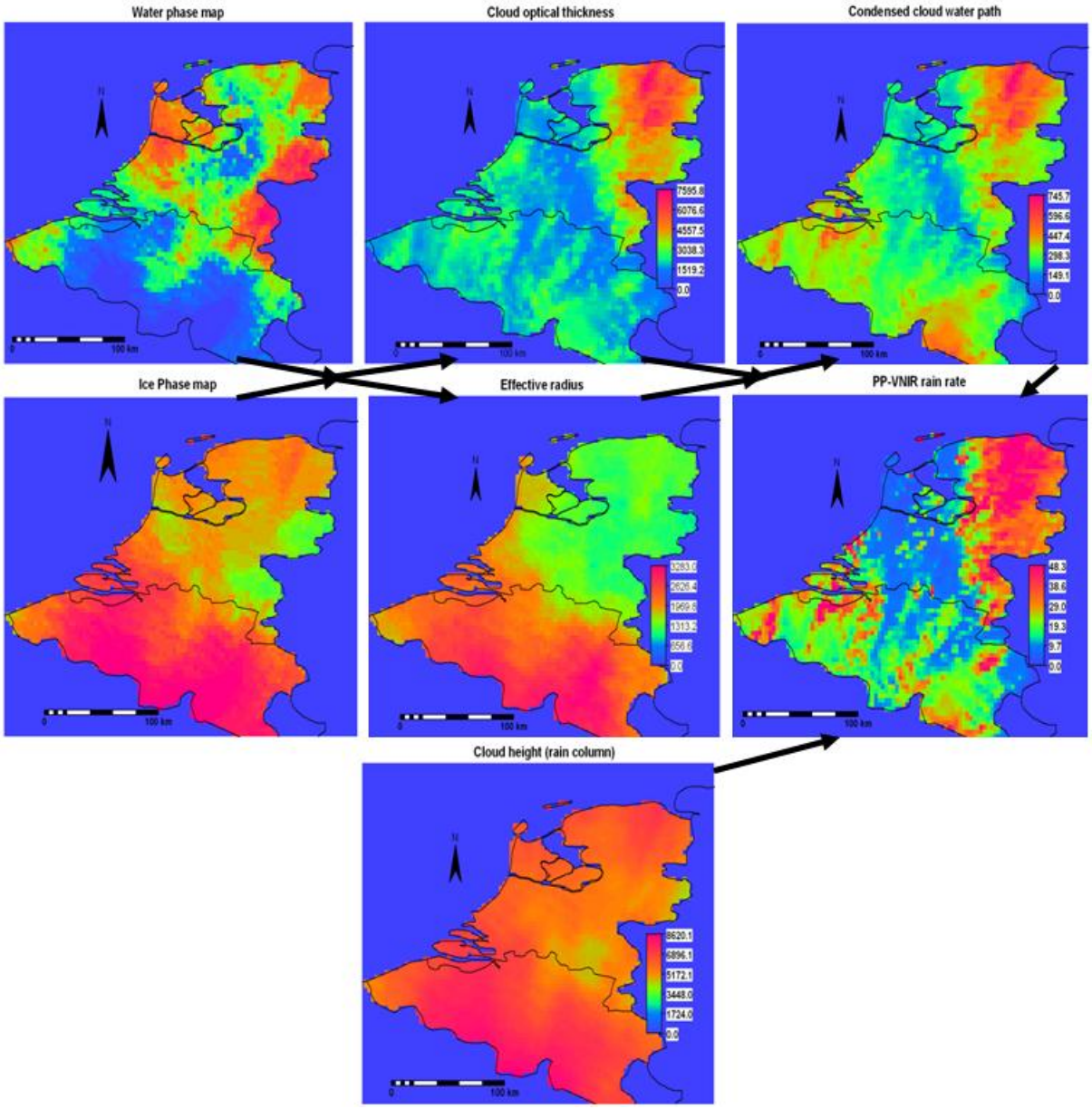

Figure 20: PP-VNIR day time total rain rate and cloud properties day average values over part of NW Europe on 12th July 2010

5.1.1. PP-VNIR and H-E comparison with ground measurements over NW Europe

Detection validation:

The PP-VNIR and H-E day total rainfall estimates were compared with rain gauge measurements station by station. By use of contingency table the corresponding rainy and non-rain days were determined. Day rainfall total for each region by each algorithm was used to compare with the 29 stations (Appendix 16 and 17) accumulated rain gauge measurements (GSOD rain gauge measurements) for each station. Tables' showing the categorical analysis scores of detection of each algorithm in relation to observed values and the overall accuracy in percentage were determined. Bar graphs and line plot were also used to describe the relationship of each algorithm estimates in relation to the observed values (Figures 21 to 24). Table 2 show the two algorithms detection capability was the same for both eventful days over NW Europe. From Figure 21 POD was very high and likewise the FRR was very low. On the 12th day of July the rain rate

reported increased and this was marked with decrease in Bias and increase of CSI as well as the percentage correct ratio. The FAR however increased with increase of rain rate.

Table 2: Contingency table of the daily total rainfall estimates by PP-VNIR and H-E algorithms and accumulated rain gauge measurements over NW Europe.

3rd July							
Estimated Rain rate by PP-VNIR	Observed by rain gauges			Estimated Rain rate by H-E	Observed by rain gauges		
	Rain	No rain	Total		Rain	No rain	Total
Rain	9	20	29	Rain	9	20	29
No rain	0	0	0	No rain	0	0	0
Total	9	20	29	Total	9	20	29
12thJuly							
Estimated Rain rate by PP-VNIR	Observed by rain gauges			Estimated Rain rate by H-E	Observed by rain gauges		
	Rain	No rain	Total		Rain	No rain	Total
Rain	13	16	29	Rain	13	16	29
No rain	0	0	0	No rain	0	0	0
Total	13	16	29	Total	13	16	29

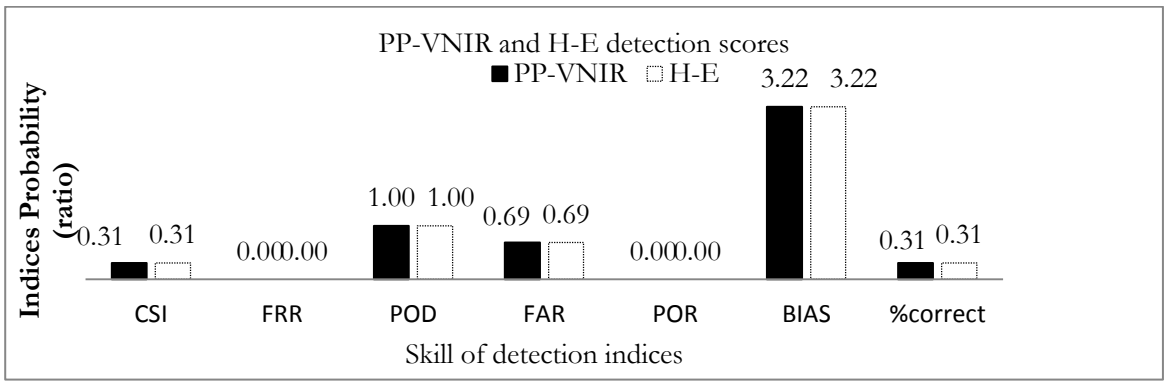

Figure 21: Skill of detection bar graphs for PP-VNIR and H-E algorithms on 3rd July

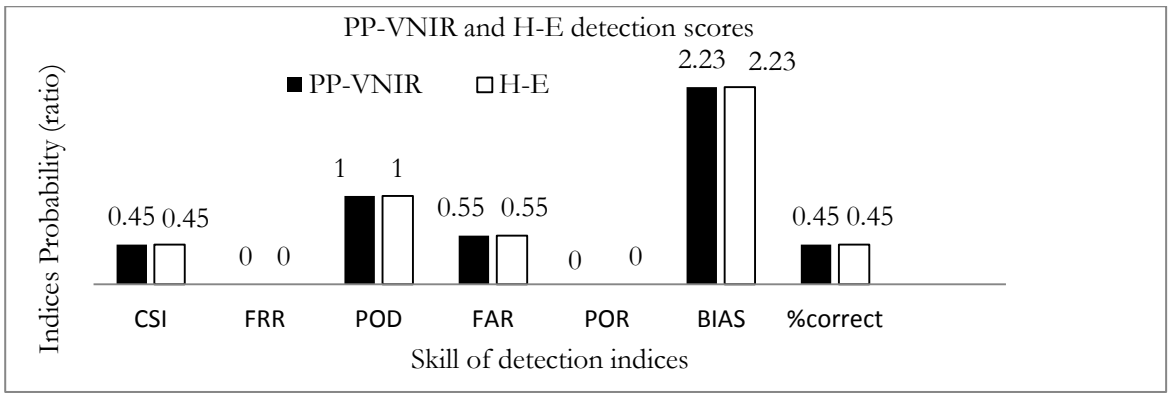

Figure 22: Skill of detection bar graphs for PP-VNIR and H-E algorithms on 12th July

Retrieval validation;

The satellite foot print was increased to 5x5 pixel box from which average values were determined. These average values were compared to the accumulated rain gauge measurements assuming the 5x5 pixel box area represented rain gauge area coverage. The results of the comparison in terms of line curves (Figure 23 and 24) indicate high rain rate by the algorithms as compared to rain gauge measurements. The algorithms however showed same trend with rain gauges particularly on 12th July when the rain rate increased.

Results of the algorithms in quantifying the rain rate was further determined by use of continuous statistics analysis (Table 3). The computed t-test was higher than the tabulated. It is noted that the accuracy of estimate increased with increase in rain rate on 12th July. This is indicated by higher correlation and corresponding higher computed t-test.

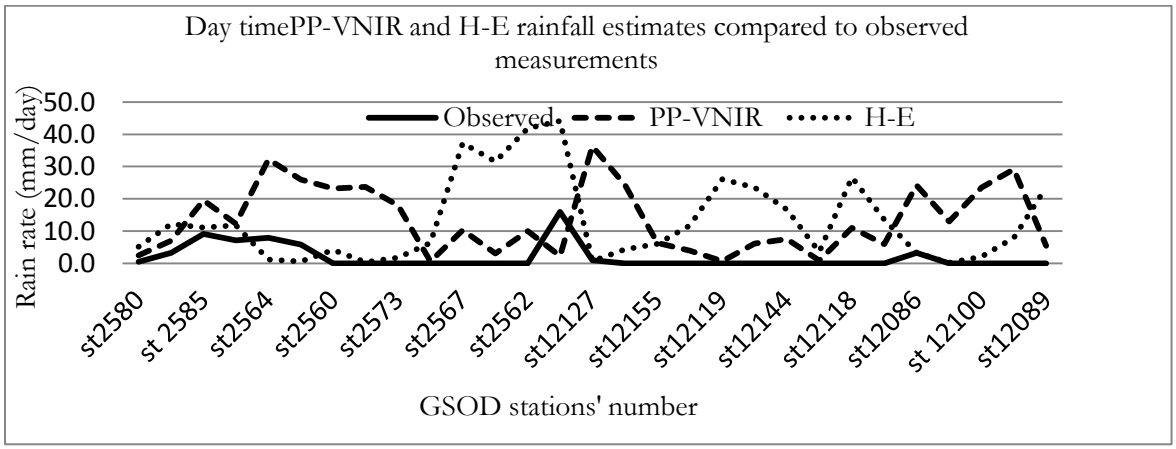

Figure 23: PP-VNIR and H-E compared to observed rain gauge measurements for NW Europe region on 3rd July

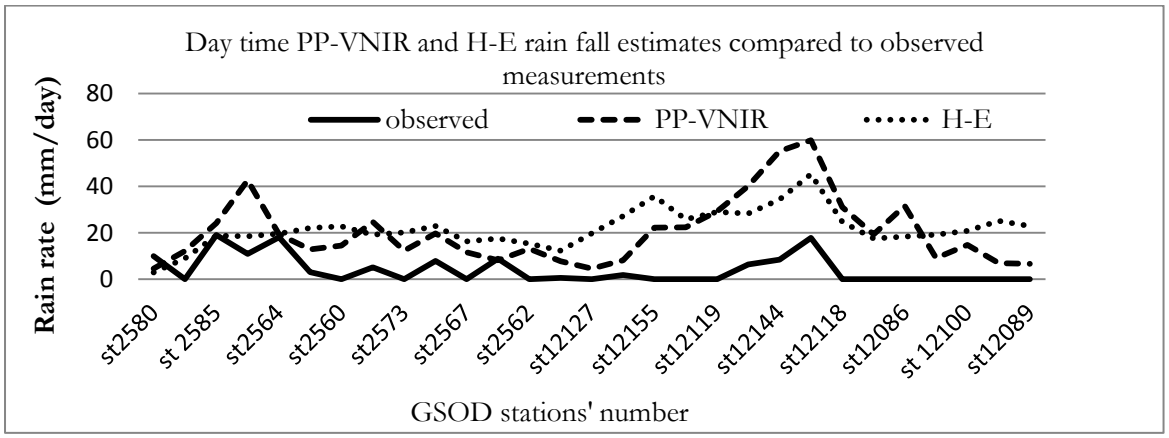

Figure 24: PP-VNIR and H-E compared to observed rain gauge measurements for NW Europe region on 12th July

Table 3: Statistical analysis results on 3rd and 12th July between the algorithms day total estimates and Accumulated rain gauge measurements over part of NW Europe

	3rd July		12th July	
	Obs/ PP-VNIR	Obs/H-E	Obs/ PP-VNIR	Obs/H-E
RMSE	15.70	47.54	20.67	41.65
Bias	0.14	0.04	0.20	0.10
Correlation	0.41	0.55	0.68	0.53
Computed t-test	2.35	3.42	5.12	3.47
Tabulated t-test	2.05	2.05	2.05	2.05

5.1.2. Comparison of PP-VNIR and H-E rain rate estimates over NW Europe.

Further qualitative comparison between the algorithms estimates of rainfall was done through time series line and scatter plots. Quantitative comparison was done through continuous statistical analysis of Bias, RMSE and correlation coefficient.

Qualitative Comparison:

To find out whether there was any association of the two algorithms in rainfall estimates, line and scatter plots were used of the algorithms' rain rate and CPP cloud properties temporal variations was used for understanding the PP-VNIR variations.

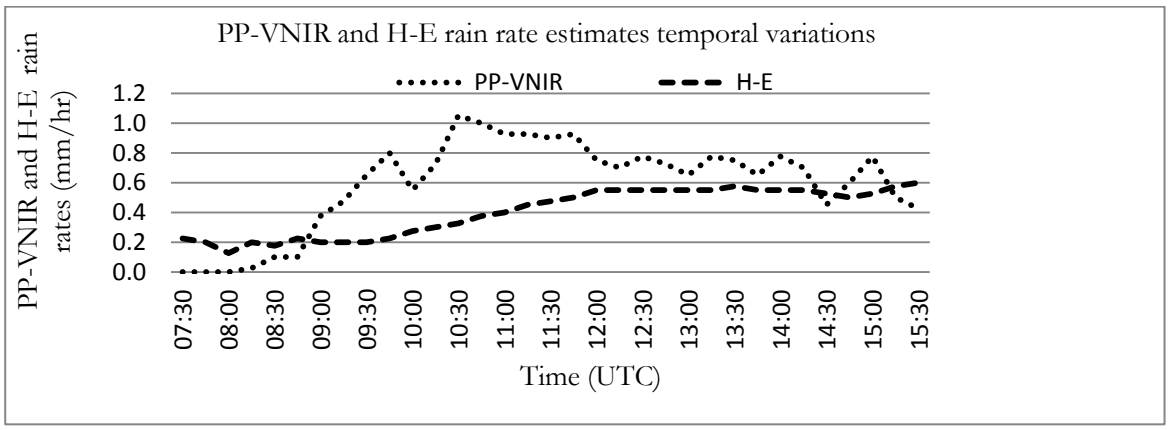

Figure 25: H-E and PP-VNIR day time rainfall estimates on 3rd July line plot over NW Europe from 0730 UTC to 1530 UTC

Results of the rain rate time series (Figures 25 and 27) indicate similar trend though PP-VNIR rain rate indicates fluctuations and over estimation particularly in the morning. These differences was indicated in the scatter plot by spatial variations being greatest in the morning hours and improved in the afternoon.(Figures 26 and 28) particularly on 3rd July. As can be seen from the PP-VNIR cloud properties, the COT on 3rd July was low in the morning and increased gradually toward afternoon (Figure 29). On 12th July it was the reverse. The COT was high in the morning and lowest in the afternoon (Figure 30), hence the two algorithms indicated a decrease in rain rate toward afternoon. The results show that, the two algorithms are comparable in retrieving rain rate in the afternoon.

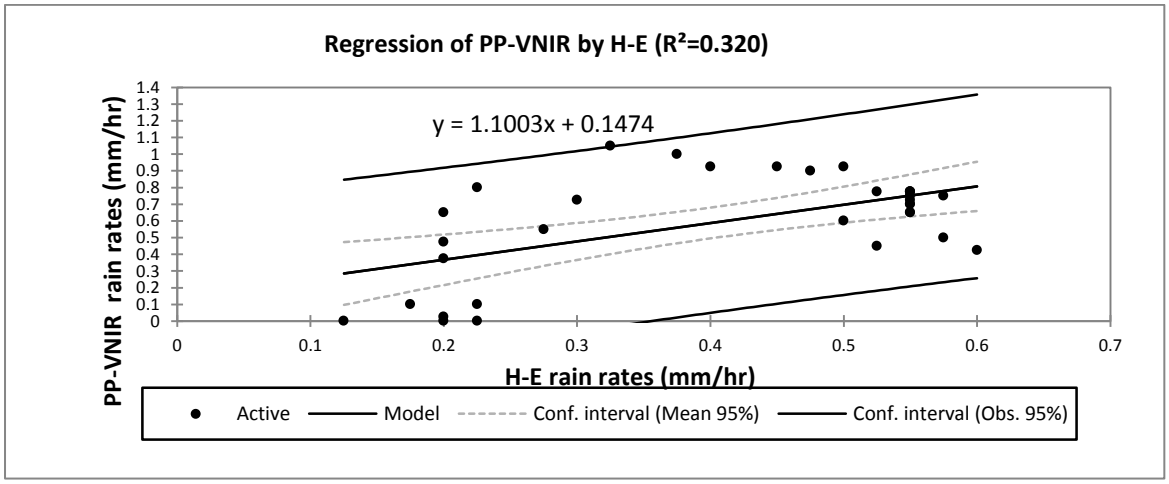

Figure 26: H-E and PP-VNIR day time rainfall estimates on 3rd July scatter plot over NW Europe from 0730 UTC to 1530 UTC

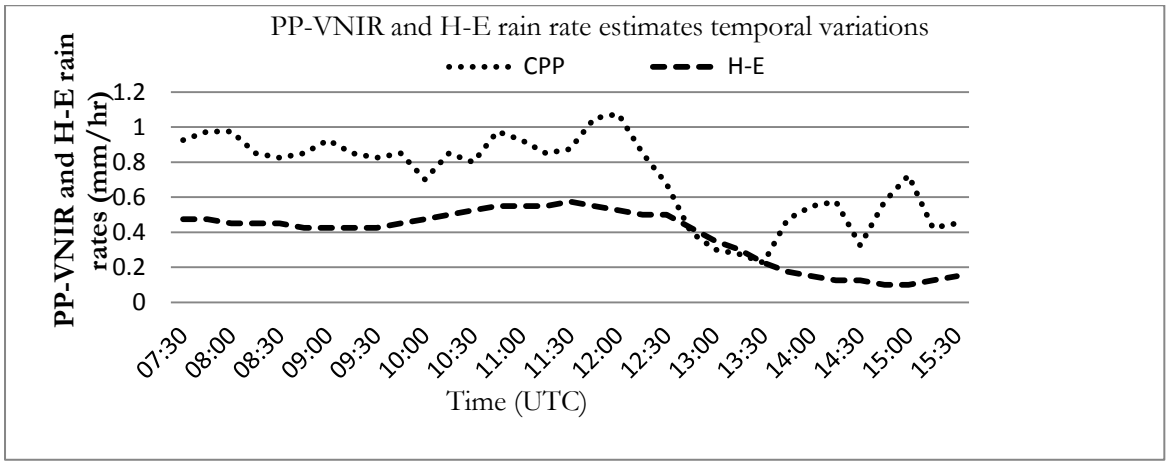

Figure 27: H-E and PP-VNIR day time rainfall estimates on 12th July line plot over NW Europe from 0730 UTC to 1530 UTC

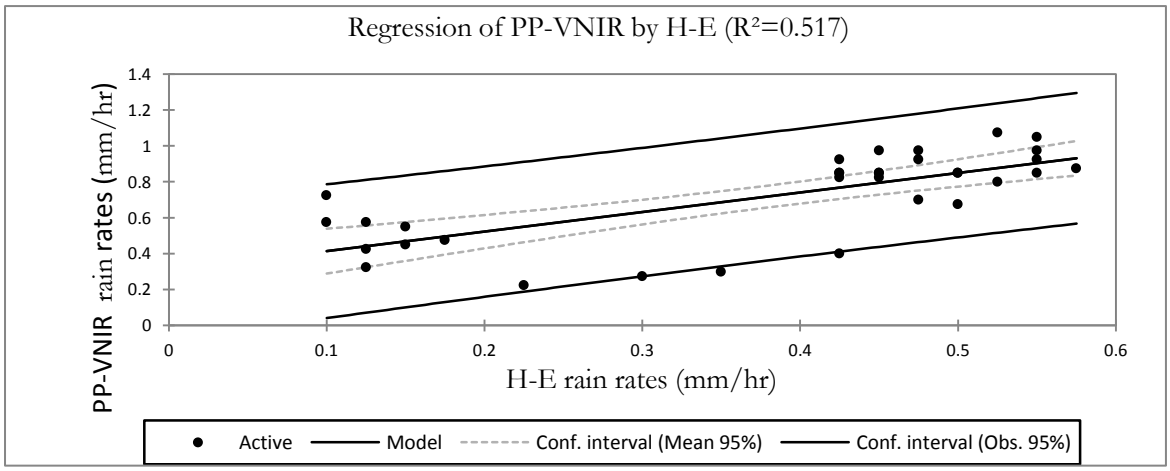

Figure 28: H-E and PP-VNIR day time rainfall estimates on 12th July line plot over NW Europe from 0730 UTC to 1530 UTC

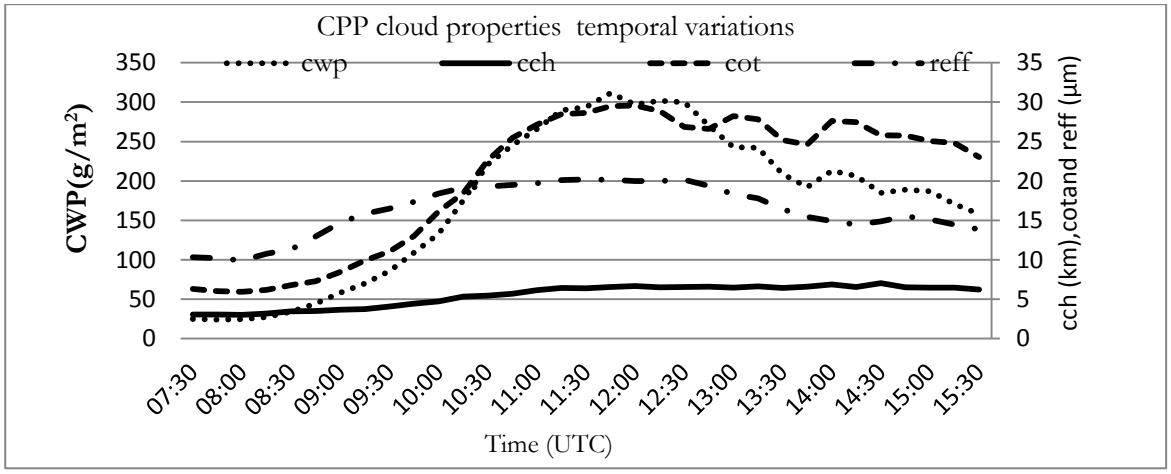

Figure 29: CPP cloud properties temporal variations line curves on 3rd July over NW Europe.

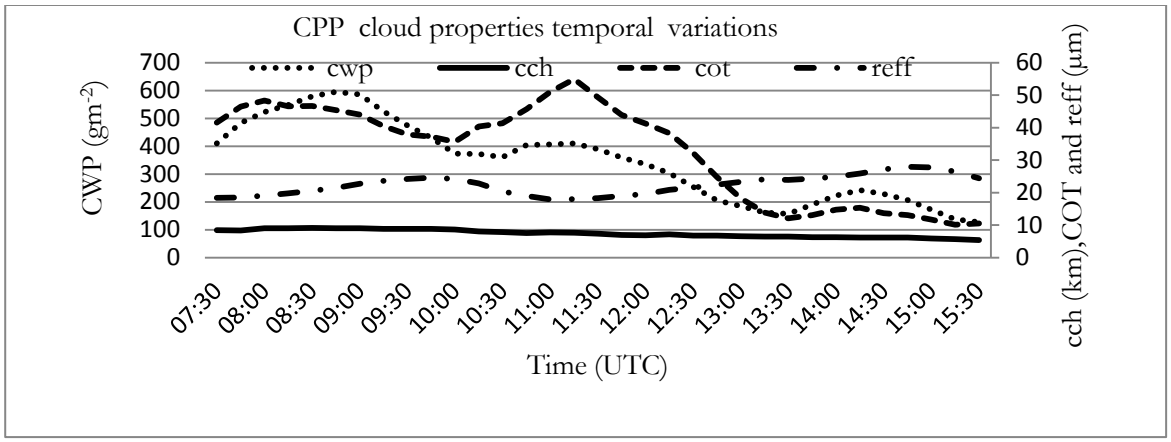

Figure 30: CPP cloud properties temporal variations line curves on 12th July over NW Europe.

Quantitative comparison:

The PP-VNIR rain rate retrieval was compared with that of H-E by use of continuous statistical analysis. From the scatter plot and the statistical results (Table 4), determination of the relationship of the two algorithms was done from which a linear regression best line was fit (Tables 5&6). The correlation was significant and higher on 12th July than on 3rd July. This corresponded with higher RMSE and low Bias.

Table 4: Statistical analysis results for NW Europe region on comparison of PP-VNIR and H-E day rainfall estimates after every 15minutes

PP-VNIR /H-E rain rate temporal variations comparison(0730 -1530 UTC)		3rdJuly	12th July
	RMSE	0.02	2.28
	BIAS	1.47	1.89
Correlation (ρ)		0.57	0.72
Computed t-test		3.82	5.76
Tabulated t-test		2.04	2.04

A linear regression line was fit between the two algorithms values of every 15 minutes from 0730 to 11530 UTC. The probability (P) value was used for testing the hypothesis at alpha=0.05.

Table 5: Linear regression best fit line statistics on 3rd July

Goodness of fit statistics:						
Observations	Sum of weights	Df	R^2	Adjusted R^2	MSE	RMSE
33	33.00	31.00	0.32	0.30	0.07	0.26
Analysis of variance:						
Source	DF	Sum of squares	Mean squares	F	Pr > F	
Model	1.00	0.98	0.98	14.58	0.00	
Error	31.00	2.09	0.07			
Model parameters:						
Source	Value	Standard error	t	Pr > |t|	Lower bound (95%)	Upper bound (95%)
Intercept	0.15	0.12	1.18	0.25	-0.11	0.40
H-E	1.10	0.29	3.82	0.00	0.51	1.69
Equation of the model: PP-VNIR = 0.15+1.10*H-E						

The p (probability) value states the confidence that one can have in the estimated values being correct. R^2 and adjusted R^2 are estimates of the "goodness of fit" of the line .They represent the % variation of the data explained by the fitted line. $p<0.05$ (alpha=0.05) was used to test the hypothesis and since on both days the "p" value was very small hence the algorithm comparisons were statistically significant at level alpha. The "R" values were quite high and very low standard error. As from previous analysis of line and scatter plot, the regression statistics improved on 12th July. This was indicated by higher R^2, adjusted R^2 and t-test while the RMSE was correspondingly low.

Table 6: Linear regression best fit line statistics on 12th July

Goodness of fit statistics:						
Observations	Sum of weights	Df	R^2	Adjusted R^2	MSE	RMSE
33	33.00	31.00	0.52	0.50	0.03	0.17
Analysis of variance:						
Source	DF	Sum of squares	Mean squares	F	Pr > F	
Model	1.00	0.98	0.98	33.15	< 0.0001	
Error	31.00	0.92	0.03			
Model parameters:						
Source	Value	Standard error	t	Pr > |t|	Lower bound (95%)	Upper bound (95%)
Intercept	0.30	0.08	3.89	0.00	0.15	0.46
H-E	1.09	0.19	5.76	< 0.0001	0.70	1.48
Equation of the model: PP-VNIR = 0.30+1.09*H-E						

5.2. Kenya Region results

Day total rainfall estimates for the H-E (Figures 31 and 33) and PP-VNIR (Figures 32 and 34) algorithms and their intermediate maps are shown. The dates of the events were 20100402 and 20100403 from 0730 UTC to 1530 UTC on 15 minutes time step. Due to PP-VNIR inability to retrieve rain rate in the morning and late afternoon in this region, 0730 and 1430 -1530 UTC were not included in the retrieval analysis. Figure 31 show the convective and non-convective rain rate coexistence with more rain rate to the western and eastern side of the country. The false colour composite maps agree with total H-E rain rate in location and area covered by the precipitating clouds. The southern and central regions of the country were dominated by cirrus and low water clouds. Figure 32 shows coexistence of ice and water clouds and the PP-VNIR rain rate was mainly from ice cloud. The rain rate location agrees with the false colour map composites to the western, eastern and partially to the central region location but differed in intensities.
Figure 32 shows the PP-VNIR rain rate was mainly from ice clouds with corresponding high cch, COT and correspondingly high CWP. The PP-VNIR delineation of precipitating clouds differed with the colour map composites in that, the central regions was mainly of cirrus clouds which were not precipitating. These were the only areas that the PP-VNIR differed with the H-E over this region due to its inability to differentiate cirrus clouds as non-precipitating clouds.
It is clear from the algorithm and the false colour composite maps that over this region most of the rains comes from the western, central and eastern side of the country

Detection Validation

PP-VNIR and H-E day total rainfall estimates were compared with rain gauge measurements station by station. By use of contingency table the corresponding rainy and non-rain days were determined. Daytime rainfall total for each region by each algorithm was used to compare with the 31 stations (Appendix18 and 19) accumulated rain gauge measurements. The choice of the stations used was based on availability of information on rainfall for the days of study.

Figure33 and 34 indicates the two algorithms detection of precipitating clouds to be similar in location but differed in area covered. H-E was more in agreement with the false colour composites maps in location and area covered by rain rate. The PP-VNIR (Figure 36) shows ability to detect precipitating clouds to the central region where it was more of water clouds. Tables' showing the various scores of detection by each algorithm in relation to observed values and the overall accuracy in percentage. Line plot were also used to describe the relationship of each algorithm with the observed values. Contingency table and their probability scores used in determination of detection capability of each algorithm in relation to the rain gauge measurements (observed) are shown in table 7.

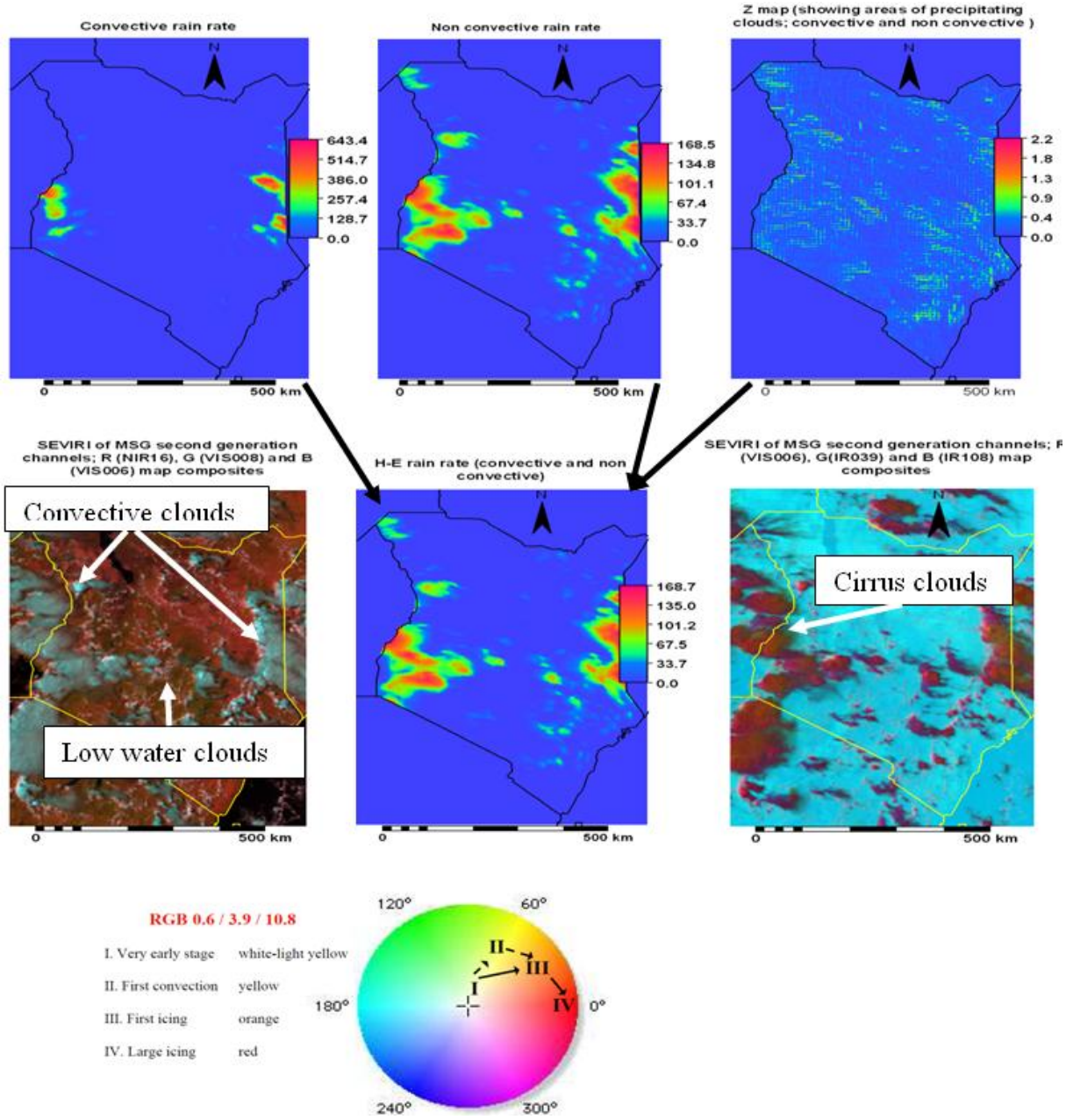

Figure 31: H-E day total rainfall, input maps and 1315 UTC false colour composite maps all in geostationary MSG projection over Kenya on 2nd April 2010.

Retrieval validation;

In this section results of rainfall estimates of each algorithm in relation to observed values are given.

The satellite foot print was increased to 5x5 kernel area from which average values were determined. This were compared to accumulated rain gauge measurements assuming the 5x5 pixel box represented the area covered by each rain gauge. The difference in detection capability by the two algorithms over this region was clear (Figure 35 and 36). It increased for both algorithms with increase in rain rate on 3rd April. The FAR and Bias were very high on 2nd for both algorithms with PP-VNIR having the highest and correspondingly the CSI was very low. On 3rd April when rain rate increased, this effect was reduced The CSI increased from 0.04 and 0.06 for PP-VNIR and H-E consecutively to 0.33 and 0.35 with increase in rain rate and likewise the POR increased from 0.27 and 0.43 to 0.45 and 0.64. Comparison with the rain gauge measurements curves (Figure 37 and 38) show the two algorithms had a similar trend with rain gauge measurements with a delay which improved with increase in rain rate on 3rd April. The algorithms

rain rate was also higher than the rain gauges measurements. Both had low correlation with rain gauges measurements and RMSE decreased with increase in rain rate on 3rd April. Bias increased mostly for PP-VNIR with increase in rain rate. The satellite estimates lag (delay) is associated with parallax error.

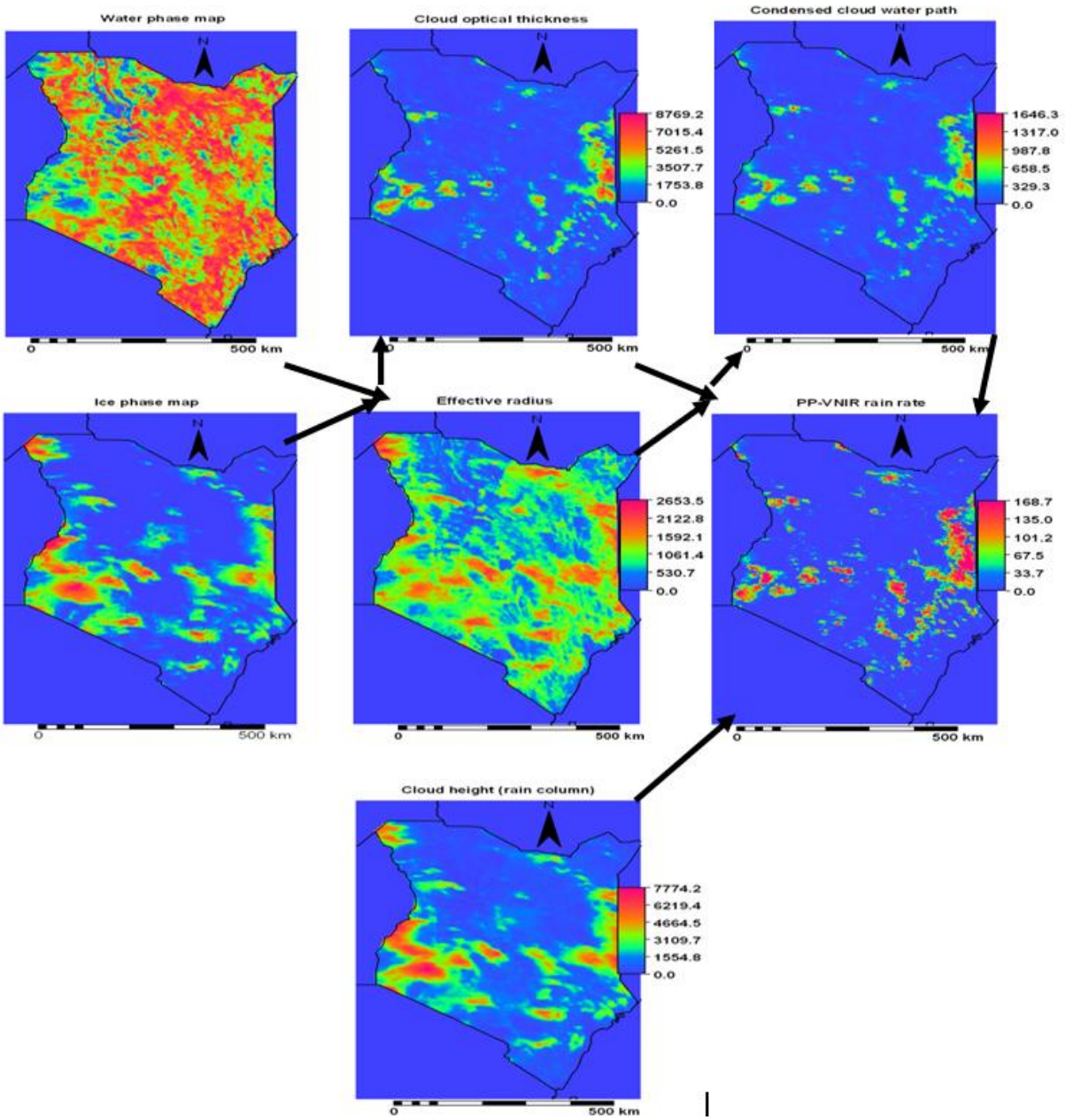

Figure 32 H-E day total rainfall and input maps in geostationary MSG projection over part Kenya on 2nd April 2010.

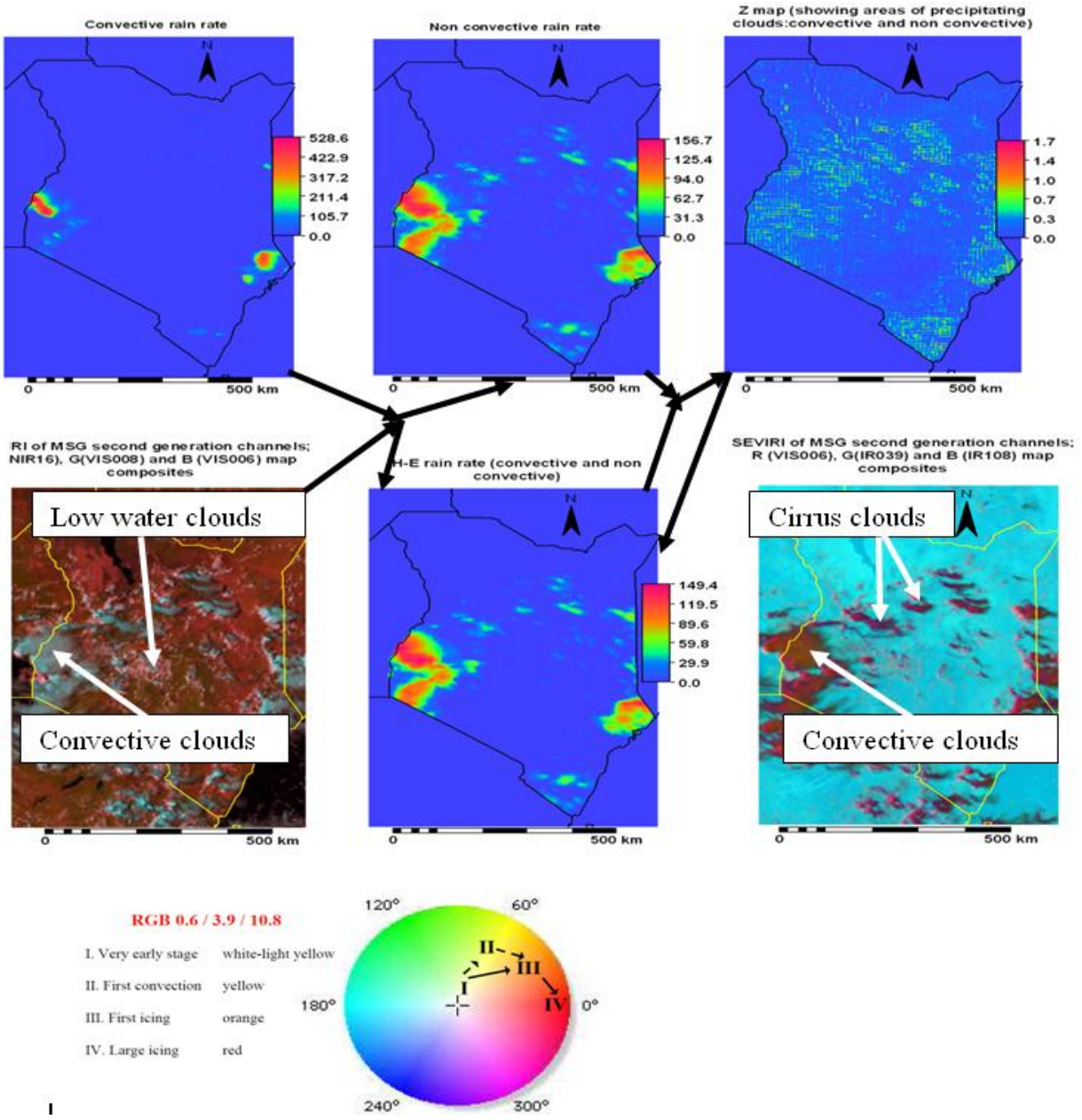

Figure 33: H-E day total rainfall, input maps and 1315 UTC false colour composite maps all in geostationary MSG projection over Kenya on 3rd April 2010.

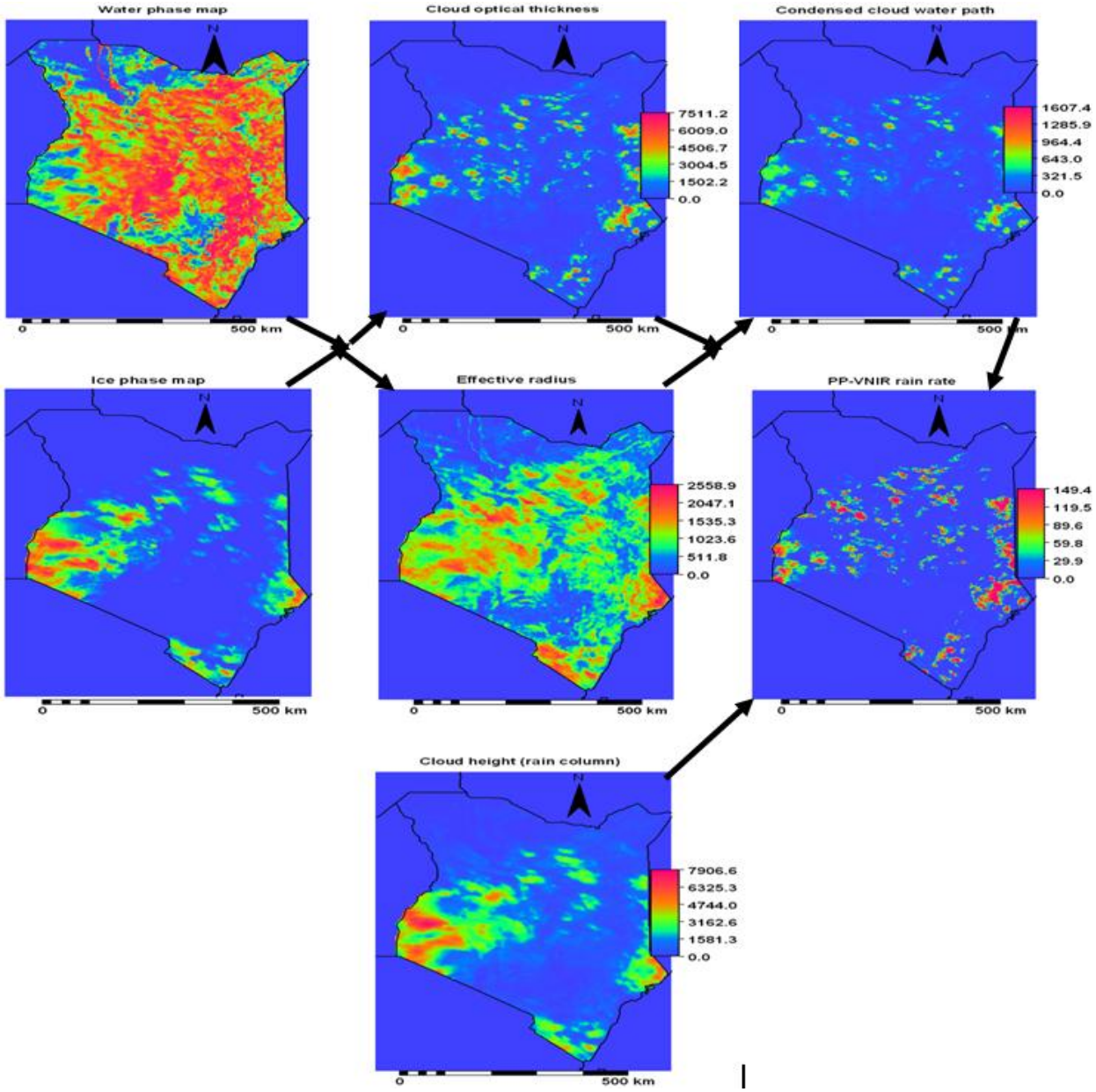

Figure 34: PP-VNIR day time total rain rate and cloud properties day average values over Kenya on 3rd April 2010

Table 7: Contingency table of the daily total rainfall estimates by PP-VNIR and H-E algorithms and accumulated rain gauge measurements over Kenya

2ndApril							
Estimated Rain rate by PP-VNIR	Observed by rain gauges			Estimated Rain rate by H-E	Observed by rain gauges		
	Rain	No rain	Total		Rain	No rain	Total
Rain	1	22	23	Rain	1	17	18
No rain	0	8	8	No rain	0	13	13
Total	1	30	31	Total	1	30	31
3rdApril							
Estimated Rain rate by PP-VNIR	Observed by rain gauges			Estimated Rain rate by H-E	Observed by rain gauges		
	Rain	No rain	Total		Rain	No rain	Total
Rain	7	12	19	Rain	6	8	14
No rain	2	10	12	No rain	3	14	17
Total	9	22	31	Total	9	22	31

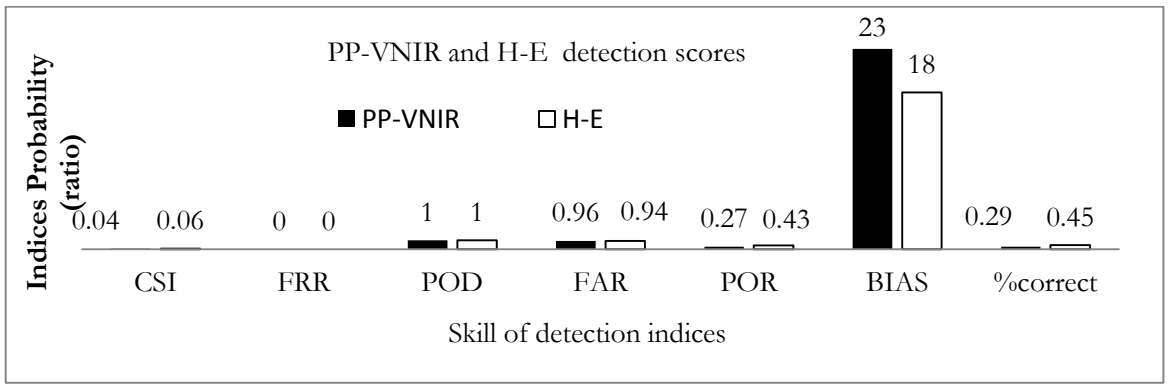

Figure 35: Skill of detection bar graphs for PP-VNIR and H-E algorithms on 2nd April

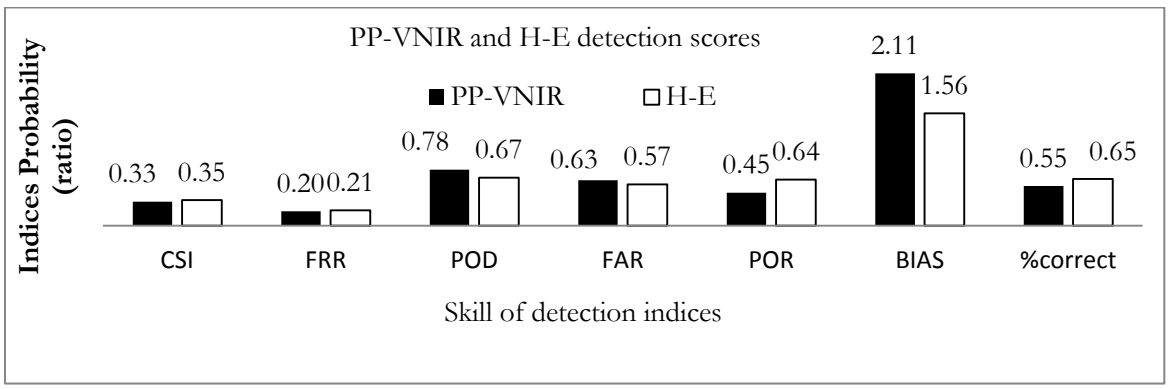

Figure 36: Skill of detection bar graphs for PP-VNIR and H-E algorithms on 3rd April

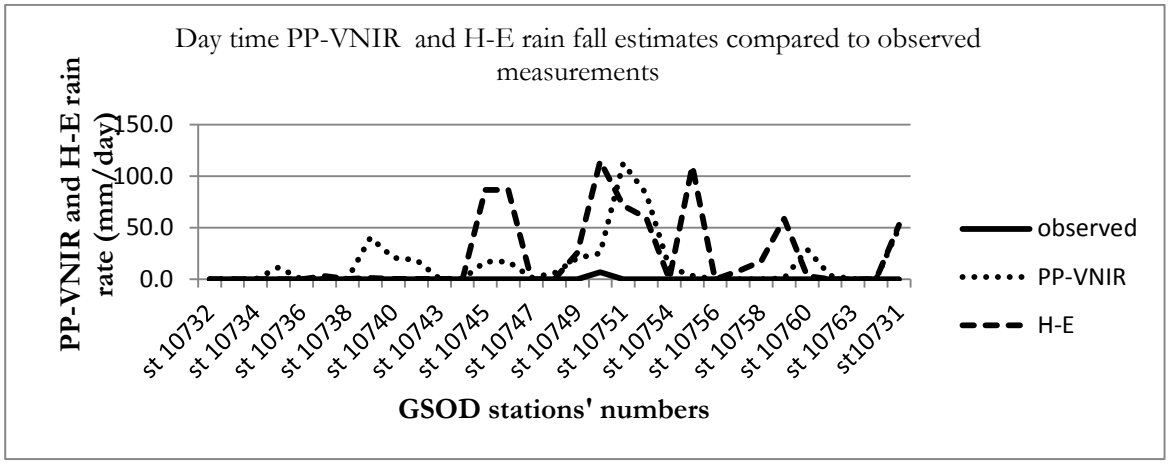

Figure 37: PP-VNIR and H-E compared to observed rain gauge measurements for Kenya region on 2nd April

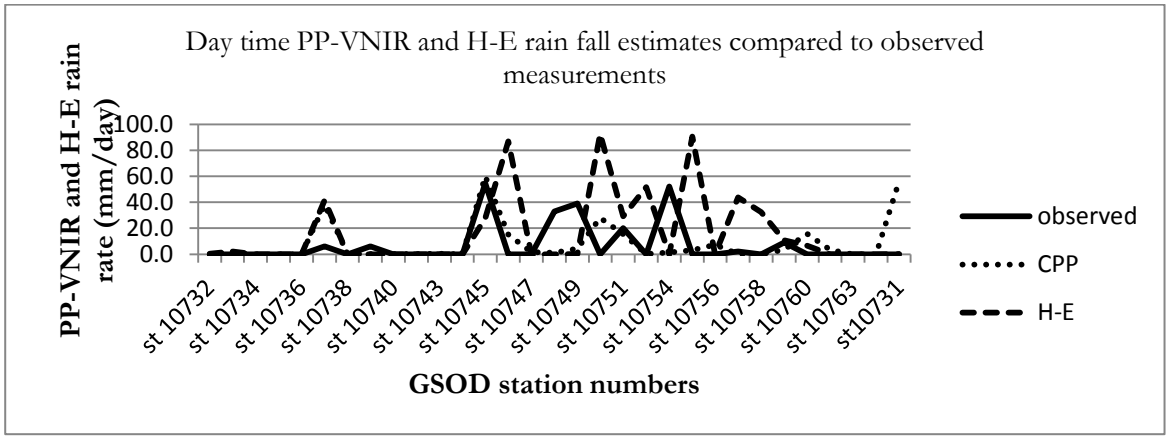

Figure 38: PP-VNIR and H-E compared to observed rain gauge measurements for Kenya region on 3rd April

Table 8: Statistical analysis results on 2nd and 3rd April between the algorithms day total estimates and Accumulated rain gauge measurements over Kenya.

	2nd April		3rd April	
	Obs/PP-VNIR	Obs/H-E	Obs/PP-VNIR	Obs/H-E
RMSE	30.43	43.35	21.95	35.86
Bias	0.01	0.01	0.66	0.32
Correlation	0.15	0.48	0.11	0.07
Computed t-test	0.80	2.87	0.59	0.38
Tabulated t-test	2.04	2.04	2.04	2.04

5.2.1. Comparison of rain rate estimates by PP-VNIR and H-E over Kenya

This section shows the analysis results of the comparison between PP-VNIR and H-E rainfall estimates over Kenya. Line and scatter plots were used to establish whether there was any relationship between

them PP while continuous statistics of Bias, RMSE and correlation were used to compare their rain rate rain rate. Linear regression statistics was used to determine the significance of the relationship.

Qualitative Comparison:

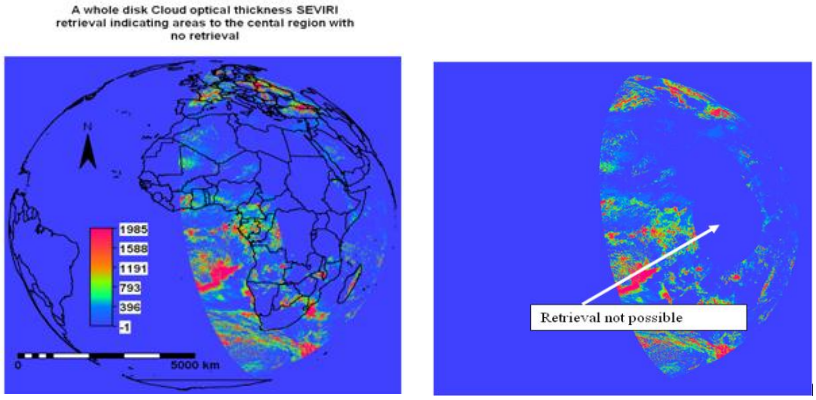

Figure 39: An image of CPP retrieval (example. of COT (μm)) of whole MSG disk retrieval at 0730 UTC on 3rd April

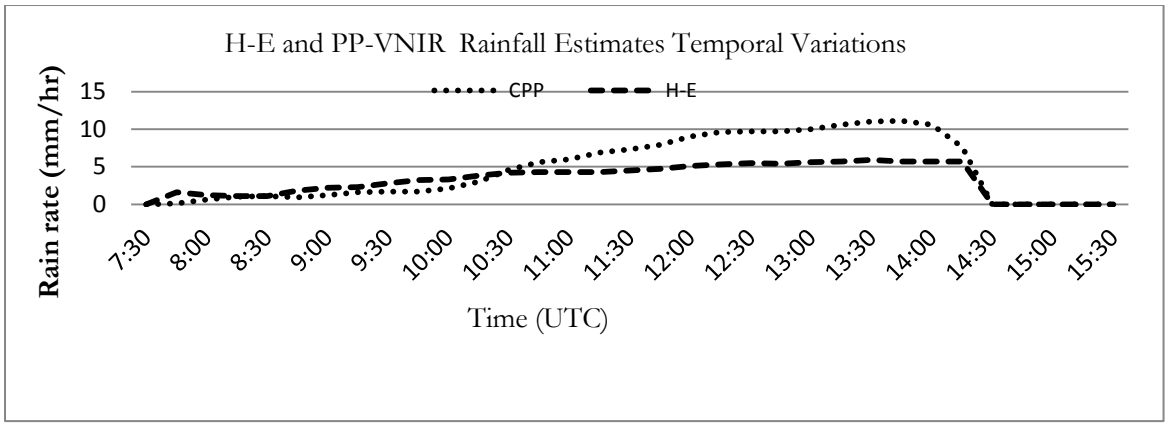

Figure 40: PP-VNIR and H-E daylight rainfall estimates time series plot on 2nd April over Kenya region from 0745 UTC to 1415 UTC

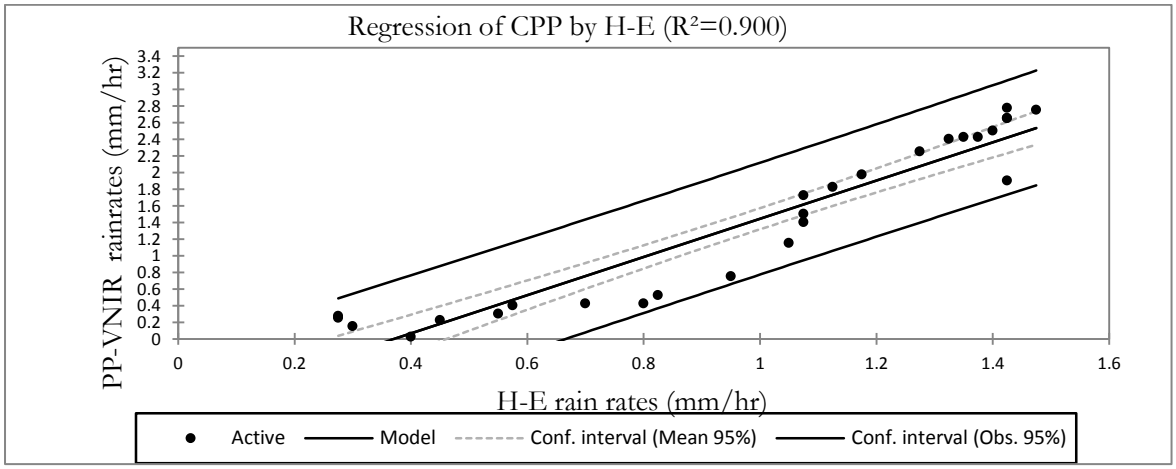

Figure 41: PP-VNIR and H-E daylight rainfall estimates scatter plot on 2nd April over Kenya region from 0745 UTC to 1415 UTC

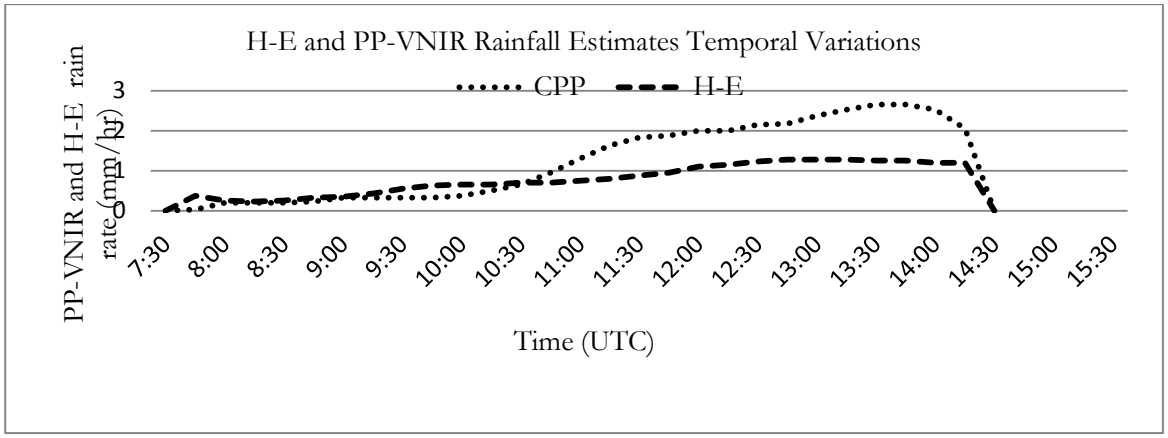

Figure 42: PP-VNIR and H-E daylight rainfall estimates time series plot on 3rdApril over Kenya region from 0745 UTC to 1415 UTC

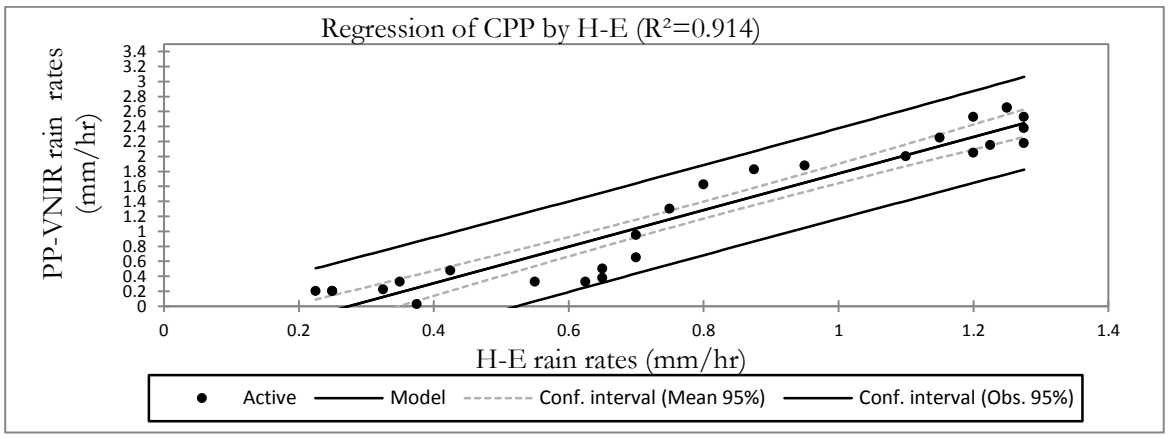

Figure 43: PP-VNIR and H-E daylight rainfall estimates scatter plots curves on 3rd April over Kenya region from 0745 UTC to 1415 UTC

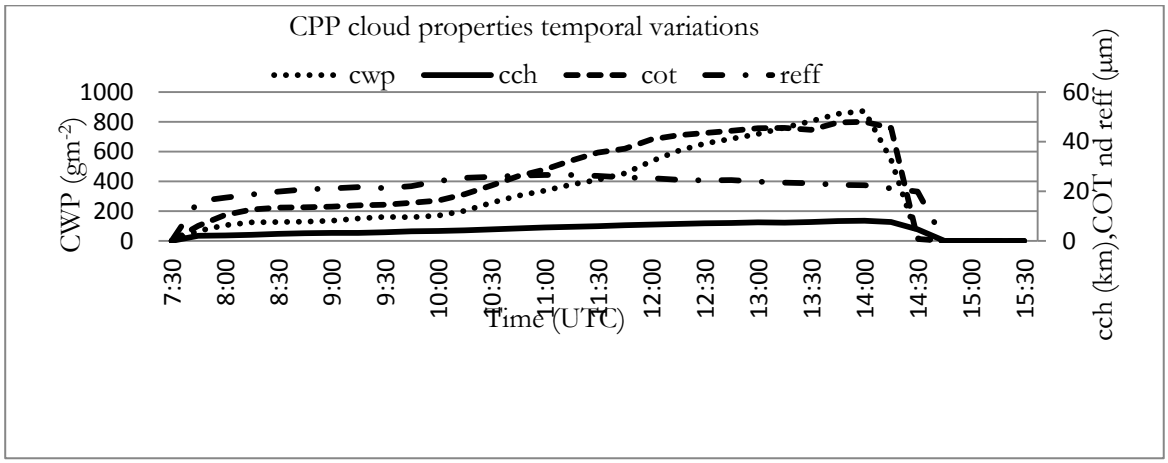

Figure 44: CPP cloud properties day average temporal variations curves on 2nd April over Kenya

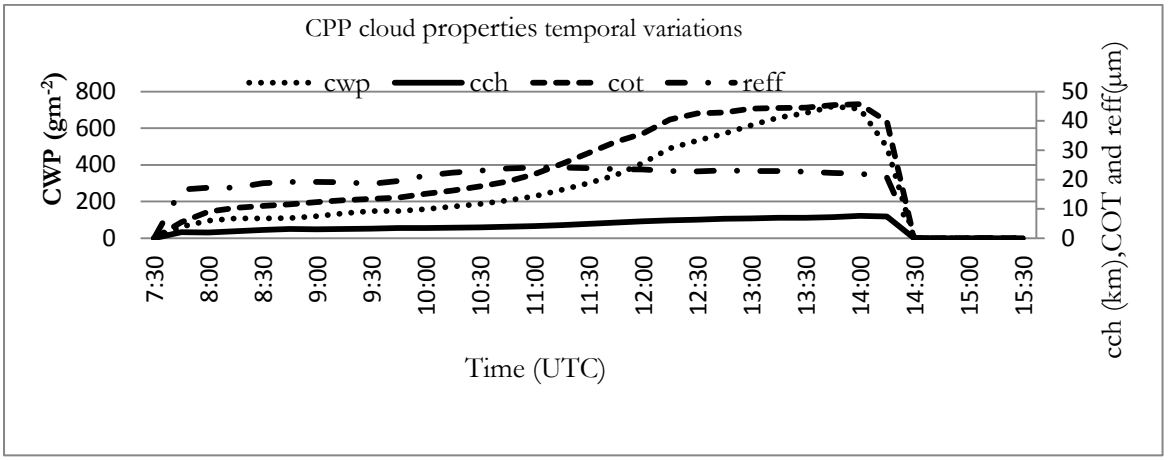

Figure 45: CPP cloud properties day average temporal variations curves on 3rd April over Kenya

Comparison of the two algorithms in rain rate retrieval show close agreement particularly in the morning though PP-VNIR had higher rain rate over H-E mostly in the afternoon (Figures 40 and 42). The scatter plots (Figure 40 and 42) show spatial variation in the morning and close agreement in the afternoon for both 2nd and 3rd April. The CPP cloud properties show similar trend of increasing trend from morning toward afternoon and had an abrupt decrease in the late afternoon due to inability of CPP to retrieve cloud properties.

Quantitative comparison:

The PP-VNIR rain rate was further compared quantitatively with the H-E by use of statistical analysis. The relationship between the algorithms rain rate, was tested for significance by use of linear regression statistics. The correlation between the algorithms rain rate retrieval was very high and significant on 2nd April (0.94) and it increased further to 0.95 with increase in rain rate on 3rdApril. The RMSE and Bias however rose slightly.

Table 9: Statistical analysis results for Kenya region on comparison of PP-VNIR and H-E day rainfall estimates after every15 minute

		2ndApril	3rdApril
PP-VNIR /H-E rain rate temporal variations comparison(0745 -1415 UTC)	RMSE	2.9	3.06
	Bias	1.43	1.57
Correlation (ρ)		0.94	0.95
Computed t-test		15.15	15.23
Tabulated t-test		2.06	2.06

The tabulated t-test or critical value at 95% confidence level on 2nd and 3rd April were greater than the critical values. The null hypothesis was therefore rejected and the alternative hypothesis accepted over Kenya region.

Regression analysis

The p (probability) value states the confidence that one can have in the estimated values being correct. R^2 and adjusted R^2 estimate of the "goodness of fit" of the line. They represent the % variation of the data explained by the fitted line. If the "p" value is greater than alpha (0.05) at 95% confidence level the Null hypothesis, H_0: $\rho = 0$ is accepted otherwise the alternative hypothesis, H_1: $\rho \neq 0$ is accepted.

From table 10 and 11 of regression statistical results, show that at 95% confident level the probability that there was no significant relationship between the two estimates was very low hence the null hypothesis was rejected and the alternative hypothesis that there was a significant relationship was taken. The R^2 and the adjusted R^2 was very high for both days and consequently the RMSE was also very low.

Table 10: Linear regression best fit line statistics on 2nd April

Goodness of fit statistics:						
Observations	Sum of weights	Df	R^2	Adjusted R^2	MSE	RMSE
27	27	25	0.90	0.90	0.10	0.32
Analysis of variance:						
Source	DF	Sum of squares	Mean squares	F	Pr > F	
Model	1.00	22.97	22.97	223.95	< 0.0001	
Error	25.00	2.56	0.10			
Model parameters:						
Source	Value	Standard error	t	Pr > |t|	Lower bound (95%)	Upper bound (95%)
Intercept	-0.85	0.16	-5.21	< 0.0001	-1.19	-0.51
H-E	2.29	0.15	14.96	< 0.0001	1.98	2.61
Equation of the model: PP-VNIR = -0.85+2.29*H-E						

Table 11: Linear regression best fit line statistics on 3rd April

Goodness of fit statistics:						
Observations	Sum of weights	Df	R^2	Adjusted R^2	MSE	RMSE
27	27	25	0.91	0.91	0.08	0.29
Analysis of variance:						
Source	DF	Sum of Sq.	Mean sq.	F	Pr > F	
Model	1	21.88	21.88	265.98	< 0.0001	
Error	25	2.057	0.082			
Model parameters:						
Source	Value	Std error	t	Pr > |t|	Lower bound (95%)	Upper bound (95%)
Intercept	-0.67	0.13	-5.08	< 0.0001	-0.94	-0.40
H-E	2.44	0.15	16.31	< 0.0001	2.13	2.75
Equation of the model: PP-VNIR = -0.67+2.44*H-E						

5.3. Discussion

5.3.1. Northwest Europe region

Detection validation

H-E precipitating cloud detection was in agreement with the map composites but non-convective rain rate was underestimated. The under estimation was attributed to water clouds being of low temperature in agreement with what Scofield & Kuligowski (2003) found, that H-E tend to underestimate warm clouds above -58^{0}C and over estimates below -58^{0}C. Comparison with rain gauge measurements indicates high POD hence low FRR which was attributed to high spatial resolution of the satellite. The POR was also low and correspondingly high Bias resulting from point rain gauge measurements which could not characterise the highly variable rainfall.

PP-VNIR algorithm in detection of precipitating clouds considers water and ice phase separately. Due to its high brightness temperature of separating the two phases (265K)(Roebeling & Holleman, 2009) the delineation of precipitating clouds had spatial variations to that of H-E which had a limitation of 250K for non-convective rain rate and about 240K for convective rain rate (Scofield & Kuligowski, 2003). It is noted that PP-VNIR delineation of precipitating clouds was in areas where water phase and ice phase coexisted. This is in line with its principle of considering large water droplets and high thick clouds to be associated with more rain rate. The two had agreement in detection in ice clouds due to low a temperature which was considered by both to be favourable for more rain rate. The POD, FRR Bias and POR were the same as the H-E. Increase in rain rate on 12th July, had the two algorithm CSI increase from 0.31 to 0.45 and correspondingly a reduction of Bias from 3.22 to 2.23 on the two eventful days. This was associated with the rain gauges ability to capture most of the rainfall reaching the ground with increase in rain rate. The results of the comparison in terms of line curves (Figure 23 and 24) indicate high rain rate by the algorithms as compared to rain gauge measurements. The algorithms however showed same trend with rain gauges particularly on 12th July when the rain rate increased but with a lag which was attributed to parallax error in the SEVIRI images. Over this region good distribution of rain gauges were able to characterise the variable rainfall reasonably well. This was also attributed to increase of the satellite foot print to 5x5 kernel areas.

Retrieval accuracy

Statistical analysis showed that PP-VNIR retrieval capability increased with increase in rain rate but the opposite was true for H-E. This was attributed to the fact that the H-E considered convective and non-convective rain rate separately and it underestimates stratiform. Depending on which rainfall type is dominant the H-E retrieval accuracy varies. PP-VNIR on the other hand considers cloud microphysics instead of rainfall type. Of importance to note is that the rain gauges distribution coupled with increase in satellite foot print resulted into rain gauges been more representative of the variable rainfall hence the two algorithms correlation was reasonably high and significant.

Comparison of the algorithms in retrieval over NW Europe

Qualitative comparison of rain rate show the two algorithms agreed in general trend but differed in intensity particularly in the morning due to their differences of stratiform rain rate retrieval. This was seen in the time series plot. The scatter plot indicated spatial variation which was again a contribution from stratiform rain rate differences. The study showed COT of CPP cloud properties to have great influence in PP-VNIR rain rate since it is directly related to CWP and cch. This means the higher the cloud height the more the rain rate. H-E considers clouds which are high to give more rain rate due to their cold temperatures. This agreement brings the two algorithms to have the same trend as depicted by the CWP and COT. The correlation between the two algorithms in retrieval was significant and increased with increase in rain rate from 0.57 on 3rd July to 0.72 on 12th July.

Regression statistics shows that the two algorithms relationship was significant at 95% confident level. The significance increased with increase in rain rate as indicated by R^2 increase from 0.32 to 0.52.

5.3.2. Kenya region

Detection validation

The delineation of precipitating clouds by the algorithms was well defined which was associated with convective systems being dominant over the region during the rainy season and reduction of stratiform clouds which the two algorithms differed in detection. H-E delineation was in agreement with false map composites in location and area on both days in April. The PP-VNIR differed with false colour map composite by inclusion of cirrus clouds which are cold but not precipitating. Comparison with the rain gauge measurements indicated very high Bias particularly for PP-VNIR algorithm on 2nd April which reduced with increase in rain rate on 3rd April. High Bias for the algorithms was associated with rainfall variability which could not be characterized by the sparse rain gauge distribution (Prigent, 2010). Detection accuracy increased with increase in rain rate as depicted by the bar graphs (figure 35 and 36), and is reflected by the drop of over estimation (Bias) by the algorithms. The increase in rain rate however resulted into more cirrus development which coexists in deep convections as anvil. The H-E reduces this cirrus effect hence the bias was less. FAR was very high on 2nd and reduced on 3rd April. This was associated with the rain gauge sparse distribution which could not characterise the highly variable rainfall. Over Africa sparse rain gauge distribution is common (Grimes, 2008) but with increase in rain rate, this effect is reduced because rainfall variability is reduced. Rain gauges measurements were also affected by topography, wind, and gauge design (Barrret & Martin, 1981). Gauges representation of the variable rain fall depends upon slope, aspect, elevation, and location in relation to hills and ridges. The Kenya highlands are located to the central region of the country and they contributed to the discrepancy between satellite detection of rain rate to that of the rain gauge measurements. The POD reduced and consequently the POR increased. This was due to parallax effect which was also well reflected in line curves (Figure 37 and 38) where the algorithm indicated close trend with rain gauge measurements but with a delay.

Retrieval accuracy

PP-VNIR algorithm showed closer relationship with the rain gauges which was also reflected in statistical analysis of RMSE being lower than that of H-E (Table 8). The correlation was however low and insignificant due to sparse rain gauges distribution which even on increasing the foot print of the satellite could not characterize rainfall variability. This shows that good rain gauge distribution is a necessity in improving validation. The PP-VNIR was affected by CPP retrieval of cloud properties failure in the morning and late afternoon due to low sun angle (Figure 39). This led to retrieval comparison of the algorithm to be restricted to 0745 to 1415 UTC time steps.

Comparison of the algorithms in retrieval over Kenya

Comparison of the two algorithms in retrieval of rain rate by line (Figure 40 and 42) plot show the two had close agreements in retrieval in the morning and differed late in the afternoon. The difference in the afternoon was due to PP-VNIR cirrus effect which coexists with convective systems and was considered to be precipitating. Unlike the NW Europe where the spatial variation was large, over this region it was low (Figure 41 and 43) and this was due to absence of stratiform rainfall over this region which the two algorithms differed in retrieval. Convective rainfall is more dominate over the tropics due to ITCZ effect. The CPP cloud properties had a consistent trend. The CWP, COT and cch showed increases with time (figure 44 and 45). This is what was expected over this region since convective systems develop gradually to maximum in the late afternoon when sun angle is high. The effective radius decreased during late afternoon due to intense heating that led to evaporation at the cloud base hence decrease in effective radius. This is in line with what McCollum& Ba (2000) found over central Africa that in satellite

estimates, evaporation of small rain drops is very high over the continental areas. This effect is enhanced more by the intense heating over the tropics. The correlation between their estimates was very high and significant 0.94 and 0.95 on 2nd and 3rd April consecutively.

Regression analysis result showed the relationship of two was significant with R^2 of 0.90 and 0.91 consecutively for the two eventful days.

6. CONCLUSION AND RECOMMENDATIONS

This section presents the conclusions drawn from the study and the future work recommendations.

6.1. Conclusions

Geostationary satellites are especially important for their high temporal (every 15 minutes) and spatial (1-4km at nadir) resolution. This study compared two algorithms, the PP-VNIR and H-E in detection and retrieval of rainfall and validated their results to rain gauge point measurements by use of SEVIRI of Meteosat Second Generation retrievals. Two events from each region in the year 2010 month of July (3rd and 12th) for NW Europe region and month of April (2nd and 3rd) for Kenya region were used for the study. The two algorithms differ in principle. PP-VNIR algorithm is based on use of cloud physical properties while H-E is based on cloud top infrared brightness temperature. The study was carried in two different geographical regions; NW Europe and Kenya regions. They have different weather systems; NW Europe being in temperate climatic zone experiences large frontal systems and convective showers while Kenya being in the tropics experiences deep convective systems resulting from ITCZ during the rainfall seasons. The study was intended to test accuracy of each method in detection in relation to rain gauge measurements and finally compare them to test whether there was any relationship between their estimates and further determine a linear regression of the best line fit. PP-VNIR had been applied successfully in NW Europe (Roebeling & Holleman, 2009) but had one major limitation; it can only be applied during daylight. While H-E is widely used in Northern America for flood forecasting (Scofield & Kuligowski, 2003) and worldwide using geostationary data for rainfall forecast. It has advantage over PP-VNIR by being applicable day and night. Categorical statistics were used for detection test while continuous statistics of Bias, RMSE and correlation were used for rain rate retrieval test. The two regions were considered independently.

To fulfil the main objective, three specific objectives were fulfilled:

Each algorithm detection and retrieval of rain rate was tested in relation to rain gauge measurements at 95% confident level (alpha=0.05) under the null hypothesis that there is no correlation between the compared values, and alternative one that there is correlation between the compared values. The two events from each region were considered together.

PP-VNIR algorithm detection and retrieval capability:

(1) PP-VNIR algorithm can be applied over NW Europe with an overall detection capability of 38%, CSI of 0.38, retrieval precision of 18 mm/day and accuracy of 0.2mm/day with significant correlation of 55% compared to rain gauge measurements. It can be applied over Kenya with an overall detection accuracy of 42%, CSI of 0.2, retrieval precision of 26 mm/day and accuracy of 0.3 mm/day with insignificant correlation of 13%.

H-E algorithm detection and retrieval capability:

(1) H-E algorithm can be applied over NW Europe with an overall detection capability of 38%, CSI of 0.38, retrieval precision of 45 mm/day and accuracy of 0.1mm/day with significant correlation of 54% compared to rain gauge measurements. It can be applied over Kenya with an overall

detection accuracy of 55%, CSI of 0.2, retrieval precision of 40 mm/day and accuracy of 0.2 mm/day with insignificant correlation of 28%.

PP-VNIR and H-E rain rate retrieval comparison:

(2) H-E and PP-VNIR rain rate are comparable over NW Europe with a precision of 0.2 mm/hr and significant correlation of 42%. Over Kenya the two estimates compares at a precision of 0.3 mm/hr and significant correlation of 91%.

Comparison of the two algorithms in rain rate retrieval was significantly good over NW Europe and very high over Kenya. There was close agreement in detection of rain rate between the algorithms hence H-E can fill the gap of PP-VNIR night time estimates. The PP-VNIR has another limitation of cloud physical properties from which it derives its rain rate are not retrievable in the morning and late afternoon over Kenya. From this study it was found that increasing satellite foot print with good rain gauge network can improve the usage of rain gauge measurement to validate the satellite estimates. It was also found that recalibrating the rain /no rain in terms of Z and brightness temperature in H-E algorithm, reduces the over estimation of the non-convective rain rate.

Noteworthy, these conclusions are drawn based on analysis for limited number of days.

6.2. Recommendations

1) It is important to consider the inability of the CPP to retrieve the cloud properties in the morning and evening over Kenya. Retrieval on regional basis is recommended to reduce this problem.

2) Over Kenya it was found that the satellite estimates compared to rain gauge measurements as depicted by the line curves had shifts and this was considered due to parallax error by the satellites. This caused the point of detection of precipitating cloud to be different from the position of rainfall. It is therefore recommended to include weather analysis from the stations to determine this effect. Due poor to rain gauge distribution, the validation is recommended only on areas with dense rain gauges over this region.

3) The study indicates evaporation at the cloud base to be a major effect in rain gauge and satellite retrieval discrepancies as seen from their large differences and there is need for this correction.

4) It is also recommended to recalibrate the H-E rain /no rain separation in terms of Z and brightness temperature at regional basis to avoid over estimation of non-convective rain rate before application.

5) More events need to be analysed for this study

LIST OF REFERENCES

Adler, R. F., & Negri , A. J. (1988). A satellite IR technique to estimate tropical convective and stratiform rainfall. *J. Appl. Meteorol., 27*, 30– 51

AghaKouchak, A., Habib, E., & Bardossy, A. (2010). Modeling Radar Rainfall Estimation Uncertainties. *Journal of Hydrologic Engineering, 15(4)*, 265-274.

Ahrens, C. D. (2007). *Meteorology Today : An Introduction to Weather, Climate, and the Environment* (eighth edition ed.). Australia: Thomson.

Arkin, P. A. (1979). The relationship between fractional coverage of high cloud and rainfall accumulations during the GAGE over the B-scale array. *Mon. Weather Rev. , 107*, 1382–1387.

Arkin, P. A., & Meisner, B. N. (1987). The relationship between large -scale convective rainfall and cold cloud over the Western Hemisphere during 1982-84. *Mon.Wea.Rev., 115*, 51-74.

Barros, A. P., & Lettenmaier, D. P. (1993). Dynamic modeling of the spatial distribution of precipitation in remote mountainous area. *Mon. Wea. Rev., 121*, 1195-1214.

Barros, A. P., & Lettenmaier, D. P. (1994). Dynamic modeling of orographically induced precipitation. *Rev. geophys., 32*, 265-284.

Barrret, E. C., & Martin, D. W. (1981). The Use of Satellite data in Rainfall Monitoring. *Academic Press*, 340 pp.

Bellon, A., Lovejoy, S., & Austin, G. L. (1980). Combining satellite and radar data for the short-range forecasting of precipitation. *Mon.Wea.Rev., 108*, 1554-1556.

Bindlish, R., & Barros, A. P. (2000). Disaggregation of rainfall for one-way coupling of atmospheric and hydrologic models in regions of complex terrain. *Global Planet. Change, 25*, 111-132.

Brutsaert, W. (2005). *Hydrology. An Introduction*. Cambridge: Cambridge University Press.

Cheng, M., Brown, R., & Collier, C. G. (1993). Delineation of precipitation areas using METEOSAT infrared and visible data in the region of the United Kingdom. *J.Appl. Meteorol., 32*, 884-898.

COMET. (2000). Radar. Retrieved 13/02/2011, from http://www.everythingweather.com/weather-radar/principles.shtml

Corder, G. W., & Foreman, D. I. (2009). Nonparametric statistics for Non-Statisticians. Retrieved from http://en.wikipedia.org/wiki/Student%27s_t_distribution

Dingman, S. L. (1994). *Physical Hydrology*. Upper Saddle River: Prentice Hall.

El-Baz, F. (2008). Remote sensing of the earth: Implication for Ground water in Darfur,The Brigde. *38*(3), 5-14

FAO. (1997). World Climates. Retrieved 2010-10-26, from http://www.blueplanetbiomes.org/climate.htm

Goodrich, D. C., Faures, D. A., Wooolhiser, L. J., Lane, & Sorooshian, S. (1995). Measure ment and analysis of small -scale convective storm rainfall variability. *J.Hydrolology, 173*, 283-308.

Gray, D. M. (Ed.). (1973). *Handbook on the principles of hydrology : a general text with special emphasis directed to Canadian conditions in the discussions, applications and presentation of data*. Huntington: Water Information Center.

Griffith, C. G., Woodley, W. L., Grube, P. G., Martin, D. W., Stout, J., & Sikdar, D. N. (1978). Rain estimation from geosynchronous satellite imagery-visible and infrared studies. *Mon. Weather Rev., 106*, 1153–1171.

Grimes, D. I. F. (2008). Geostatistical Tools for Validation of Satellite and NWP Model Rainfall Estimates. In S. Sorooshian, K.-L. Hsu, E. Coppola, B. Tomassetti, M. Verdecchia & G. Visconti (Eds.), *Hydrological Modelling and the Water Cycle* (Vol. 63, pp. 117-143): Springer Berlin Heidelberg.

Heinemann, T., & Kerenyi, J. (2003). The EUMETSAT Multi sensor Precipitaion Estimate (MPE): Concept and Validation ,proceedings of the EUMETSAT users conference, Weimar, Germany.

Hu, Y. X., & Stamnes, K. (1993). An accurate parameterization of the radiative properties of water clouds suitable for use in climate models. *J. Climate, 6*, 70-83.

Huade, G., & John, l. W. (2005). Geostatistical Mapping of Precipitation Incorporating Autosearched Effects of Terrain and Climatic Characteristics. *Journal of hydrometeology, 6*, 1018.

Huffman, G. J., Adler, R. F., Arkin, P., Chang, A., Ferraro, R., Gruber, A., et al. (1997). The Global Precipitation Climatology Project (GPCP) combined precipitation data set. *Bull.Am.Meteorolo.Soc., 78*, 5-20.

Huffman, G. J., Adler, R. F., Morrissey, M., Bolvin, D. T., Gu, G., Nelkin, K. P., et al. (2007). The TRMM Multi-satellite Precipitation analysis (TMPA): Quasi-global, Multi -year, combined--sensor Precipitation at fine scales. *J.Hydrometeorol,, 8(1)*, 38-55.

Kidd, C., Kniveton, D., & Barrett, E. C. (1998). The advantages and disadvantages of statistically derived-empirically calibrated passive microwave algorithms for rainfall estimation *J. Atmos. Sci., 55*, 1576-1582.

.

Kitchen, M., & Jackson, P. M. (1993). Weather radar performance at long range-Simulated and observed. *J. Appl. Meteorol., 32*, 975–985.

Kleespies, T. J. (1995). The retrieval of marine stratiform cloud properties from multiple observations in the 3.9-µm window under conditions of varying solar illumination. *J. Appl.Meteorol.appl., 34*, 1512-1524.

Kuligowski, R. J., Davenport, J. C., & Scofield, R. A. (2003). The Hydro-Estimator technique for highest - resolution geostationary satellite rainfall estimates.Submitted to Mon.We.Rev.

Levizzani, V., Amorati, R., & Meneguzzo, F. (2002). A review of satellite-based rainfall estimation methods. European Commission Project MUSIC report (EVKI-CT-2000-00058., 66 pp.

Liou, K. N. (1992). Radiation and cloud processes in the atmosphere. *Oxford Univ. Press,* 487pp.

Maidment, D. R. (Ed.). (1993). *Handbook of hydrology* New York: MacGraw-Hill.

Marzban, C. (1998). Scalar Measures of Performance in Rare-event Situations, Weather and Forecasting *13*, 753-763.

McCollum, J. A., Gruber, A., & Ba, M. (2000). Comparison of monthly mean satellite estimates of precipitation with gauges over Africa. *J. Appl. Meteor., 39*, 666–679.

NCAR. (2010). CISL Research Data Archive Home
from http://nomad1.ncep.noaa.gov/cgi-bin/ftp2u_6p_r2.sh retrieved on 29/10/2010

Negri , A. J., Adler , R. F., & Wetzel , P. J. (1984). Satellite rain estimation: An analysis of the Griffith-Woodley technique. Journal of Climate and Applied Meteorology. *23*, 102-116.

Oki, T. K., Musiake, & Koike, T. (1991). Spatial rainfall distribution at a storm event in mountainous regions, estimated by orography and wind direction. Water Resour. Res.*, 27*, 359-369.

Prigent, C. (2010). Precipitation retrieval from space. Comptes Rendus Geoscience. *342(4-5)*, 380-389.

Roebeling, R. A., Feijt, A. J., & Stammes, P. (2006). Cloud property retrievals for climate monitoring: Implications of differences between SEVIRI on METEOSAT-8 and AVHRR on NOAA-17. *J. Geophys., Res,111*.

Roebeling, R. A., & Holleman, I. (2009). SEVIRI rainfall retrieval and validation using weather radar observations. *Journal of Geophysical Research-Atmospheres, 114*.

Rosenfield, D., & Gutman, G. (1994). Retrieving microphysical properties near the tops of potential rain clouds by multi spectral analysis of AVHRR data. *J.atmos., 34*, 259–283.

Saunders, R. W., & Kriebel, K. T. (1988). An improved method for detecting clear sky and cloudy radiances from AVHRR data. *J. Remote Sensing, 9*, 123-150.

Scofield, R. A., & Kuligowski, R. J. (2003). Status and outlook of Operational Satellite Precipitation algorithm for Extreme-Precipitation Events. *Mon. Wea. Rev., 18*, 1037-1051.

Silvio, S. Z., & Bryan, F. J. (2006). Generating different data sets for linear regression models with the same estimates. Retrieved 01/01/1011, from http://www.ime.usp.br/~abe/ICOTS7/Proceedings/PDFs/ContributedPapers/C108.pdf

Slingo, A., & Schrecker, H. M. (1982). On the shortwave radiative properties of stratiform water clouds. *Q. J. R. Meteorol. Soc., 108*, 407-426.

Sorooshian, S., Hsu, K.-L., Gao, X., Gupta, H. V., Imam, B., & Braithwaite, D. (2000). Evaluation of PERSIANN system satellite–based estimates of tropical rainfall. *Bull. Am. Meteor. Soc., 81*, 2035–2046.

Sotillo, M. G., Ramis, C., Romero, R., Alonso, S., & Homar, V. (2003). Role of orography in the spatial distribution of precipitation over the Spanish Mediterranean zone. Climate Res. *23*, 247–261.

STAR. STAR Satellite Rainfall Estimates - Hydro-Estimator. Retrieved 06/11/2010, from http://www.star.nesdis.noaa.gov/smcd/emb/ff/HEtechnique.php

Stephens, G. L., Paltridge, G. W., & Platt , C. M. R. (1978). Radiation Profiles in Extended Water Clouds. III: Observations. *J. Atmos. Sci., 35*, 2133– 2141.

Sturman, A., & Wanner, H. (2001). A Comparative Review of the Weather and Climate of the Southern Alps of New Zealand and the European Alps. Mountain Research and Development. *21*, 359–369.

Todd, M. C., Barrett, E. C., Beaumont, M. J., & Bellerby, T. J. (1999). Estimation of daily rainfall over the upper Nile river basin using a continuously calibrated satellite infrared technique. *Meteorological Applications, 6*, 201-210.

Vicente, G. A., Scofield, R. A., & Menzel, W. P. (1998). The operational GOES infrared rainfall estimation technique. *American Meteorological Society,, 79(9)*, 1883-1898.

Wentz, F. J., & Spencer, R. W. (1998). SSM/I Rain retrievals within a unified all-weather ocean algorithm. *J.Atmos.Sci., 55*, 1613-1627.

Young, C. B., Nelson, B. R., Bradley, A. A., Smith, J. A., Peters-Lidard, C. D., Kruger, A., et al. (1999). An evaluation of NEXRAD precipitation estimates in complex terrain. *J. Geophys. Res., 104*, 19691–19703.

LIST OF APPENDICES

Appendix 1: Model data download

//The model data from NOAA forecast applied in Eta model of Hydro Estimator was found in the NOAA model data website: http://nomad1.ncep.noaa.gov/ncep_data/index.html

// http://nomad1.ncep.noaa.gov:9090/dods/reanalyses/reanalysis-2/6hr/pgb/ pgb.info webpage gives the data spatial and temporal resolution which is $2.5^0 \times 2.5^0$ (latitude and longitude) and 6 hours temporal resolution.

//From CDAS-NCEP/NCAR Reanalysis selection of Reanalysis -2 pressure levels 4x daily was done, then ftp2u ftp. Webpage was opened.

//The pgb.ft00.yyyymm data was then selected according to the year, month wanted. For this study the year 2010, month of July for NW window was chosen and the month of April same year for Kenya window.

// Selection of the variables and level was done. PW (precipitable water) and RH (relative humidity at 500mb level) at global scale was used.

//selection was done on corresponding days and hours. Two days from each region were selected .For northwest Europe 3rd and 12th day of July and Kenya 2rd and 3rd day of April. The hours selected were 00, 06, 12 and 18 UTC for PW and RH separately for respective days and the data was sent to ftp site where it was downloaded into external drive.

Appendix 2: Model data importation into ILWIS format

The data was imported into ILWIS format by use of 2 scripts.

Geospatial Data Abstraction Library (GDAL) information

D:\ilwis371_52n\Extensions\Geonetcast-Toolbox\GDAL\bin\gdalinfo input map (this is grib input file). The input file refers to PW or RH at 00, 06, 12 or 18 UTC time.

GDAL_translate

D:\ilwis371_52n\Extensions\Geonetcast-Toolbox\GDAL\bin\gdal_translate -of Ilwis input map outputmap.mpr .The output file refers to the new import file name.

The data was assigned georeference corners (90N/S and 180W/E) for each variable; PW and RH.

The PW and RH was averaged (00, 06, 12, 18 UTC) to get the daily average map by use of map list function in ILWIS.

The Eta model curves (Figure 13 and 14 were converted into polygon functions to enable spatial variations of temperature rain rate and relative humidity relative to precipitable water (PW)

The study areas polygon maps were extracted from the GSOD world rain gauge polygon maps.

H-E rain rate estimate Processing

Use was made of ILWIS scripts to run algorithm processes.

Appendix 3: One –time script (preparation script)

This script was used to resample the model data (PW and RH) and recomputed spatial maps of the polynomial functions derived from model (Eta) adjusted brightness temperature, rain rate at 210 K and rainfall reduction with respect to RH. The output maps were resampled into geostationary georeference. The study area polygon maps of Belgium-Netherlands and Kenya were also rasterized by use of this script. The example given here is for Belgium-Netherlands map.

PW and RH Averages resampled

PWavere: =MapResample (PWave.mpr, c07300000.grf, Nearest Neighbour)
RHavere: =MapResample (RHave.mpr, c07300000.grf, Nearest Neighbour)

10.8µm brightness temperature adjusted polynomial curve conversion into map. See appendix 21

Tbcorr: =2.3995694+-0.065047931*PWavere+-0.00407337*(PWavere) ^2+0.00017242466*(PWavere) ^3+-1.7490547e-006*(PWavere) ^4

Rain rate Adjustment at 210K polynomial curve conversion into map. See appendix 21

rain210_PW:=19.001015+0.70664924*PWavere+-0.030283779*(PWavere) ^2+0.0005454345*(PWavere) ^3+-3.2176021e-006*(PWavere) ^4

Rain rate adjusted for relative humidity polynomial curve conversion into map. See appendix 21

rain_reduc:=62.049427-52.945023*RHavere*0.01-382.87221*(RHavere*0.01) ^2+782.46126*(RHavere*0.01) ^3-425.44012*(RHavere*0.01) ^4

Northwest Europe map masking

belguim_netherlands:=MapRasterizePolygon (belguim_netherlands.mpa, c07300000.grf)

Appendix 4: Script 3 (H-E algorithm processing)

Script 3 processes one file of the map list (from time 0730 UTC to 1530 UTC) and then MS-Dos batch files were used to run the process for all the maplists

```
Tbadj_%1:=%1+Tbcorr
Rc_%1:=1.1183*10^11*exp (-0.036382*Tbadj_%1^1.2)
Rc240_%1:=iff (Tbadj_%1=240, 0.5, Rc_%1)
Rc210_%1:=iff (Tbadj_%1=210, rain210_PW, Rc240_%1)
RcRh_%1:=Rc210_%1-rain_reduc
RcRhneg_%1:=iff (RcRh_%1<0, 0, RcRh_%1)
Rcmax: =PWavere*40/25.4
RcRhnegmax_%1:=iff (RcRhneg_%1>Rcmax, Rcmax, RcRhneg_%1)
Rs_%1 :=( 250-Tbadj_%1)*Rcmax*0.2
RsRh_%1:=Rs_%1-rain_reduc
RsRhneg_%1:=iff (RsRh_%1<0, 0, RsRh_%1)
RsRhnegmax_%1:=iff(RsRhneg_%1>=Rcmax*0.2,Rcmax*0.2*RsRhneg_%1/333,RsRhneg_%1)
RsRhnegmaxc_%1:=iff (Tbadj_%1>243, 0, RsRhnegmax_%1)
Tbave_%1:=MapAggregateavg (%1.mpr, 3, No Group)
Tbstd_%1:=MapAggregatemin (%1.mpr, 3, No Group)
Z_%1:=(Tbave_%1-Tbadj_%1)/Tbstd_%1
Zcore_%1:=iff (Z_%1<0, 0, Z_%1)
Z2_%1:=iff (Zcore_%1<=1.5, Zcore_%1,0)
RR_%1:=(RcRhnegmax_%1*Z2_%1^2+RsRhnegmaxc_%1*(1.5-Z2_%1)^2)/(Z2_%1^2+(1.5-
Z2_%1)^2)
RRmask_%1:=iff (ISUNDEF (belguim_netherlands),?,1)
RRmaskc_%1:=iff (RRmask_%1=1, RR_%1,0)
RRmaskcc_%1:=iff (ISUNDEF (RRmaskc_%1), 0, RRmaskc_%1)
Rsmaskc_%1:=iff (RRmask_%1=1, RsRhnegmaxc_%1,0)
Rsmaskcc_%1:=iff (ISUNDEF (Rsmaskc_%1), 0, Rsmaskc_%1)
Rcmaskc_%1:=iff (RRmask_%1=1, RcRhnegmax_%1,0)
```

Rcmaskcc_%1:=iff (ISUNDEF (Rcmaskc_%1), 0, Rcmaskc_%1)
Zmaskc_%1:=iff (RRmask_%1=1, Z2_%1,0)
Zmaskcc_%1:=iff (ISUNDEF (Zmaskc_%1), 0, Zmaskc_%1)

Callscript3.bat:

Callscript.bat process one file of the map list but the actual work is done by script3; this file simply removes the extension of the maps file name, and then calls script 3.

(@echo off
set filename=%1
d:\ilwis_371\ilwis.exe -C run script3 %filename: ~0, 9%)

Runall3.bat:

@echo off
for %%j in (c*.mpr) do callscript3.bat %%j

This script processes all the files of the map list (In reality this file process all files that start with letter "e","f","c"and "d"(used for different days) and end with .mpr.) for each file ,callscript.bat is called.

Appendix 5: Script 4 (map list computation)

Scripts 4 create the map list and sum them to give the day total rain rate for the H-E algorithm.

crmaplist RRmaskccc RRmaskccc_c07300000.mpr RRmaskccc_c07450000.mpr
RRmaskccc_c08000000.mpr RRmaskccc_c08150000.mpr RRmaskccc_c08300000.mpr
RRmaskccc_c08450000.mpr RRmaskccc_c09000000.mpr RRmaskccc_c09150000.mpr
RRmaskccc_c09300000.mpr RRmaskccc_c09450000.mpr RRmaskccc_c10000000.mpr
RRmaskccc_c10150000.mpr RRmaskccc_c10300000.mpr RRmaskccc_c10450000.mpr
RRmaskccc_c11000000.mpr RRmaskccc_c11150000.mpr RRmaskccc_c11300000.mpr
RRmaskccc_c10450000.mpr RRmaskccc_c11000000.mpr RRmaskccc_c11150000.mpr
RRmaskccc_c11300000.mpr RRmaskccc_c11450000.mpr RRmaskccc_c12000000.mpr
RRmaskccc_c12150000.mpr RRmaskccc_c12300000.mpr RRmaskccc_c12450000.mpr
RRmaskccc_c13000000.mpr RRmaskccc_c13150000.mpr RRmaskccc_c13300000.mpr
RRmaskccc_c13450000.mpr RRmaskccc_c14000000.mpr RRmaskccc_c14150000.mpr
RRmaskccc_c14300000.mpr RRmaskccc_c14450000.mpr RRmaskccc_c15000000.mpr
RRmaskccc_c15150000.mpr RRmaskccc_c15300000.mpr
RRmasksum:=MapMaplistStatistics(RRmaskccc.mpl, Sum, 0, 32)

Appendix 6: Script 4b

Script 7 calculates the sum of the intermediate maps (convective (Rc) and non convective (Rs) aggregated day rainfall maps in the H-E algorithm.

Rcmaskccsum:=MapMaplistStatistics(Rcmaskcc_out.mpl, Sum, 0, 32)
RRmasksum:=MapMaplistStatistics(RRmaskcc_out.mpl, Sum, 0, 32)
Rsmaskccsum:=MapMaplistStatistics(Rsmaskcc_out.mpl, Sum, 0, 32)
Zmaskccsum: =MapMaplistStatistics (Zmaskcc_out.mpl, Sum, 0, 32)
Tbadjmin: =MapMaplistStatistics (Tbadj_out.mpl, min, 0, and 32)

Appendix 7: CPP field data Import

The field data from KNMI in Hdf format were imported into ILWIS format.

CPP LUTs fields were imported from hdf5 files into ILWIS raster maps by use of MS- DOS's scripts (batch files).

Geospatial Data Abstraction Library (GDAL) information

This script simply reads the GDAL data
"D:\ilwis_371\Extensions\GeonetcastToolbox\GDAL\bin\gdalinfo"meteosat9_20100402_0730_00000.fl.PP-VNIR .hdf
NB "fl" was used for Kenya region, for Europe region "eu" was used and corresponding data and time.

GDAL_translate

This script translates GDAL data from Hdf into ILWIS format
"D:\ilwis_371\Extensions\Geonetcast-Toolbox\GDAL\bin\gdal_translate" –of ILWIS hdf5:"meteosat9_20100402_0730_00000.fl.PP-VNIR .hdf"://COT COT_0730
The field shown here is cloud optical thickness (COT), all other fields were likewise imported.
The raster maps of all fields were given georeference of the data (Test) which was derived by use of submap from the whole disc MSG georeference by downloading an ILWIS image of the whole disc

Appendix 8: Script 5 (PP-VNIR algorithm processing)

This script was used to run the PP-VNIR algorithm processes.
The script processes one file of the map list (from time 0730 UTC to 1530 UTC) and then
MS-Dos batch files were used to run the process for all the maplists.

```
cotre_%1:=MapResample (cot_%1.mpr, c07300000.grf, Nearest Neighbour)
reffre_%1:=MapResample (reff_%1.mpr, c07300000.grf, Nearest Neighbour)
cphre_%1:=MapResample (cph_%1.mpr, c07300000.grf, Nearest Neighbour)
cchre_%1:=MapResample (cch_%1.mpr, c07300000.grf, Nearest Neighbour)
cwp_%1:=2*cotre_%1*0.01*reffre_%1*0.01/3
PP-VNIR _%1:=iff(cphre_%1=1,1,0)*iff(cwp_%1>160,1,0)*iff(reffre_%1*0.01>15,1,0)*(((cwp_%1-120)/120)^1.6)/(cchre_%1*0.001)+iff(cphre_%1=2,1,0)*iff(cwp_%1>160,1,0)*(((cwp_%1-120)/120)^1.6)/(cchre_%1*0.001)
PP-VNIR max_%1:=iff(PP-VNIR _%1>40,40,PP-VNIR _%1)
PP-VNIR maxmask_%1:=ifundef (belguim_netherlands,?, PP-VNIR max_%1)
cotremask_%1:=ifundef (belguim_netherlands,?, cotre_%1)
reffremask_%1:=ifundef (belguim_netherlands,?, reffre_%1)
cphremask_%1:=ifundef (belguim_netherlands,?, cphre_%1)
cchremask_%1:=ifundef (belguim_netherlands,?, cchre_%1)
cwpmask_%1:=ifundef (belguim_netherlands,?, cwp_%1)
PP-VNIR maxmaskc_%1:=ifundef (PP-VNIR maxmask_%1, 0, PP-VNIR maxmask_%1)
cotremaskc_%1:=ifundef (cotremask_%1, 0, cotremask_%1)
reffremaskc_%1:=ifundef (reffremask_%1, 0, reffremask_%1)
cphremaskc_%1:=ifundef (cphremask_%1, 0, cphremask_%1)
cchremaskc_%1:=ifundef (cchremask_%1, 0, cchremask_%1)
cwpmaskc_%1:=ifundef (cwpmask_%1, 0, cwpmask_%1)
```

Callscript5.bat

```
@echo off
set filename=%1
d:\ilwis_371\ilwis.exe -C run script5 %filename:~4,4%
```

This script was used in this procedure to process one file of the map list (but the work was done by script 5, and this file simply removed the extension of the maps file name, then calls script5).

Runall5.bat

@echo off
For %%j in (cot_*.mpr) do callscript5.bat %%j

This script processed all the files of the map list (In reality this file processed all files (cot_*.mpr.). Then callscript5.bat is called.

Appendix 9: Script 9 (Ice and water phase maps computation)

This script was used to derive the ice and water phase maps from the imported original phase maps (CPH).The script processes one file of the map list (from time 0730 UTC to 1530 UTC) and then
MS-Dos batch files were used to run the process for all the maplists.
cphW_%1:=iff (cphremaskc_%1=1, cphremaskc_%1,0)
cphICE_%1:=iff (cphremaskc_%1=2, cphremaskc_%1,0)

Callscript9.bat

Callscript9.bat process one file of the map list but the actual work is done by script9; this file simply removes the extension of the maps file name, and then calls script 9.
@echo off
set filename=%1
d:\ilwis_371\ilwis.exe -C run script9Phase %filename: ~4, 4%

Runall9.bat

This script processed all the files of the map list (In reality this file processed all files (cot_*.mpr.). Then callscript9.bat is called.
@echo off
For %%j in (cot_*.mpr) do callscript9.bat %%j

Appendix 10: Script 6 (map list computation)

This script computed all the map lists of PP-VNIR cloud properties and the PP-VNIR rain rate.
crmaplist PP-VNIR MaxMaskc_out PP-VNIR maxmaskc_0730.mpr PP-VNIR maxmaskc_0745.mpr PP-VNIR maxmaskc_0800.mpr PP-VNIR maxmaskc_0815.mpr PP-VNIR maxmaskc_0830.mpr PP-VNIR maxmaskc_0845.mpr PP-VNIR maxmaskc_0900.mpr PP-VNIR maxmaskc_0915.mpr PP-VNIR maxmaskc_0930.mpr PP-VNIR maxmaskc_0945.mpr PP-VNIR maxmaskc_1000.mpr PP-VNIR maxmaskc_1015.mpr PP-VNIR maxmaskc_1030.mpr PP-VNIR maxmaskc_1045.mpr PP-VNIR maxmaskc_1100.mpr PP-VNIR maxmaskc_1115.mpr PP-VNIR maxmaskc_1130.mpr PP-VNIR maxmaskc_1145.mpr PP-VNIR maxmaskc_1200.mpr PP-VNIR maxmaskc_1215.mpr PP-VNIR maxmaskc_1230.mpr PP-VNIR maxmaskc_1245.mpr PP-VNIR maxmaskc_1300.mpr PP-VNIR maxmaskc_1315.mpr PP-VNIR maxmaskc_1330.mpr PP-VNIR maxmaskc_1345.mpr PP-VNIR maxmaskc_1400.mpr PP-VNIR maxmaskc_1415.mpr PP-VNIR maxmaskc_1430.mpr PP-VNIR maxmaskc_1445.mpr PP-VNIR maxmaskc_1500.mpr PP-VNIR maxmaskc_1515.mpr PP-VNIR maxmaskc_1530.mpr

crmaplist cotremaskc_out cotremaskc_0730.mpr cotremaskc_0745.mpr cotremaskc_0800.mpr cotremaskc_0815.mpr cotremaskc_0830.mpr cotremaskc_0845.mpr cotremaskc_0900.mpr cotremaskc_0915.mpr cotremaskc_0930.mpr cotremaskc_0945.mpr cotremaskc_1000.mpr cotremaskc_1015.mpr cotremaskc_1030.mpr cotremaskc_1045.mpr cotremaskc_1100.mpr cotremaskc_1115.mpr cotremaskc_1130.mpr cotremaskc_1145.mpr cotremaskc_1200.mpr cotremaskc_1215.mpr cotremaskc_1230.mpr cotremaskc_1245.mpr cotremaskc_1300.mpr cotremaskc_1315.mpr cotremaskc_1330.mpr cotremaskc_1345.mpr cotremaskc_1400.mpr

cotremaskc_1415.mpr cotremaskc_1430.mpr cotremaskc_1445.mpr cotremaskc_1500.mpr cotremaskc_1515.mpr cotremaskc_1530.mpr
crmaplist reffremaskc_out reffremaskc_0730.mpr reffremaskc_0745.mpr reffremaskc_0800.mpr reffremaskc_0815.mpr reffremaskc_0830.mpr reffremaskc_0845.mpr reffremaskc_0900.mpr reffremaskc_0915.mpr reffremaskc_0930.mpr reffremaskc_0945.mpr reffremaskc_1000.mpr reffremaskc_1015.mpr reffremaskc_1030.mpr reffremaskc_1045.mpr reffremaskc_1100.mpr reffremaskc_1115.mpr reffremaskc_1130.mpr reffremaskc_1145.mpr reffremaskc_1200.mpr reffremaskc_1215.mpr reffremaskc_1230.mpr reffremaskc_1245.mpr reffremaskc_1300.mpr reffremaskc_1315.mpr reffremaskc_1330.mpr reffremaskc_1345.mpr reffremaskc_1400.mpr reffremaskc_1415.mpr reffremaskc_1430.mpr reffremaskc_1445.mpr reffremaskc_1500.mpr reffremaskc_1515.mpr reffremaskc_1530.mpr
crmaplist cphremaskc_out cphremaskc_0730.mpr cphremaskc_0745.mpr cphremaskc_0800.mpr cphremaskc_0815.mpr cphremaskc_0830.mpr cphremaskc_0845.mpr cphremaskc_0900.mpr cphremaskc_0915.mpr cphremaskc_0930.mpr cphremaskc_0945.mpr cphremaskc_1000.mpr cphremaskc_1015.mpr cphremaskc_1030.mpr cphremaskc_1045.mpr cphremaskc_1100.mpr cphremaskc_1115.mpr cphremaskc_1130.mpr cphremaskc_1145.mpr cphremaskc_1200.mpr cphremaskc_1215.mpr cphremaskc_1230.mpr cphremaskc_1245.mpr cphremaskc_1300.mpr cphremaskc_1315.mpr cphremaskc_1330.mpr cphremaskc_1345.mpr cphremaskc_1400.mpr cphremaskc_1415.mpr cphremaskc_1430.mpr cphremaskc_1445.mpr cphremaskc_1500.mpr cphremaskc_1515.mpr cphremaskc_1530.mpr
crmaplist cchremaskc_out cchremaskc_0730.mpr cchremaskc_0745.mpr cchremaskc_0800.mpr cchremaskc_0815.mpr cchremaskc_0830.mpr cchremaskc_0845.mpr cchremaskc_0900.mpr cchremaskc_0915.mpr cchremaskc_0930.mpr cchremaskc_0945.mpr cchremaskc_1000.mpr cchremaskc_1015.mpr cchremaskc_1030.mpr cchremaskc_1045.mpr cchremaskc_1100.mpr cchremaskc_1115.mpr cchremaskc_1130.mpr cchremaskc_1145.mpr cchremaskc_1200.mpr cchremaskc_1215.mpr cchremaskc_1230.mpr cchremaskc_1245.mpr cchremaskc_1300.mpr cchremaskc_1315.mpr cchremaskc_1330.mpr cchremaskc_1345.mpr cchremaskc_1400.mpr cchremaskc_1415.mpr cchremaskc_1430.mpr cchremaskc_1445.mpr cchremaskc_1500.mpr cchremaskc_1515.mpr cchremaskc_1530.mpr
crmaplist cphICE_out cphICE_0730.mpr cphICE_0745.mpr cphICE_0800.mpr cphICE_0815.mpr cphICE_0830.mpr cphICE_0845.mpr cphICE_0900.mpr cphICE_0915.mpr cphICE_0930.mpr cphICE_0945.mpr cphICE_1000.mpr cphICE_1015.mpr cphICE_1030.mpr cphICE_1045.mpr cphICE_1100.mpr cphICE_1115.mpr cphICE_1130.mpr cphICE_1145.mpr cphICE_1200.mpr cphICE_1215.mpr cphICE_1230.mpr cphICE_1245.mpr cphICE_1300.mpr cphICE_1315.mpr cphICE_1330.mpr cphICE_1345.mpr cphICE_1400.mpr cphICE_1415.mpr cphICE_1430.mpr cphICE_1445.mpr cphICE_1500.mpr cphICE_1515.mpr cphICE_1530.mpr
crmaplist cphW_out cphW_0730.mpr cphW_0745.mpr cphW_0800.mpr cphW_0815.mpr cphW_0830.mpr cphW_0845.mpr cphW_0900.mpr cphW_0915.mpr cphW_0930.mpr cphW_0945.mpr cphW_1000.mpr cphW_1015.mpr cphW_1030.mpr cphW_1045.mpr cphW_1100.mpr cphW_1115.mpr cphW_1130.mpr cphW_1145.mpr cphW_1200.mpr cphW_1215.mpr cphW_1230.mpr cphW_1245.mpr cphW_1300.mpr cphW_1315.mpr cphW_1330.mpr cphW_1345.mpr cphW_1400.mpr cphW_1415.mpr cphW_1430.mpr cphW_1445.mpr cphW_1500.mpr cphW_1515.mpr cphW_1530.mpr
crmaplist cwpmaskc_out cwpmaskc_0730.mpr cwpmaskc_0745.mpr cwpmaskc_0800.mpr cwpmaskc_0815.mpr cwpmaskc_0830.mpr cwpmaskc_0845.mpr cwpmaskc_0900.mpr cwpmaskc_0915.mpr cwpmaskc_0930.mpr cwpmaskc_0945.mpr cwpmaskc_1000.mpr cwpmaskc_1015.mpr cwpmaskc_1030.mpr cwpmaskc_1045.mpr cwpmaskc_1100.mpr cwpmaskc_1115.mpr cwpmaskc_1130.mpr cwpmaskc_1145.mpr cwpmaskc_1200.mpr cwpmaskc_1215.mpr cwpmaskc_1230.mpr cwpmaskc_1245.mpr cwpmaskc_1300.mpr

cwpmaskc_1315.mpr cwpmaskc_1330.mpr cwpmaskc_1345.mpr cwpmaskc_1400.mpr
cwpmaskc_1415.mpr cwpmaskc_1430.mpr cwpmaskc_1445.mpr cwpmaskc_1500.mpr
cwpmaskc_1515.mpr cwpmaskc_1530.mpr

Appendix 11: Script 7 (sum averages and aggregation computation)

This scripts creates all the cloud properties averages and sum for PP-VNIR rain rate
It aggregated the day total rain rate of PP-VNIR and H-E into a 5 pixel box to increase the foot print of the satellite .This was done to reduce uncertainties of satellite versus rain gauge different spatial variations.

PP-VNIR sum.mpr:=mapmaplistatistics (PP-VNIR maxmaskc_out.mpl, Sum, 0, 32)
cotAvg.mpr:=MapmaplistStatistics (cotremaskc_out.mpl, Avg, 0, 32)
reffAvg.mpr:=MapmaplistStatistics (reffremaskc_out.mpl, Avg, 0, 32)
cphAvg.mpr:=MapmaplistStatistics (cphremaskc_out.mpl, Avg, 0, 32)
cchAvg.mpr:=MapmaplistStatistics (cchremaskc_out.mpl, Avg, 0, 32)
cwpAvg.mpr:=MapmaplistStatistics (cwpmaskc_out.mpl, Avg, 0, 32)
cphICEAvg.mpr:=MapmaplistStatistics (cphICE_out.mpl, Avg, 0, 32)
cphWAvg.mpr:=MapmaplistStatistics (cphW_out.mpl, Avg, 0, 32)
cwpAvg.mpr:=MapmaplistStatistics (cwpmaskc_out.mpl, Avg, 0, 32)
PP-VNIR sumc: =MapAggregateavg (PP-VNIR sum.mpr, 5, No Group)
RRmasksumc: =MapAggregateavg (RRmasksum.mpr, 5, No Group)

Appendix 12: Script 8 (attribute tables computation for statistical analysis)

This script was used to ”cross” each PP-VNIR cloud properties with PP-VNIR rain rate maps and between the PP-VNIR rain rate with H-E rain rate after every 15 minutes .The tables were used to derive hourly rainfall of each algorithm and 15 minutes variation of cloud properties. For effective radius “reff”” was used in place of “r_e”.
r%1.tbt:= TableCross (PP-VNIR maxmaskc_%1, RRmaskcc_c%10000, IgnoreUndefs)
r_cch%1.tbt:= TableCross (PP-VNIR maxmaskc_%1, cchremaskc_%1, IgnoreUndefs)
r_reff%1.tbt:= TableCross (PP-VNIR maxmaskc_%1, reffremaskc_%1, IgnoreUndefs)
r_cot%1.tbt:= TableCross (PP-VNIR maxmaskc_%1, cotremaskc_%1, IgnoreUndefs)
r_cwp%1.tbt:= TableCross (PP-VNIR maxmaskc_%1, cwpmaskc_%1, IgnoreUndefs)
To enable repeated action for allthe maplists, two batch files were used. The work was done by script 8 but callscript8 and runall_script call callscript.

Callscript8.bat

Callscript8. Bat process one file of the map list but the actual work is done by script8, this file simply removes the extension of the maps file name, and then calls script 8.

```
@echo off
Set filename=%1
d:\ilwis_371\ilwis.exe -C run script8_PP-VNIR _H-E %filename: ~4, 4%
```

runall_script8.bat

This script processed all the files of the map list (In reality this file processed all files (cot_*.mpr.). Then callscript8.bat is called.

```
@echo off
for %%j in (c*.mpr) do callscript3.bat %%j
```

Appendix 13: Script 10

This script reduced the decimal places to 1 by assigning zeros to numbers beyond i decimal place.

Appendix 14: Student's t-test tabulated values

One Sided	75%	80%	85%	90%	95%	97.50%	99%	99.50%	99.75%	99.90%	99.95%
Two Sided	50%	60%	70%	80%	90%	95%	98%	99%	99.50%	99.80%	99.90%
1	1	1.376	1.963	3.078	6.314	12.71	31.82	63.66	127.3	318.3	636.6
2	0.816	1.061	1.386	1.886	2.92	4.303	6.965	9.925	14.09	22.33	31.6
3	0.765	0.978	1.25	1.638	2.353	3.182	4.541	5.841	7.453	10.21	12.92
4	0.741	0.941	1.19	1.533	2.132	2.776	3.747	4.604	5.598	7.173	8.61
5	0.727	0.92	1.156	1.476	2.015	2.571	3.365	4.032	4.773	5.893	6.869
6	0.718	0.906	1.134	1.44	1.943	2.447	3.143	3.707	4.317	5.208	5.959
7	0.711	0.896	1.119	1.415	1.895	2.365	2.998	3.499	4.029	4.785	5.408
8	0.706	0.889	1.108	1.397	1.86	2.306	2.896	3.355	3.833	4.501	5.041
9	0.703	0.883	1.1	1.383	1.833	2.262	2.821	3.25	3.69	4.297	4.781
10	0.7	0.879	1.093	1.372	1.812	2.228	2.764	3.169	3.581	4.144	4.587
11	0.697	0.876	1.088	1.363	1.796	2.201	2.718	3.106	3.497	4.025	4.437
12	0.695	0.873	1.083	1.356	1.782	2.179	2.681	3.055	3.428	3.93	4.318
13	0.694	0.87	1.079	1.35	1.771	2.16	2.65	3.012	3.372	3.852	4.221
14	0.692	0.868	1.076	1.345	1.761	2.145	2.624	2.977	3.326	3.787	4.14
15	0.691	0.866	1.074	1.341	1.753	2.131	2.602	2.947	3.286	3.733	4.073
16	0.69	0.865	1.071	1.337	1.746	2.12	2.583	2.921	3.252	3.686	4.015
17	0.689	0.863	1.069	1.333	1.74	2.11	2.567	2.898	3.222	3.646	3.965
18	0.688	0.862	1.067	1.33	1.734	2.101	2.552	2.878	3.197	3.61	3.922
19	0.688	0.861	1.066	1.328	1.729	2.093	2.539	2.861	3.174	3.579	3.883
20	0.687	0.86	1.064	1.325	1.725	2.086	2.528	2.845	3.153	3.552	3.85
21	0.686	0.859	1.063	1.323	1.721	2.08	2.518	2.831	3.135	3.527	3.819
22	0.686	0.858	1.061	1.321	1.717	2.074	2.508	2.819	3.119	3.505	3.792
23	0.685	0.858	1.06	1.319	1.714	2.069	2.5	2.807	3.104	3.485	3.767
24	0.685	0.857	1.059	1.318	1.711	2.064	2.492	2.797	3.091	3.467	3.745
25	0.684	0.856	1.058	1.316	1.708	2.06	2.485	2.787	3.078	3.45	3.725
26	0.684	0.856	1.058	1.315	1.706	2.056	2.479	2.779	3.067	3.435	3.707
27	0.684	0.855	1.057	1.314	1.703	2.052	2.473	2.771	3.057	3.421	3.69
28	0.683	0.855	1.056	1.313	1.701	2.048	2.467	2.763	3.047	3.408	3.674
29	0.683	0.854	1.055	1.311	1.699	2.045	2.462	2.756	3.038	3.396	3.659
30	0.683	0.854	1.055	1.31	1.697	2.042	2.457	2.75	3.03	3.385	3.646
40	0.681	0.851	1.05	1.303	1.684	2.021	2.423	2.704	2.971	3.307	3.551
50	0.679	0.849	1.047	1.299	1.676	2.009	2.403	2.678	2.937	3.261	3.496
60	0.679	0.848	1.045	1.296	1.671	2	2.39	2.66	2.915	3.232	3.46
80	0.678	0.846	1.043	1.292	1.664	1.99	2.374	2.639	2.887	3.195	3.416
100	0.677	0.845	1.042	1.29	1.66	1.984	2.364	2.626	2.871	3.174	3.39
120	0.677	0.845	1.041	1.289	1.658	1.98	2.358	2.617	2.86	3.16	3.373
∞	0.674	0.842	1.036	1.282	1.645	1.96	2.326	2.576	2.807	3.09	3.291

Appendix 15a: Rain gauge distribution over NW Europe region

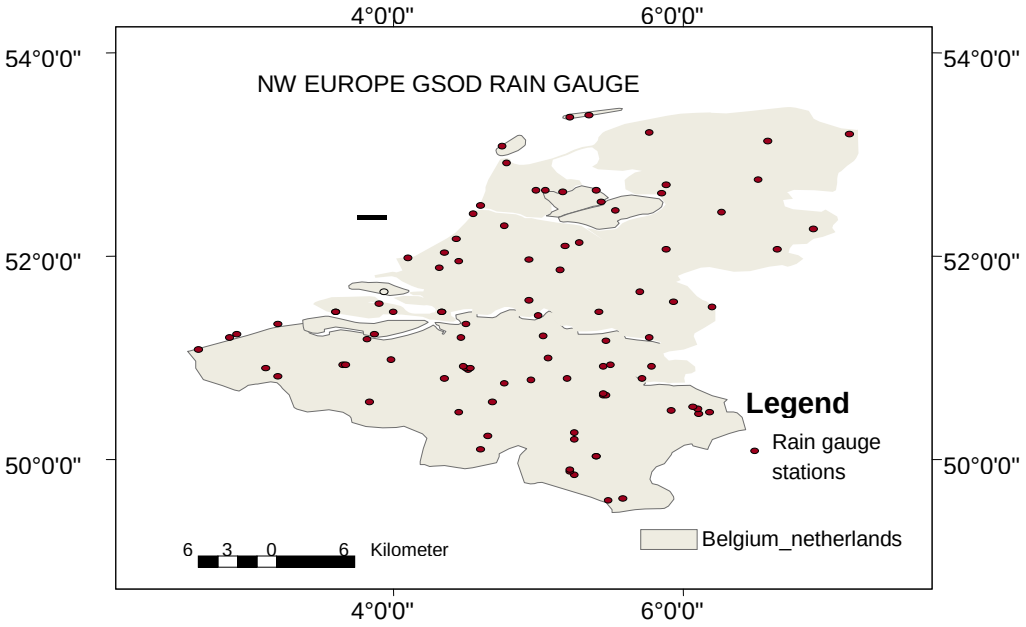

Appendix 15b: Rain gauge distribution over Kenya region

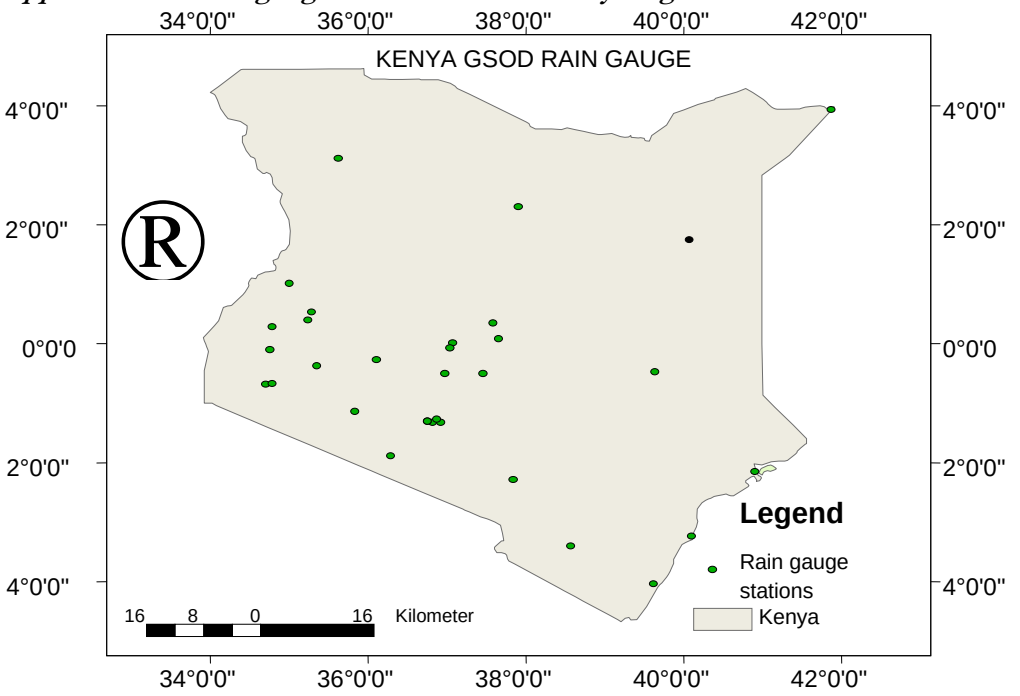

Appendix 16: NW Europe Rain gauge Stations 3rd July

GSOD stations	USAF	Lat_new	Lon_new	Observed	PP-VNIR	H-E	Observed	PP-VNIR	H-E
st2580	64000	51.083	2.65	0.508	2.5	5.1	Rain	Rain	Rain
st2584	64070	51.2	2.867	3.302	7.1	12.2	Rain	Rain	Rain
st 2585	64280	50.933	3.667	9.144	19.6	11.1	Rain	Rain	Rain
st2582	64310	51.183	3.817	7.112	12.3	11.8	Rain	Rain	Rain
st2564	64320	50.567	3.833	7.874	32.2	1.2	Rain	Rain	Rain
st2571	64470	51.2	2.867	5.842	25.9	0.6	Rain	Rain	Rain
st2560	64490	50.467	4.45	0	23.2	4.2	No rain	Rain	Rain
st2583	64500	51.2	4.467	0	23.7	0.3	No rain	Rain	Rain
st2573	64510	50.9	4.533	0	18.0	1.8	No rain	Rain	Rain
st2557	64560	50.233	4.65	0	0.6	6.4	No rain	Rain	Rain
st2567	64780	50.65	5.45	0	10.3	37.3	No rain	Rain	Rain
st2581	64790	51.167	5.467	0	3.1	31.6	No rain	Rain	Rain
st2562	64900	50.483	5.917	0	10.0	41.9	No rain	Rain	Rain
st2559	64960	50.467	6.183	16.002	2.3	44.2	Rain	Rain	Rain
st12127	62400	52.3	4.767	1.016	36.3	0.7	Rain	Rain	Rain
st12120	62600	52.1	5.183	0	24.3	4.3	No rain	Rain	Rain
st12155	62700	53.217	5.767	0	6.3	6.0	No rain	Rain	Rain
st12142	62730	52.7	5.883	0	3.9	11.7	No rain	Rain	Rain
st12119	62750	52.067	5.883	0	0.7	26.1	No rain	Rain	Rain
st12131	62780	52.433	6.267	0	6.1	23.5	No rain	Rain	Rain
st12144	62790	52.75	6.517	0	7.5	16.6	No rain	Rain	Rain
st12152	62800	53.133	6.583	0	0.8	3.6	No rain	Rain	Rain
st12118	62830	52.067	6.65	0	11.0	26.7	No rain	Rain	Rain
st2124	62900	52.267	6.9	0	5.9	13.6	No rain	Rain	Rain
st12086	63190	51.233	3.867	3.302	24.2	3.2	Rain	Rain	Rain
st12112	63440	51.95	4.45	0	12.9	0.2	No rain	Rain	Rain
st12100	63500	51.567	4.933	0	23.5	2.1	No rain	Rain	Rain
st12107	63560	51.867	5.15	0	29.1	8.0	No rain	Rain	Rain
st12089	63700	51.45	5.417	0	5.4	23.6	No rain	Rain	Rain

Appendix 17: NW Europe Rain gauge Stations 12th July

GSOD station	USAF	Lat_new	Lon_new	observed	PP-VNIR	H-E	observed	PP-VNIR	H-E
st2580	64000	51.083	2.65	9.906	4.52	2.908	Rain	Rain	Rain
st2584	64070	51.2	2.867	0	12.14	9.044	No rain	Rain	Rain
st 2585	64280	50.933	3.667	19.05	24.156	18.728	Rain	Rain	Rain
st2582	64310	51.183	3.817	10.922	42.636	18.528	Rain	Rain	Rain
st2564	64320	50.567	3.833	18.034	19.292	19.652	Rain	Rain	Rain
st2571	64470	51.2	2.867	3.048	12.852	22.064	Rain	Rain	Rain
st2560	64490	50.467	4.45	0	14.492	22.728	No rain	Rain	Rain
st2583	64500	51.2	4.467	5.08	24.656	19.232	Rain	Rain	Rain
st2573	64510	50.9	4.533	0	12.24	20.2	No rain	Rain	Rain
st2557	64560	50.233	4.65	7.874	19.708	22.916	Rain	Rain	Rain
st2567	64780	50.65	5.45	0	11.54	16.348	No rain	Rain	Rain
st2581	64790	51.167	5.467	8.89	8.104	17.544	Rain	Rain	Rain
st2562	64900	50.483	5.917	0	13.072	15.332	No rain	Rain	Rain
st2559	64960	50.467	6.183	0.508	7.736	12.268	Rain	Rain	Rain
st12127	62400	52.3	4.767	0	4.576	19.756	No rain	Rain	Rain
st12120	62600	52.1	5.183	1.778	8.216	27.2	Rain	Rain	Rain
st12155	62700	53.217	5.767	0	22.256	35.684	No rain	Rain	Rain
st 12142	62730	52.7	5.883	0	22.336	25.852	No rain	Rain	Rain
st12119	62750	52.067	5.883	0	29.26	28.98	No rain	Rain	Rain
st12131	62780	52.433	6.267	6.35	40.104	28.316	Rain	Rain	Rain
st12144	62790	52.75	6.517	8.382	55.196	34.336	Rain	Rain	Rain
st12152	62800	53.133	6.583	17.78	59.852	45.28	Rain	Rain	Rain
st12118	62830	52.067	6.65	0	31.116	24.704	No rain	Rain	Rain
st2124	62900	52.267	6.9	0	19.388	17.532	No rain	Rain	Rain
st12086	63190	51.233	3.867	0	31.548	18.352	No rain	Rain	Rain
st12112	63440	51.95	4.45	0	9.184	19.204	No rain	Rain	Rain
st 12100	63500	51.567	4.933	0	14.776	20.864	No rain	Rain	Rain
st12107	63560	51.867	5.15	0	6.888	25.14	No rain	Rain	Rain
st12089	63700	51.45	5.417	0	6.652	22.896	No rain	Rain	Rain

Appendix 18: Kenya Rain gauge Stations 2nd April

GSOD Stations	USAF	Lat_new	Lon_new	observed	PP-VNIR	H-E	observed	PP-VNIR	H-E
st 10732	638200	-4.033	39.617	0.0	0.0	0.0	No rain	No rain	No rain
st 10733	637930	-3.4	38.567	0.0	0.0	0.0	No rain	No rain	No rain
st 10734	637990	-3.233	40.1	0.0	0.0	0.0	No rain	No rain	No rain
st 10735	637660	-2.283	37.833	0.0	11.5	0.0	No rain	Rain	No rain
st 10736	637720	-2.267	40.9	0.0	0.0	0.0	No rain	No rain	No rain
st 10737	697104	-2.267	40.9	0.0	0.3	3.0	No rain	Rain	Rain
st 10738	637380	-1.883	36.283	0.0	0.5	0.2	No rain	Rain	Rain
st 10739	637400	-1.317	36.917	0.0	40.4	1.1	No rain	Rain	Rain
st 10740	637420	-1.317	36.817	0.0	20.7	0.2	No rain	Rain	Rain
st 10742	637410	-1.3	36.75	0.0	18.6	0.1	No rain	Rain	Rain
st 10743	637390	-1.267	36.867	0.0	0.6	0.1	No rain	Rain	Rain
st 10744	637370	-1.133	35.833	0.0	0.1	0.0	No rain	Rain	No rain
st 10745	637085	-0.683	34.7	0.0	17.1	86.7	No rain	Rain	Rain
st 10746	637090	-0.667	34.783	0.0	17.1	86.7	No rain	Rain	Rain
st 10747	637200	-0.5	37.45	0.0	1.4	0.0	No rain	Rain	No rain
st 10748	637170	-0.5	36.967	0.0	5.8	0.0	No rain	Rain	No rain
st 10749	637230	-0.467	39.633	0.0	20.5	25.5	No rain	Rain	Rain
st 10750	637100	-0.367	35.35	6.9	24.9	114.4	Rain	Rain	Rain
st 10751	637140	-0.267	36.1	0.0	112.3	71.2	No rain	Rain	Rain
st 10752	637080	-0.1	34.75	0.0	82.8	59.5	No rain	Rain	Rain
st 10754	636950	0.083	37.65	0.0	11.3	0.0	No rain	Rain	No rain
st 10755	636870	0.283	34.783	0.0	3.4	109.7	No rain	Rain	Rain
st 10756	636953	0.25	37.583	0.0	0.0	0.0	No rain	No rain	No rain
st 10757	636880	0.4	35.233	0.0	0.0	7.6	No rain	No rain	Rain
st 10758	636860	0.533	35.283	0.0	0.0	17.4	No rain	No rain	Rain
st 10759	636610	1.016	35	0.0	0.9	58.6	No rain	Rain	Rain
st 10760	636710	1.75	40.067	0.0	28.7	3.1	No rain	Rain	Rain
st 10762	636410	2.3	37.9	0.0	3.4	0.0	No rain	Rain	No rain
st 10763	636120	3.117	35.617	0.0	0.1	0.0	No rain	Rain	No rain
st 10764	636190	3.533	39.033	0.0	0.0	0.0	No rain	No rain	No rain
st10731	63694	0.017	37.067	0.0	50.0	52.6	No rain	Rain	Rain

Appendix 19: Kenya Rain gauge Stations 3rd April

GSOD Stations	USAF	Lat_new	Lon_new	observed	PP-VNIR	H-E	observed	PP-VNIR	H-E
st 10732	638200	-4.033	39.617	0.0	0.0	0.5	No rain	No rain	No rain
st 10733	637930	-3.4	38.567	0.0	0.7	2.2	No rain	Rain	Rain
st 10734	637990	-3.233	40.1	0.0	0.0	0.0	No rain	No rain	No rain
st 10735	637660	-2.283	37.833	0.0	0.0	0.0	No rain	No rain	No rain
st 10736	637720	-2.267	40.9	0.0	0.0	0.0	No rain	No rain	No rain
st 10737	697104	-2.267	40.9	6.1	38.2	41.5	Rain	Rain	Rain
st 10738	637380	-1.883	36.283	0.0	0.0	0.0	No rain	No rain	No rain
st 10739	637400	-1.317	36.917	6.1	0.0	0.0	Rain	No rain	No rain
st 10740	637420	-1.317	36.817	0.0	0.1	0.0	No rain	Rain	No rain
st 10742	637410	-1.3	36.75	0.0	0.1	0.0	No rain	Rain	No rain
st 10743	637390	-1.267	36.867	0.0	0.4	0.0	No rain	Rain	No rain
st 10744	637370	-1.133	35.833	0.0	0.0	0.0	No rain	No rain	No rain
st 10745	637085	-0.683	34.7	54.5	60.0	27.7	Rain	Rain	Rain
st 10746	637090	-0.667	34.783	0.0	15.2	86.9	No rain	Rain	Rain
st 10747	637200	-0.5	37.45	0.0	1.7	0.0	No rain	Rain	No rain
st 10748	637170	-0.5	36.967	33.0	1.1	0.0	Rain	Rain	No rain
st 10749	637230	-0.467	39.633	39.1	4.2	0.1	Rain	Rain	Rain
st 10750	637100	-0.367	35.35	0.0	27.9	92.6	No rain	Rain	Rain
st 10751	637140	-0.267	36.1	20.1	15.5	29.3	Rain	Rain	Rain
st 10752	637080	-0.1	34.75	0.0	0.0	51.7	No rain	No rain	Rain
st 10754	636950	0.083	37.65	52.1	1.5	0.0	Rain	Rain	No rain
st 10755	636870	0.283	34.783	0.0	3.0	90.5	No rain	Rain	Rain
st 10756	636953	0.25	37.583	0.0	7.2	0.0	No rain	Rain	No rain
st 10757	636880	0.4	35.233	2.0	0.0	43.6	Rain	No rain	Rain
st 10758	636860	0.533	35.283	0.0	0.0	32.5	No rain	No rain	Rain
st 10759	636610	1.016	35	8.9	3.6	10.7	Rain	Rain	Rain
st 10760	636710	1.75	40.067	0.0	15.8	6.5	No rain	Rain	Rain
st 10762	636410	2.3	37.9	0.0	3.3	0.0	No rain	Rain	No rain
st 10763	636120	3.117	35.617	0.0	0.0	0.0	No rain	No rain	No rain
st 10764	636190	3.533	39.033	0.0	0.0	0.0	No rain	No rain	No rain
st10731	63694	0.017	37.067	0.0	56.0	0.1	No rain	Rain	Rain

Appendix 20: Polynomial curves